ISSN 1408-7073

RMZ – MATERIALS AND GEOENVIRONMENT

PERIODICAL FOR MINING, METALLURGY AND GEOLOGY

RMZ – MATERIALI IN GEOOKOLJE

REVIJA ZA RUDARSTVO, METALURGIJO IN GEOLOGIJO

RMZ-M&G, Vol. 55, No. 1 pp. 1-146 (2008)

Ljubljana, February 2008

Historical Review

More than 80 years have passed since in 1919 the University Ljubljana in Slovenia was founded. Technical fields were joint in the School of Engineering that included the Geologic and Mining Division while the Metallurgy Division was established in 1939 only. Today the Departments of Geology, Mining and Geotechnology, Materials and Metallurgy are part of the Faculty of Natural Sciences and Engineering, University of Ljubljana.

Before War II the members of the Mining Section together with the Association of Yugoslav Mining and Metallurgy Engineers began to publish the summaries of their research and studies in their technical periodical Rudarski zbornik (Mining Proceedings). Three volumes of Rudarski zbornik (1937, 1938 and 1939) were published. The War interrupted the publication and not until 1952 the first number of the new journal Rudarsko-metalurški zbornik - RMZ (Mining and Metallurgy Quarterly) has been published by the Division of Mining and Metallurgy, University of Ljubljana. Later the journal has been regularly published quarterly by the Departments of Geology, Mining and Geotechnology, Materials and Metallurgy, and the Institute for Mining, Geotechnology and Environment.

On the meeting of the Advisory and the Editorial Board on May 22nd 1998 Rudarsko-metalurški zbornik has been renamed into "RMZ - Materials and Geoenvironment (RMZ -Materiali in Geookolje)" or shortly RMZ - M&G.

RMZ - M&G is managed by an international advisory and editorial board and is exchanged with other world-known periodicals. All the papers are reviewed by the corresponding professionals and experts.

RMZ - M&G is the only scientific and professional periodical in Slovenia, which is published in the same form nearly 50 years. It incorporates the scientific and professional topics in geology, mining, and geotechnology, in materials and in metallurgy.

The wide range of topics inside the geosciences are welcome to be published in the RMZ -Materials and Geoenvironment. Research results in geology, hydrogeology, mining, geotechnology, materials, metallurgy, natural and antropogenic pollution of environment, biogeochemistry are proposed fields of work which the journal will handle. RMZ - M&G is co-issued and co-financed by the Faculty of Natural Sciences and Engineering Ljubljana, and the Institute for Mining, Geotechnology and Environment Ljubljana. In addition it is financially supported also by the Ministry of Higher Education, Science and Technology of Republic of Slovenia.

Editor in chief

Table of Contents – Kazalo

Internal oxidation of Cu-C and Ag-C composites

Notranja oksidacija Cu-C in Ag-C kompozitov

Gabrijela Čevnik[1,3], Gorazd Kosec[2,3], Ladislav Kosec[3], Rebeka Rudolf[4], Borut Kosec[3], Ivan Anžel[4]

[1]METAL Ravne d.o.o., Koroška cesta 14, SI-2390 Ravne na Koroškem, Slovenia;
E-mail: gcevnik@metalravne.com
[2]ACRONI d.o.o., Cesta Borisa Kidriča 44, SI-4270 Jesenice, Slovenia;
E-mail: gorazd.kosec@acroni.si
[3]University of Ljubljana, Faculty of Natural Sciences and Engineering, Aškerčeva cesta 12, SI-1000 Ljubljana, Slovenia; E-mail: kosec@ntf.uni-lj.si, borut.kosec@ntf.uni-lj.si
[4]University of Maribor, Faculty of Mechanical Engineering, Smetanova ulica 17, SI-2000 Maribor, Slovenia; E-mail: rebeka.rudolf@uni-mb.si, ivan.anzel@uni-mb.si

Received: December 3, 2007 **Accepted:** January 11, 2008

Abstract: The internal oxidation in copper-carbon and silver-carbon composites occurs when they are exposed to air or oxygen at high temperature. Solubility of carbon in copper or in silver is very low. The kinetics of oxidation at high temperature and activation energy were determined and the mechanism of internal oxidation was analysed. The kinetics of internal oxidation was determined for both cases and it is depended from the diffusion of oxygen following parabolic time dependence according to Wagner's theory. The activation energy for Cu-C composite is 70.5 kJ/mol, and for Ag-C composite is 50.1 kJ/mol, what is in both cases close to the activation energy for the volume diffusion of oxygen in copper or in silver. In both cases gas products are formed during the internal oxidation of composites. In the internal oxidation zone pores, bubbles occur. The carbon oxidates directly with the oxygen from solid solution as long there is a contact, which breaks down with the presence of gas products. Then the oxidation occurs over the gas mixture of CO and CO_2.

Izvleček: Pri visokih temperaturah kompoziti bakra in srebra z ogljikom na zraku ali v kisiku reagirajo po mehanizmu notranje oksidacije. Topnost ogljika v trdnem bakru in trdnem srebru je zelo majhna. Analizirali smo kinetiko oksidacije kompozitov, določili aktivacijsko energijo in mehanizem notranje oksidacije. Kinetika oksidacije je pri obeh skupinah materialov odvisna od difuzije kisika in sledi parabolični odvisnosti od časa v skladu z Wagnerjevo teorijo. Aktivacijska energija procesa je za kompozit Cu-C enaka 70,5 kJ/mol, za kompozit Ag-C pa 50,1 kJ/mol, kar je blizu aktivacijski energiji za volumsko difuzijo kisika v trdnem bakru oziroma srebru. Pri

Preliminary note

oksidaciji kompozita nastajajo plinski produkti. Oksidacija ogljika poteka neposredno s kisikom iz trdne raztopine, ko pa se zaradi nastanka plinske faze stik prekine, pa preko plinske zmesi CO in CO_2.

Key words: internal oxidation, internal oxidation zone (IOZ), composite, copper, silver, diffussion, kinetics
Ključne besede: notranja oksidacija, cona notranje oksidacije (CNO), kompozit, baker, srebro, difuzija, kinetika

Introduction

Internal oxidation is a general term for the process taking place under the surface of alloys and including the selective reaction of a less noble composite constituent with oxygen[1,2]. The phenomenon of internal oxidation was first noticed in copper alloys with silicon, nickel, tin, manganese and zinc, but it is also seen in silver alloys with additions of less noble alloy constituents[3]. The oxidation of these alloys results in the zone with a typical heterogeneous composition, the so called internal oxidation zone (IOZ)[4,5].

The internal oxidation is a phenomenon that includes several elementary processes with oxygen transmission as the most important factor of growth and morphological characteristics of the oxidized zone.

Conditions for the process of internal oxidation are[4,6]:

- larger electronegativity of alloy constituent from the basic metal,
- larger oxygen solubility in basic metal, and
- higher diffusion rate of oxygen in basic metal in comparison with the diffusion rate of alloy constituent.

Special examples require additional conditions like the maximal concentration of alloy constituent, oxidation temperature and partial oxygen pressure in atmosphere. All these influence the transmission process from the internal to external oxidation or passivation.

Theoretical principles

The first theoretic analysis being the principle of further research was made by Wagner[4] who used his own principle mathematic pattern for the caluclation of process kinetics to explore typical examples of internal oxidation in different alloys.

The discussed examples of oxidation of Cu-C and Ag-C composites belong to the examples of internal oxidation of two-phase alloys. Copper and silver dissolve a small portion of carbon in both liquid and solid state, and do not create compouds with carbon. Therefore their composites are two-phase composites and consist of a matrix and carbon particles.

Copper and silver meet the conditions that are necessary for internal oxidation:

- both metals are more noble than carbon,
- oxygen solubility in both metals is relatively high, and

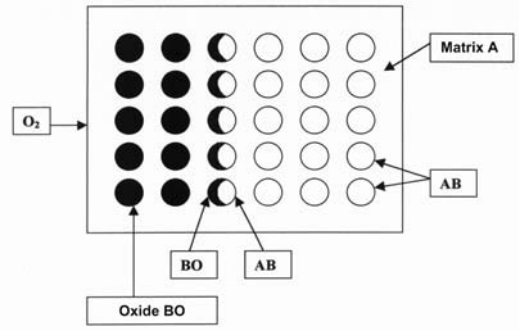

Figure 1. Internal oxidation mechanism of two-phase alloys when there is no dissolution of alloy component during oxidation
Slika 1. Mehanizem notranje oksidacije dvofazne zlitine za primer, ko se legirni element ne raztaplja med oksidacijo

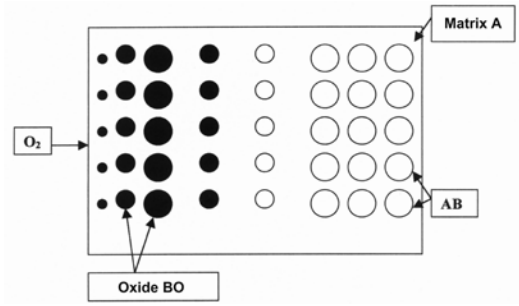

Figure 2. Mechanism of a two-phase alloy internal oxidation when there is a dissolution of the alloy component during oxidation
Slika 2. Mehanizem notranje oksidacije dvofazne zlitine za primer, ko se legirni element raztaplja med oksidacijo

- diffusion rate of oxygen exceeds the diffusion rate of carbon.

Internal oxidation of two-phase alloys and composites runs according to one of Kapteijn and Meijering mechanisms[6,7] or follows the mechanism that is a combination of both[8] (Figures 1 and 2).

Experimental work

For testing purpose, samples made of copper with 1 and 2 m.% carbon and samples made of silver with 1, 2, 5 and 10 m.% carbon were prepared[9-11]. Cu-C and Ag-C composites were made using the process of powder metallurgy. Mixtures of metal and graphite powder were compacted in a rigid hydraulic tool on the hydraulic press. They were subjected to sintering under vacuum and then to hot isostatic process. As a result, materials reached a practically theoretic density with no porosity. Cu-C composits were oxidized in a mixture of Cu_2O and Cu powders so that the oxygen partial pressure equalled Cu_2O dissociation pressure. Therefore, no copper oxide was created on the surface of Cu-C composites and internal oxidation was released. In case of Ag-C composites, internal oxidation was released also in the air or in pure oxygen as silver oxide disintegrates completely already at temperatures around 453 K [12].

We cut samples from both materials and prepared them for a metallographic analysis using an optical microscope (OM) and scanning electronic microscope (SEM).

Results and discussion

After the internal composite oxidation, the zone of internal oxidation (IOZ) consists of a matrix and scattered oxide particles (bubbles, pores) of composite constituent. A comparison of morphological characteristics of the internally oxidized zone in different composites shows essential differences in the size, form and distribution of oxide particles in the matrix. We noticed no resi-

dues of porosity at the microscopic level. We found that the thermodynamic condition for the internal oxidation is met in the Cu-C and Ag-C composites.

Metallographic characteristics of internally oxidized Cu-C composites show that internal oxidation is running primarily with a direct carbon oxidation (Figure 3). Metallographic characteristics of internally oxidized Ag-C composites show that oxidation of these type of composites is probably running directly out of a solid solution (Figures 4 and 5).

On the basis of kinetics of growth of the internal oxidation zone (Figures 6 and 7) we calculated the activation energy of process. The activation energy for Cu-C compositesis 70.5 kJ/mol which is close to the activation energy for a volume diffusion of oxygen in copper between 1023 and 1323 K that amounts to 67.2 kJ/mol.

For Ag-C composites, the calculated activation energy is 50.1 kJ/mol which is close to the activation energy for a volume diffusion of oxygen in silver between 1023 and 1173 K that amounts to 46.1 kJ/mol.

In both examples, the activation energies are very close to the activation energy for a volume diffusion of oxygen in copper and in silver. This makes us conclude that kinetics of the internal oxidation in both composite groups primarily depends upon oxygen diffusion.

Conclusions

Ag-C and Cu-C composites meet all necessary conditions for internal oxidation. They

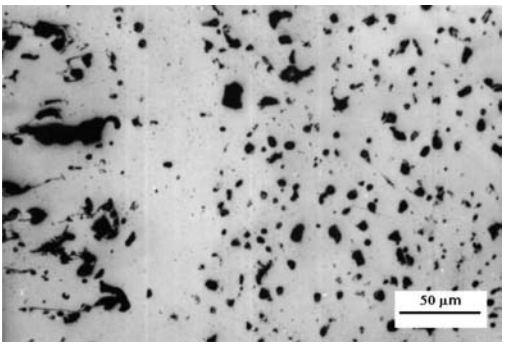

Figure 3. Microstructure of internally oxidized Cu-2m.% C composite (1323 K, 23h, oxygen)
Slika 3. Mikrostruktura notranje oksidiranega kompozita Cu-2m.% C (1323 K, 23h, kisik)

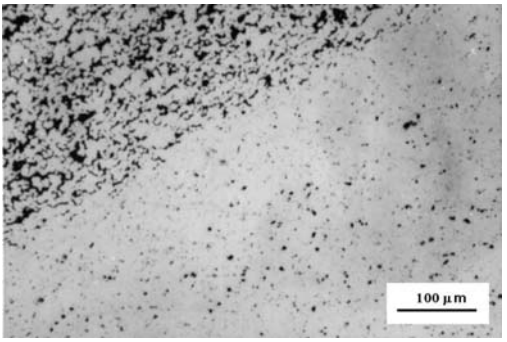

Figure 4. Microstructure of internally oxidized Ag-10m.% C composite (1123 K, 4h, oxygen)
Slika 4. Mikrostruktura notranje oksidiranega kompozita Ag-10m.% C (1123 K, 4h, kisik)

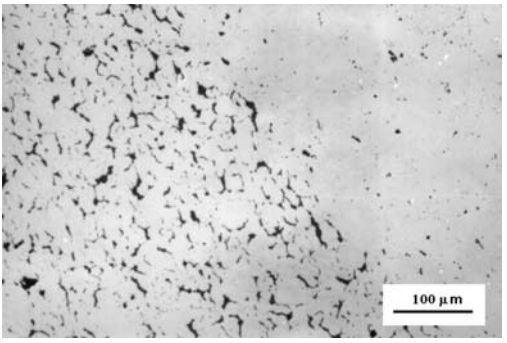

Figure 5. Microstructure of internally oxidized Ag-5m.% C composite (1123 K, 4h, oxygen)
Slika 5. Mikrostruktura notranje oksidiranega kompozita Ag-5m.% C (1123 K, 4h, kisik)

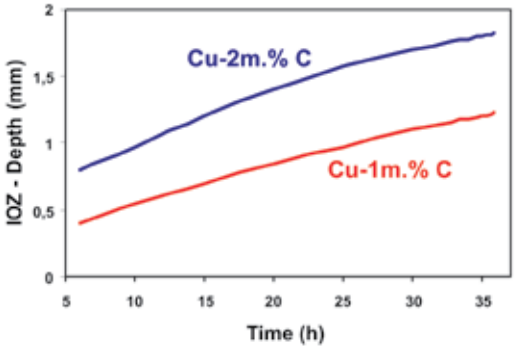

Figure 6. Kinetics of the internal oxidation of Cu-1m.% C and Cu-2m.% C composites at 1323 K in Cu-Cu_2O mixture
Slika 6. Kinetika notranje oksidacije kompozitov Cu-1m.% C in Cu-2m.% C pri 1323 K v Cu-Cu_2O zmesi

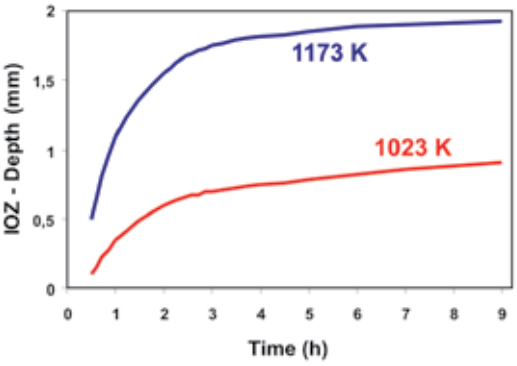

Figure 7. Kinetics of internal oxidation of Ag-5m.% C composite
Slika 7. Kinetika notranje oksidacije kompozita Ag-5m.% C

are typical two-phase composites and gas products are the result of internal oxidation. The internal oxidation of Cu-C composites is running primarily with a direct carbon oxidation. The kinetics of oxidation parabolically depends upon time and is controlled by oxygen diffusion in solid copper. Arising pores are unstable and get spheroidized.

In case of Ag-C composites, we noticed some similarity between the geometry of pores and carbon particles only with small concentrations of carbon (0.5 to 2 m.% C). Differences are obvious with large carbon concentrations. In the discussed example, oxygen diffusion in silver is the most essential parameter for the control of oxidation kinetics.

Carbon oxidation is carried out directly with oxygen out of solid solution and - when the creation of gas phase this contact is interrupted - over a gas mixture of CO and CO_2.

Povzetek

Notranja oksidacija Cu-C in Ag-C kompozitov

Kompoziti bakra in srebra z ogljikom v kisiku ali na zraku reagirajo pri visokih temperaturah po t.i. mehanizmu notranje oksidacije. Topnost ogljika v trdnem bakru in trdnem srebru je zelo majhna.

Analizirali smo kinetiko oksidacije kompozitov, določili aktivacijsko energijo in mehanizem notranje oksidacije. Kinetika oksidacije je tako pri kompozitih Cu-C kot tudi pri kompozitih Ag-C odvisna od difuzije kisika in sledi parabolični odvisnosti od časa v skladu z Wagnerjevo teorijo.

Aktivacijska energija procesa je za kompozite Cu-C enaka 70,5 kJ/mol, za kompozite Ag-C pa 50,1 kJ/mol, kar je zelo blizu aktivacijski energiji za volumsko difuzijo kisika v trdnem bakru oziroma srebru.

Pri oksidaciji kompozita nastajajo plinski produkti. Oksidacija ogljika poteka neposredno s kisikom iz trdne raztopine, ko pa se zaradi nastanka plinske faze stik prekine, pa preko plinske zmesi CO in CO_2.

V okviru predstavljenega dela so bili izdelani in analizirani kompoziti Cu-C z 1 oziroma 2 m.% C ter kompoziti Ag-C z 1, 2, 5 in 10 m.% C. Vsi kompoziti obravnavani v prispevku so bili izdelani po postopkih metalurgije prahov. Z uporabo optične in elektronske presevne mikroskopije so bile izvedene metalografske analize vzorcev obeh navedenih skupin kompozitnih materialov.

References

[1] Rapp, A. (1965): Kinetics, Microstructures and Mechanism of Internal Oxydation – Its Effect and Prevention in High Temperature Alloy Oxydation. *Corrosion*.; Vol. 21, pp. 382-401.

[2] Hagan, S.P., Polizzotti, A., Luckman, G. (1985): Internal Oxydation of Binary Alloys. *SIAM Journal of Applied Matherials*.; Vol. 45, No. 6, pp. 956-971.

[3] Gesmundo, F., Viani, F., Niu, Y. (1996): The Internal Oxidation of Two-Phase Binary Alloys Under Low Oxidant Pressures. *Oxidation of Metals*.; Vol. 45, No. 1-2, pp. 51-76.

[4] Wagner, C. (1959): Reaktionstypen bei der Oxydation von Legierungen. *Zeitschrift für Elektrochemie*.; Vol. 63, pp. 722-782.

[5] Kosec, L., Kosec, B., Horvat, S. (1999): Internal Oxidation of Binary Silver-Sulphur Alloys. *Metall*.; Vol. 53, No. 7-8, pp. 383-385.

[6] Kapteijn, J., Meijering, J.L. (1973): Internal Oxidation of Two-Phase Alloys. *Zeitschrift für Metallkunde*.; Vol. 64, No. 8 , pp. 578-580.

[7] Meijering, J.L. (1971): Internal Oxidation in Alloys. *Advances in Materials Research*.; Vol. 5, Ed. Herman H., Wiley-Interscience.

[8] Anžel, I., Kneissl, A.C., Kosec, L. (1999): Internal Oxidation of Rapidly Solidified Ternary Copper Alloys; Part I: A New Model of Dispersoids Formation. *Zeitschrift für Metallkunde*.; Vol. 90, No. 8, pp. 621-629.

[9] Anžel, I., Kneissl, A.C., Kosec, L. (1999): Internal Oxidation of Rapidly Solidified Ternary Copper Alloys; Part II: An Experimental Study. *Zeitschrift für Metallkunde*.; Vol. 90, No. 8, pp. 630-636.

[10] Bizjak, M., Kosec, L. (2000): Phase Transformations of Al-Fe and Al-Fe-Zr Rapidly Solidified Alloys. *Zeitschrift für Metallkunde*.; Vol. 91, No. 2, pp. 160-164.

[11] Rudolf, R., Kosec, L., Križman, A., Anžel, I. (2006): Microstructure Analysis of Internally Oxidized Cu-C Composite. *Metallurgy*.; Vol. 45, No. 2, pp. 79-84.

[12] Kosec, G., Kosec, L., Anžel, I., Gontarev, V., Kosec, B., Bizjak, M. (2005): Internal Oxidation of Silver Alloys with Tellurium, Selenium and Sulphur. *Metallurgy*.; Vol. 44, No. 1, pp. 37-39.

Composition and morphology of diborides in Al-Ti-B alloys after annealing at 1873 K

Sestava in morfologija diboridov v zlitinah Al-Ti-B po žarjenju na 1873 K

Franc Zupanič[1]

[1]University of Maribor, Faculty of Mechanical Engineering, Smetanova ulica 17, SI-2000 Maribor, Slovenia; E-mail: franc.zupanic@uni-mb.si

Received: January 13, 2008 **Accepted:** February 26, 2008

Abstract: In the investigation, Al-Ti-B alloys with different Ti/B ratios were annealed at 1873 K for 10 hours. Under this condition diboride particles were in contact with molten aluminium. During annealing considerable growth of remaining unmelted diboride particles took place. The composition of diboride particles shifted extremely close to the composition of pure TiB_2 regardless of the Ti/B ratios in the alloys, indicating that in equilibrium almost pure TiB_2 coexisted with a melt. Diboride particles were bound with well-defined crystal facets. Types and relative size of the facets depended on the Ti/B ratio. It is strongly indicated that an excess of Ti (B) in the melt over that needed to form TiB_2 stabilizes crystal planes having planar arrangement of Ti (B) atoms.

Izvleček: V tej raziskavi smo več zlitin Al-Ti-B, ki so imele različna razmerja Ti/B, žarili 10 ur pri 1873 K. V teh razmerah so bili delci diborida v kontaktu z aluminijevo talino. Med žarjenjem so diboridni delci močno zrasli. Njihova sestava se je v vseh raziskanih zlitinah močno približala sestavi čistega TiB_2, kar kaže, da je v termodinamskem ravnotežju s talino praktično čisti TiB_2. Diboridni delci so bili obdani s kristalnimi fasetami. Vrsta in relativna velikost faset je bila močno odvisna od razmerja Ti/B. Obstajajo trdni dokazi, da presežek Ti (B) nad vrednostjo, ki je potrebna za tvorbo TiB_2, stabilizira kristalne ravnine, ki imajo ravninsko razporeditev Ti (B) atomov.

Key words: Al-Ti-B alloys, diboride phase, high-temperature annealing, morphology, microstructure

Ključne besede: Al-Ti-B zlitine, diboridna faza, visokotemperaturno žarjenje, morfologija, mikrostruktura

Scientific paper

INTRODUCTION

It is believed that particles of the diboride phase $(Al,Ti)B_2$ present in Al-Ti-B alloys play the most important role in the grain-refining process in aluminium alloys[1,2]. Therefore, they were the subject of several investigations[1-5]. The results show that during manufacturing of Al-Ti-B alloys by an aluminothermic synthesis the diboride phase is formed with compositions ranging from that of the stoichiometric AlB_2 to that of the stoichiometric TiB_2[1-3]. All diborides, pure AlB_2 and TiB_2, as well as the mixed diboride $(Al_xTi_{1-x})B_2$ $(0 < x < 1)$ posses the same crystal structure (space group P6/mmm, Ref. 6) and very similar lattice parameters (see Figure 1). On this ground it was suggested that the mixed diboride phase $(Al_xTi_{1-x})B_2$ represents a thermodynamically stable phase in the aluminium-rich corner of the Al-Ti-B ternary system[7]. However, some experimental results do not support this assumption[2,8]. JOHNSSON and JANSSON[2] found out that the composition of the mixed diboride moved toward the compositions of pure TiB_2 and AlB_2 during holding in liquid aluminium. In addition, it was discovered that during synthesis of Al-Ti-B alloys by arc melting almost pure AlB_2 and TiB_2 formed. Furthermore, the formation of the mixed diboride $(Al_xTi_{1-x})B_2$ from pure diborides AlB_2 and TiB_2 did not take place even after exposure for 1000 h at 1073 K[8].

However, 1073 K is relatively low temperature since it amounts only 0.3 T_m of TiB_2, where T_m indicates melting temperature of pure TiB_2: 3498 K[9]. This could mean that even if the mixed boride would be a thermodynamically stable phase, the transfor-

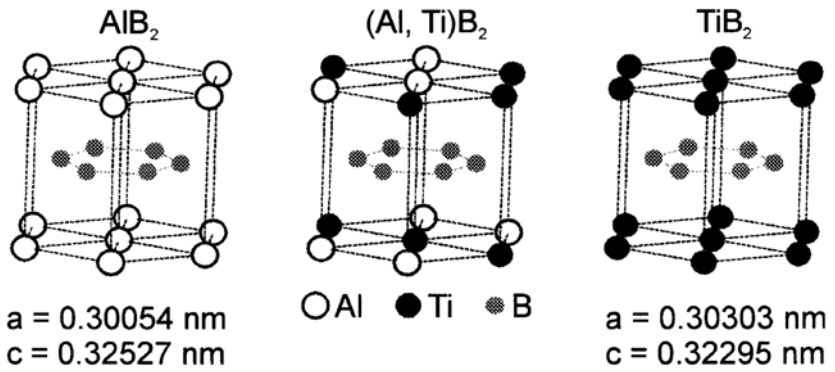

Figure 1. Crystal structures of diborides found in the ternary system Al-Ti-B. The diborides possess crystal structures belonging to the same space group P6/mmm. The lattice parameters are similar, mixed diboride having lattice parameters between those for AlB_2 and TiB_2. The crystal structure has layered form with alternate stack of planar hexagonal metal layers (m) and hexagonal boron layers (b).

Slika 1. Kristalne zgradbe diboridov v ternarnem sistemu Al-Ti-B. Kristalne zgradbe diboridov spadajo v isto prostorsko skupino P6/mmm. Mrežni parametri so podobni. Mrežni parametri zmesnega diborida so med parametri čistega AlB_2 in TiB_2. Zgradba diborida je plastna, sestavljena iz izmeničnih heksagonalnih kovinski plasti (m) in heksagonalnih borovih plasti (b).

mation of pure AlB_2 and TiB_2 to the mixed diboride $(Al_xTi_{1-x})B_2$ might be suppressed by kinetic reasons. Annealing of Al-Ti-B alloys containing both pure AlB_2 and TiB_2 is not possible at much higher temperatures that should allow completion of the transformation in shorter times, because AlB_2 would transform via a peritectic reaction to the liquid phase and α-AlB_{12} above 1253 K[10]. As a consequence, the diboride phase can be studied at higher temperatures only in equilibrium with other phases.

In this work some Al-Ti-B alloys with different Ti/B ratios were heated to 1873 K. This temperature exceeded 0.5 T_m of TiB_2, therefore in these conditions kinetic obstacles for achieving heterogeneous equilibrium between diboride phase and aluminium melt should be eliminated. The main purpose of the work was to determine the composition of the diboride phase coexisting with the liquid phase in order to contribute new information for the constitution of the ternary system Al-Ti-B. In addition, special attention was paid to the influence of Ti/B ratio on the morphology of diboride particles.

Experimental

Annealing of alloys

In this investigation samples of Al-Ti-B alloys were manufactured by an aluminothermic reduction of Ti and B from K_2TiF_6 and KBF_4 salts, respectively. The chemical compositions of the alloys are given in Table 1. Details of alloy preparation can be found elsewhere[12]. Before annealing at 1873 K the samples were put into small alumina crucibles situated inside a covered alumina vessel. The annealing took place in a high temperature furnace ASTRO in an argon atmosphere. Heating and cooling rates were 60 K/min, whereas the holding time at 1873 K was 10 hours.

Table 1. Composition of the investigated Al-Ti-B alloys prepared by an aluminothermic reduction of Ti from K_2TiF_6 and B from KBF_4
Tabela 1. Sestava preiskanih zlitin Al-Ti-B, ki so bile izdelane z aluminotermično redukcijo Ti iz K_2TiF_6 in B iz KBF_4

Alloy Zlitina	Ti / wt.% Ti / mas.%	B / wt.% B / mas. %	Ti/B weight ratio masno razmerje Ti/B	Ti + B / wt.% Ti + B / mas. %
A8	8.55	1.93	4.43	10.48
A6	7.34	2.86	2.56	10.2
A7-1	3.73	2.77	1.34	6.5
A7-2	3.14	2.85	1.1	5.99

Metallographic preparation

Samples for the light (LM) and scanning electron microscopy (SEM) were prepared using standard metallographic techniques[13]. The samples were polished directly before analyses with energy dispersive spectroscopy (EDS) to remove possible etching products and oxide layers on the investigated surface.

For investigation of the morphology of diboride particles deep etching was applied using two different etchants: (1) a solution consisting of 50 % HCl and water, and (2) a methanol-iodine solution (30 ml methanol, 3 g tartaric acid and 1 g iodine). Satisfying results were obtained after 10–15 min etching in the HCl solution and 1–2 hours etching in the methanol-iodine solution. It is important to stress that the mor-

phology of diboride particles in each alloy was the same regardless of the applied etchant. This strongly indicates that both etchants dissolved only aluminium matrix and, what is of utmost importance, did not attack diboride particles.

Energy dispersive spectroscopy

EDS was performed in a scanning electron microscope SIRION 400 NC (FEI Company), equipped with an energy dispersive analyser INCA 350 (Oxford Analytical). Boron was mainly determined qualitatively, whereas titanium and aluminium were determined quantitatively in all observed phases. We used titanium and aluminium standard spectra obtained from pure titanium and aluminium, as well as from pure diborides AlB_2 (large AlB_2 particles in binary Al-B alloy) and TiB_2 (from pure arc-melted TiB_2).

X-ray diffraction

The phase composition of alloys was determined using an X-ray diffractometer Philipps PW 1710. The general diffraction curves were recorded at a scanning rate of 0.025 °/s (Bragg angle) scan range from 5° to 70° and the detailed diffraction curves with 0.025 °/10 s with a scan range between 33.5° and 35° (around the (100) diboride peak).

The results of X-ray diffraction were primarily used for the determination of the diboride lattice parameters. It was found out that lattice parameters *a* and *c* of the diboride phase can be calculated reliably if positions of at least five diffraction peaks can be determined. In some cases only (100) peak was well defined. In this case only the value of *a*-axis could be calculated.

The composition of the diboride phase – the atomic fraction of aluminium on the metallic sublattice of diboride phase C_{Al} – was estimated on the basis of two criteria:

- the deviation of the lattice parameter *a* from that of pure TiB_2[3]:

$$C_{Al} = \frac{a_{TiB_2} - a}{a_{TiB_2} - a_{AlB_2}} 100 \ \% \qquad (1)$$

- the deviation of the axis ratio *c*/*a* from that of pure TiB_2[4]:

$$C_{Al} = \frac{c/a - (c/a)_{TiB_2}}{(c/a)_{AlB_2} - (c/a)_{TiB_2}} 100 \ \% \qquad (2)$$

RESULTS AND DISCUSSION

The compositions of Al-Ti-B alloys were chosen so that the diboride phase should exists in the equilibrium with the liquid phase at the annealing temperature (1873 K). During heating of Al-Ti-B alloys all other phases present initially (e.g. Al_3Ti, α-AlB_{12}, AlB_2) were melted completely, only the titanium-rich diboride remained partly unmelted. To estimate the quantity of unmelted TiB_2 the solubility product proposed by SIGWORTH[14] was used:

$$\log\ (w_{Ti})(w_B)^2 = 8.526 - 16,043/T \qquad (3)$$

where T means temperature in K, and w_{Ti} and w_B contents of Ti and B (in wt.%) in the melt, respectively. Table 2 shows the results. It is obvious that 4–7.2 % TiB_2 remained unmelted. Since the solubility product defined by equation (3) may be too

Table 2. Concentration of titanium and boron in the liquid phase and the quantity of unmelted TiB_2 at 1873 K using equation (3)
Tabela 2. Koncentracija titana in bora v talini in količina nestaljenega TiB_2 pri 1873 K, izračunana z uporabo enačbe (3)

Alloy	Ti dissolved in the melt / wt.%	B dissolved in the melt / wt.%	estimated initial quantity of TiB_2 / wt.%	unmelted TiB_2 at 1873 K / wt.%
A8	5.22	0.42	6.2	4.8
A6	2.40	0.62	9.2	7.2
A7-1	0.53	1.32	5.4	4.7
A7-2	0.36	1.59	4.6	4

high, the amount of unmelted TiB_2 is to be slightly higher.

Morphology of diboride particles

The size of the diboride particles in the initial state (after aluminothermic reduction) rarely exceeded 1 μm (Figure 2). In alloys with hypostoichiometric and stoichiometric composition (Ti/B ≤ 2.21) agglomerates of diboride particles in Al-rich solid solution could be observed. In alloys with hiperstoichiometric composition, in addition to boride agglomerates also Al_3Ti particles were present.

However, during annealing at 1873 K very large hexagonal plates of the titanium-rich diboride formed. The height of the plates often exceeded 5 μm and their edge 10 μm (Figures 3 and 4).

All diboride particles were bound with very well defined crystal faces; however their morphology was not the same in all investigated alloys. In the alloy A7-1 having an excess of B over that needed for formation of TiB_2 (Ti/B) = 1.34, the basal {0001} facets dominate (Figure 4a). Note also traces of the prismatic $\{10\bar{1}0\}$ and pyramidal facets. It is not possible to determine the Miller-Bravais indices of these pyramidal planes by inspection of deep-etched specimens only. However, it seems possible that their indices could be $\{h\bar{k}\,01\}$, $h > l$, $h = -k$.

In the near-stoichiometric alloy A6 (Ti/B = 2.56) two additional types of facets were observed (Figure 4b): prismatic $\{11\bar{2}0\}$ and pyramidal $\{11\bar{2}1\}$ facets. In the alloy A8 having an excess of Ti over that to form TiB_2 (Ti/B = 4.43), the diboride particles were bound by basal {0001} and prismatic $\{10\bar{1}0\}$ facets (Figure 4c).

To explain the influence of Ti/B ratio on the observed morphology of the diboride particles we must take a closer look to the atomic arrangements in the following crystallographic planes: {0001}, $\{10\bar{1}0\}$, $\{11\bar{2}0\}$, $\{11\bar{2}1\}$ and $\{2\bar{2}01\}$. In the {0001} planes, boron and titanium atoms form alternate planar layers (Figure 1). Thus, the outer layer in the contact with the liquid phase could be occupied only by boron or only by titanium atoms. In the family of $\{10\bar{1}0\}$ planes only titanium atoms can be arranged in a planar array, whereas the arrangement of boron atoms cannot be planar (Figure 5a). In both $\{11\bar{2}0\}$ and $\{11\bar{2}1\}$ families of planes it is not possible to get the planar outer layer occupied by only one kind of atoms, but in each case with both boron and titanium atoms (Figure 5a). On the other hand, boron atoms can be arranged in a planar manner, therefore the facets of this plane dominate in alloy A7-1.

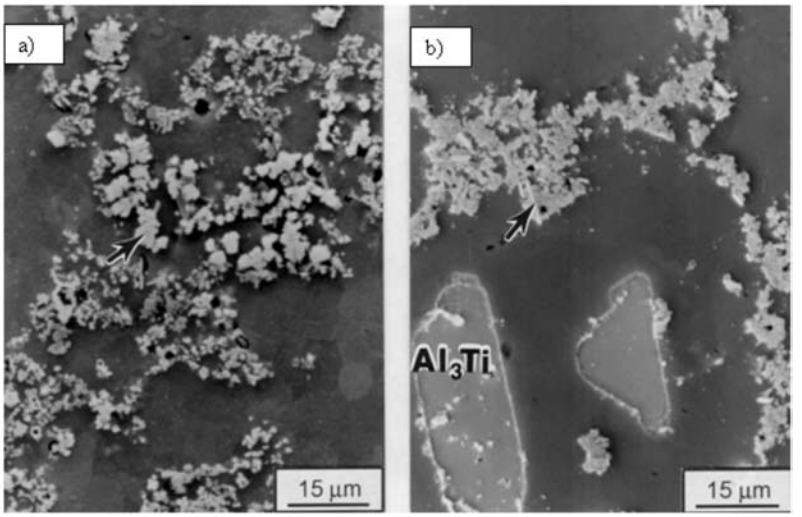

Figure 2. Secondary electron micrographs of a) alloy A7-1 and b) alloy A8. The arrows indicate diboride agglomerates.
Slika 2. Mikroposnetek z vrstičnim elektronskim mikroskopom (sekundarni elektroni) zlitin: a) A7-1 in b) A8. Puščici kažeta na diboridne agregate.

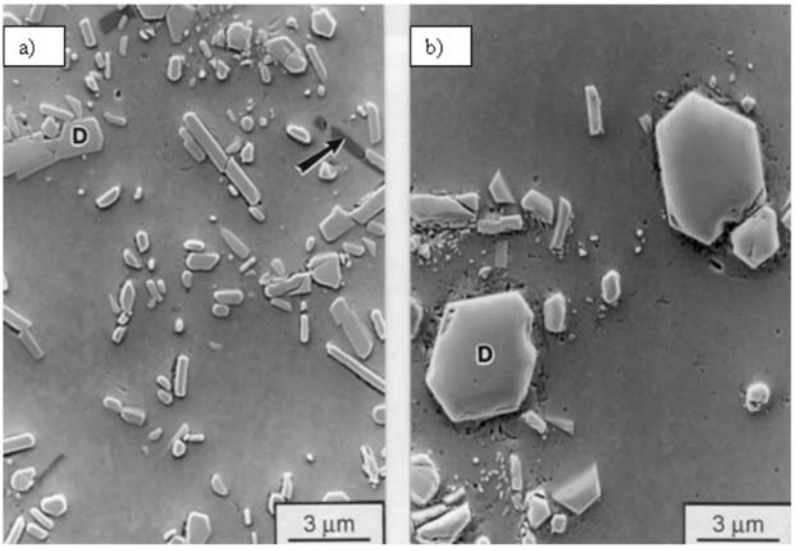

Figure 3. Secondary electron micrographs of a) alloy A7-1 and b) alloy A8. The arrow indicates AlB_2 particle. D indicates TiB_2.
Slika 3. Mikroposnetek z vrstičnim elektronskim mikroskopom (sekundarni elektroni) zlitin a) A7-1 in b) A8. Puščica kaže na delec AlB_2. D pomeni TiB_2.

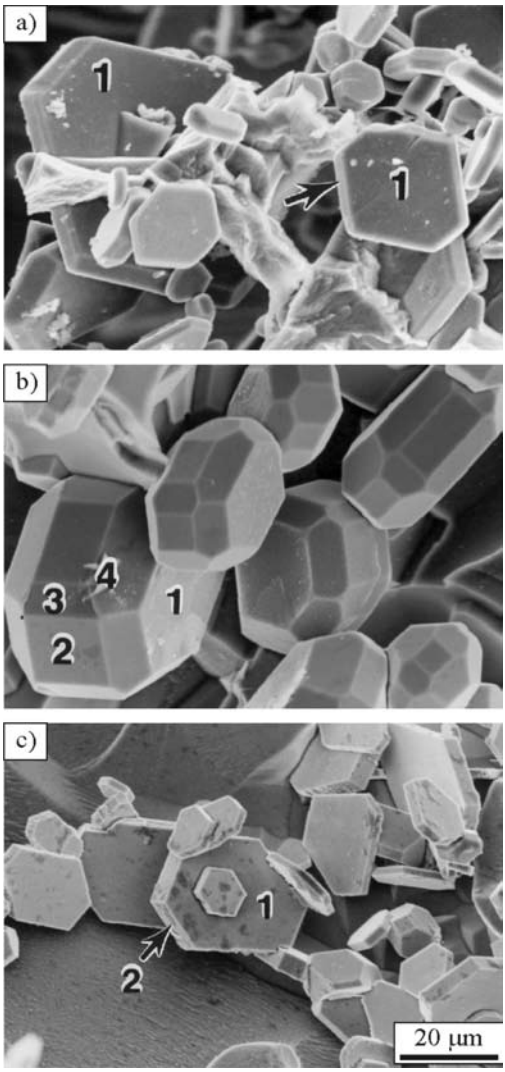

Figure 4. Secondary electron micrographs of diboride particles in the investigated alloys after deep-etching: a) Alloy A7-1, b) alloy A6 and c) alloy A8 after exposure for 10 hours and 1873 K (1: (0001), 2: $(10\bar{1}0)$, 3: $(11\bar{2}0)$, 4: $(11\bar{2}1)$, arrow in a: $(h\bar{k}\,01)$, $h > l$, $h = -k$)

Slika 4. Mikroposnetek z vrstičnim elektronskim mikroskopom (sekundarni elektroni) zlitin diboridnih delcev v preiskovanih zlitinah po globokem jedkanju: a) Zlitina A7-1, b) zlitina A6 and c) zlitina A8 po desetih 10 urah pri 1873 K (1: (0001), 2: $(10\bar{1}0)$, 3: $(11\bar{2}0)$, 4: $(11\bar{2}1)$, puščica na sliki a: $(h\bar{k}\,01)$, $h > l$, $h = -k$)

According to this analysis it is very likely that diboride particles in the alloys with an excess of titanium are bound with {0001} and $\{10\bar{1}0\}$ planes, because in these planes titanium alloys are arranged in planar array. Similarly, in the alloys with an excess of boron {0001} planes dominate, since in these planes boron atoms form planar layers. On the other hand, $\{11\bar{2}0\}$ and $\{11\bar{2}1\}$ planes that contain both titanium and boron atoms are very important in the alloy A6 having near-stoichiometric composition. The above presented evidence indicates that an excess of Ti (B) tends to stabilize crystal planes with the planar arrangements of Ti (B) atoms.

Composition of the diboride phase

The results of EDS analyses showed that even after 1000 s live time aluminium peaks could not be resolved in EDS spectra of diboride particles present in the alloy A8. On the X-ray diffraction curve only two peaks arising from the diboride phase were identified thus it was not possible to reliably calculate its lattice parameters. Only the length of the *a*-axis from the position of (100) diboride phase was calculated. Using equation (1) we determined C_{Al} = 1.67 at.% Al on the metallic sublattice. It is believed that in this case the results of EDS analysis were more reliable. Thus, apparently pure TiB_2 existed in the equilibrium with the liquid phase (Table 3).

EDS showed also that in the alloy A6 no aluminium peak could be resolved in spectra of diboride particles – similarly as in the alloy A8. On the other hand, several well-defined peaks arising from both Cu $K\alpha_1$ and Cu $K\alpha_2$ radiation could be easily resolved (Figure 6). The calculated lattice

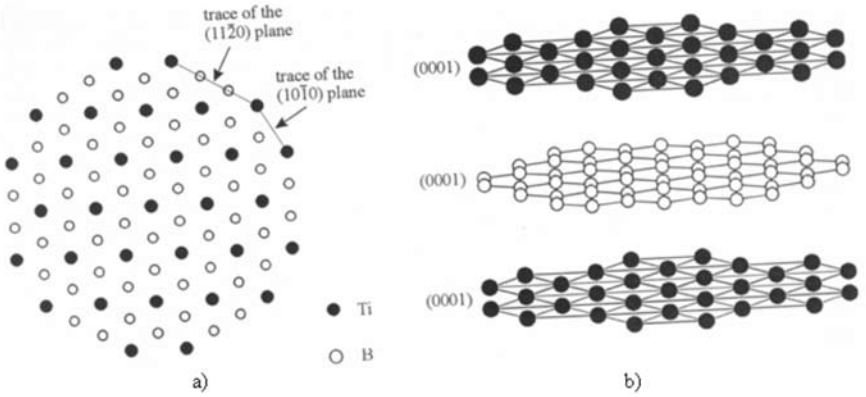

Figure 5. Arrangement of atoms in some planes of TiB_2. In a) TiB_2 crystal is bound by traces of {10$\bar{1}$0} and {11$\bar{2}$0} planes (projection perpendicular to (0001) plane. In b) planar arrangement of titanium and boron atoms in (0001) plane is shown.
Slika 5. Razporeditev atomov v nekaterih ravninah TiB_2. Na sliki a) je TiB_2 kristal obdan z ravninama {10$\bar{1}$0} in {11$\bar{2}$1} (projekcija pravokotna na ravnino (0001). Na sliki b) je prikazana ravninska ureditev titanovih in borovih atomov v ravnini (0001).

parameters coincided completely with the lattice parameters of pure TiB_2. The aluminium content computed by equations (1) and (2) amounts 0 at.% Al. Therefore, the results of EDS analysis, as well as the results of XRD clearly indicate that in this alloy almost pure TiB_2 exists in the equilibrium with the melt (Table 3).

Both alloys A7-1 and A7-2 existed at 1873 K in the two-phase liquid + diboride region. On EDS spectra of some diboride particles very small aluminium peaks could be observed. The calculations gave us the result $C_{Al} \approx 0{,}3$ at.% Al. This is close to the detection limit of the EDS. On X-ray diffraction curves peaks arising from the diffraction of Cu $K\alpha_1$- and Cu $K\alpha_2$-radiation on the lattice planes of both AlB_2 and TiB_2 could be observed. Of course, AlB_2 was not present at 1873 K, but has crystallized from the melt during cooling below 1173 K. The lattice parameters of the titanium-rich and aluminium-rich diborides corresponded closely to the lattice parameters of pure TiB_2 and AlB_2. Also in these alloys the experimental results showed that almost pure TiB_2 existed in the equilibrium with the melt at 1873 K (Table 3).

During annealing at 1873 K the size of diboride particles increased considerably. In can be shown by a simple calculation that one such particle have formed from several thousands to several ten thousands of particles that were initially present in the microstructure. It is the most probable that diboride particles shown in Figures 3 and 4 had formed by a process similar to the Ostwald ripening; smaller particles have dissolved and the larger particles have grown. Therefore, for the attainment of the

equilibrium composition of the diboride phase diffusivity inside particles is less important than the attachment/detachment kinetics during dissolution/growth of the diboride particles. Since under isothermal conditions diboride particles grow slowly, it is believed that he interface attachment/detachment kinetics should be fast enough to maintain the equilibrium composition of the diboride phase. On the basis of this discussion and the results of X-ray diffraction and EDS analyses we may conclude that at 1873 K apparently pure TiB_2 existed in the equilibrium with the liquid phase regardless of the Ti/B ratio.

Conclusions

During annealing at 1873 K considerable growth of unmelted diboride particles took place. They probably grew by a process similar to Ostwald ripening.

The composition of diborides was extremely close to the composition of pure

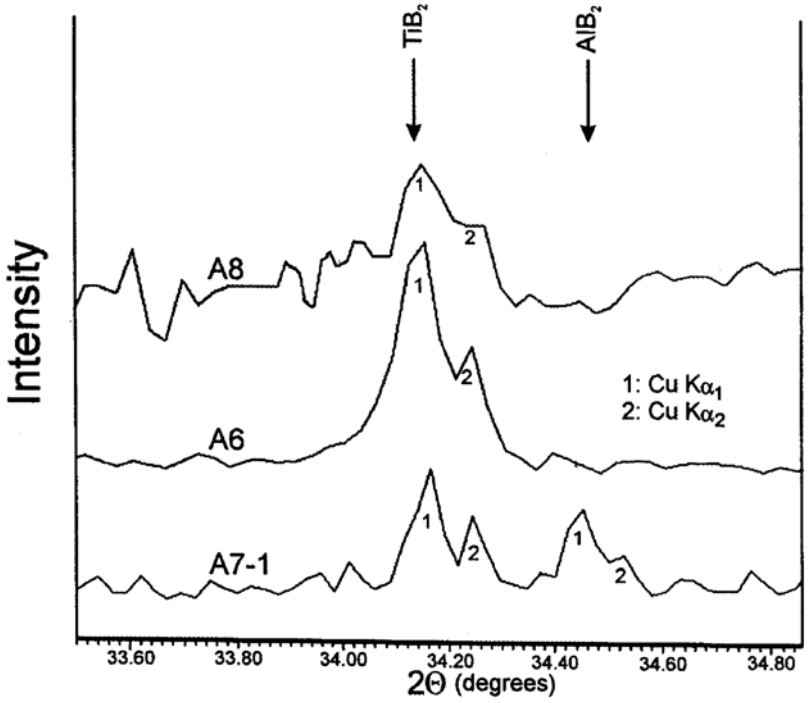

Figure 6. The results of X-ray diffraction. The shape and the position of the (100) diboride peak in different alloys after 10 hours exposure at 1873 K. In alloy A7-1 also peaks arising from AlB_2 that had formed during cooling could be seen. Arrows indicate the positions of (100) peaks of pure TiB_2 and pure AlB_2 by diffraction of Cu $K\alpha_1$ radiation.

Slika 6. Rezultati rentgenske difrakcije. Oblika in položaj vrhov (100) diborida v različnih zlitinah po 10 urah žarjenja pri 1873 K. V zlitini A7-1 se pojavi tudi vrh AlB_2, ker AlB_2 nastane pri ohlajanju. Puščici kažeta vrhova (100) čistega TiB_2 in čistega AlB_2 pri difrakciji Cu $K\alpha_1$.

Table 3. Aluminium content on the metallic sublattice of the diboride phase according to the results of XRD and EDS
Tabela 3. Vsebnost aluminija na kovinski podmreži diboridne faze skladno z rezultati XRD in EDS

alloy	C_{Al} / at.% Al (equation 1)	C_{Al} / at.% Al (equation 2)	C_{Al} / at.% Al (EDS)	remark pripomba
A8	1.5	-	0	TiB_2
A6	0	0	0	TiB_2
A7-1	0	0	0.3	TiB_2
A7-1	100	98.8	99.8	AlB_2

TiB_2 regardless of the Ti/B ratios in the investigated alloys. Therefore all evidence strongly suggests that at 1873 K almost pure TiB_2 existed in the equilibrium with the liquid phase in all investigated alloys.

Diboride particles were bound with well-defined crystal facets. Types and relative size of the facets were dependent on the Ti/B ratio. An excess of Ti (B) tended to stabilize crystal planes with the planar arrangement of Ti (B) atoms. In the alloy A8 with an excess Ti over that needed to form TiB_2 {0001} and {1010} planes dominated, whereas in alloy A7-1 and A7-2 having an excess of boron {0001} planes dominate, since in these planes boron atoms form planar layers. On the other hand, $\{11\bar{2}0\}$ and $\{11\bar{2}1\}$ planes that contain both titanium and boron atoms are very important in the alloy A6 having near-stoichiometric composition.

POVZETEK

Sestava in morfologija diboridov v zlitinah Al-Ti-B po žarjenju na 1873 K

Delci diboridne faze $(Al,Ti)B_2$ imajo pomembno vlogo pri udrobnitvi kristalnih zrn v aluminijevih zlitinah. Kadar zlitine Al-Ti-B izdelamo z aluminotermično sintezo imajo diboridi spekter sestav, ki se razteza od sestave čistega AlB_2 do sestave čistega TiB_2. V literaturi še vedno obstajajo razhajanja ali sta v sistemu Al-Ti-B termodinamsko stabilna čista diborida AlB_2 in TiB_2 ali pa zmesni diborid $(Al,Ti)B_2$.

V tej raziskavi smo raziskovali vzorce zlitine Al-Ti-B, ki smo jih izdelali z aluminotermično redukcijo Ti in B iz soli K_2TiF_6 in KBF_4. Zlitine Al-Ti-B so imele različno razmerje Ti/B. Zlitine smo nato žarili 10 ur pri 1873 K. Ta temperatura presega 0,5 T_t TiB_2 (T_t je temperatura tališča v kelvinih), zato so difuzijski procesi dovolj hitri, da se lahko vzpostavi ravnotežje v sorazmerno kratkem času.

Pri 1873 K so bili delci diborida v kontaktu z aluminijevo talino. Med žarjenjem so diboridni delci močno zrasli. Z analizo EDS in rentgensko difrakcijo (XRD) smo ugotovili, da se je njihova sestava v vseh raziskanih zlitinah močno približala sestavi čistega TiB_2. To kaže, da je v termodinamskem ravnotežju s talino praktično čisti TiB_2.

Ugotovili smo tudi, da so bili diboridni delci obdani s kristalnimi fasetami. Vrsta in relativna velikost faset je bila močno odvisna od razmerja Ti/B. V zlitini A8, v kateri je bil presežek titana glede na idealno stehiometrično razmerje (2,21:1) so bili diboridni delci obdani s fasetami osnovne ploskve {0001} in prizmatičnimi ravninami $\{10\bar{1}0\}$. V zlitini s skoraj stehiometrično sestavo (Ti/B = 2,56) sta se pojavile še fasete dveh dodatnih ravnin: prizmatične $\{11\bar{2}0\}$ in piramidne $\{11\bar{2}1\}$. V zlitini A7-1, ki je imela presežek B (Ti/B = 1,34) je prevladovala faseta osnovne ravnine {0001}.

Z analizo rezultatov in primerjavo faset z razporeditvijo atomov v diboridu smo ugotovili, da presežek Ti nad vrednostjo, ki je potrebna za tvorbo TiB_2, stabilizira kristalne ravnine, ki imajo ravninsko razporeditev Ti atomov. Podoben učinek ima B, ki stabilizira ravnine, v katerih so atomi B razporejeni v ravnini.

References

[1] Wang, C., Wang, M., Yu, B., Chen, D., Qin, P., Feng, M. and Dai, Q. (2007): The grain refinement behavior of TiB_2 particles prepared with in situ technology. *Materials Science and Engineering A*.; Vol. 459, Issues 1-2, pp. 238-243.

[2] Johnsson, M., Jansson, K. (1989): Study of $Al_{1-x}Ti_xB_2$ particles extracted from Al-Ti-B alloys. *Z. Metallkd*.; Vol. 89, pp. 394-398.

[3] Kiussalaas, R. (1986): Relation between phases present in master alloys of the Al-Ti-B type. *Chemical Communications*. Stockholm University.

[4] Stolz, U.K., Sommer, F., Predel, B. (1995): Phase equilibria of aluminium-rich Al-Ti-B alloys – solubility of TiB_2 in aluminium melts. *Aluminium*.; Vol. 71, pp. 350-355.

[5] Feng, C. F., Froyen, L. (1997): Incorporation of Al into TiB_2 in Al matrix composites and Al-Ti-B master alloys. *Materials Letters*.; Vol. 32, pp. 275-279.

[6] Pohl, A., Kizler, P., Telle, R., Aldinger, F. (1994): EXAFS studies of $(Ti,W)B_2$ compounds. *Z. Metallkde*.; Vol. 85, pp. 658-663.

[7] Hayes, F. H., Lukas, H. L., Effenberg, G., Petzow, G. (1989): Themodynamic calculation of the Al-rich corner of the Al-Ti-B system. *Z. Metallkde*.; Vol. 80, pp. 361-365.

[8] ZUPANIČ, F., SPAIĆ, S., KRIŽMAN, A. (1998): Contribution to the ternary system Al-Ti-B. Part 1: The study of diborides present in the aluminium corner. *Materials Science and Technology*.; Vol. 14, pp. 601-607.

[9] MASSALSKI, T. B. (1990): Binary alloys phase diagrams. *ASM International*.; pp. 544-548.

[10] MASSALSKI, T. B. (1990): Binary alloys phase diagram. *ASM International*.; pp. 123-125.

[11] ZUPANIČ, F., SPAIĆ, S., KRIŽMAN, A. (1998): Contribution to the ternary system Al-Ti-B. Part 1: The study of alloys in the triangle Al-AlB_2-TiB_2. *Materials Science and Technology*.; Vol. 14, pp. 1203-1212.

[12] ZUPANIČ, F., SPAIĆ, S. (1999): *Metall* (Berl. West). Vol. 53, No. 3, pp. 125-130.

[13] PETZOW, G. (1994): *Atzen*. 6. Auflage. Gebrüder Borntraeger, Berlin Stuttgart.

[14] SIGWORTH, G. K. (1984): The grain-refining of aluminium and phase relationships in the Al-Ti-B system. *Metall. Trans. A*.; Vol. 15A, pp. 272-282.

Tool for programmed open-die forging – case study

Orodje za programsko vodeno prosto kovanje – študija primera

David Bombač[1], Matevž Fazarinc[1], Goran Kugler[1], Radomir Turk[1]

[1]University of Ljubljana, Faculty of Natural Sciences and Engineering,
Department of Materials and Metallurgy, Aškerčeva cesta 12, SI-1000 Ljubljana, Slovenia;
E-mail: david.bombac@ntf.uni-lj.si, matevz.fazarinc@arnes.guest.si,
goran.kugler@ntf.uni-lj.si, rado.turk@ntf.uni-lj.si

Received: November 26, 2007 **Accepted:** January 13, 2008

Abstract: An open-die forging process as referred to in the following assumptions is a process where plastic material is compressed in one main axis only and the spread into the two other main axes is not limited. In view of present competitive markets modern open-die forging plants are highly dynamic production plants and vastly explore possibilities of programmed forging. Computer aided technology tools for programmed forging is the basis for innovative and cost effective technology planning which consider the performance limits of forging equipment and material in order to achieve the optimum productivity.

Izvleček: Proces prostega kovanja, ki je obravnavan v tej študiji, je postopek, kjer je material tlačno deformiran v eni smeri, v ostalih dveh pa se prosto širi. Na današnjem izredno konkurenčnem trgu so obrati prostih kovačnic izredno dinamični obrati in široko izkoriščajo možnost programiranega kovanja. Računalniško podprta tehnološka orodja za programirano kovanje so osnova za inovativno in cenovno učinkovito planiranje proizvodnje. Ta preuči meje zmožnosti stiskalnice in mejne vrednosti materiala, ter na podlagi teh določi optimalne pogoje preoblikovanja.

Key words: hot forming, open-die forging, programmed forging, pass schedule, forging simulation

Ključne besede: vroče preoblikovanje, prosto kovanje, programirano kovanje, plan vtikov, simulacija kovanja

Scientific paper

INTRODUCTION

In metal forming, open-die forging is a metal forming process in which a workpiece is usually pressed between flat dies with a series of compressive deformation steps and manipulated and/or rotated. The open-die forging process as referred to in the following assumptions is a process where plastic material is compressed in one main axis only and the spread into the two other main axes is not limited. It has not lost its importance in recent times and is for steel manufacturing carried out under hot working conditions when the metal is deformed plastically above its recrystallization temperature. The open-die forging plants consist of a forging press and one or two rail-bound manipulators. The dies or tools are small compared with the overall sizes of the forgings. The process is carried out incrementally, where only a part of the workpiece is being deformed at each stage. The principle of such an incremental forging process is simply the compressing or upsetting of the material step-by-step until it reaches the final target shape. In the further development of this type of forming operation, the requirements are for accuracy of load prediction and metal flow[1-3].

In view of present competitive markets modern open-die forging plants are highly dynamic production plants and vastly explore possibilities of programmed forging. Apart from the pure production speed, the main focus today is on the achievement of minimum forging tolerances and a consistent level of quality. In the past procedures in open-die forging were based on the individual forgemaster's experience and observation of each forging stroke to determine both elongation and sideways spreading. An experienced forge master can develop a geometrical pass schedule quite easily, however; the optimization of a pass schedule to minimize forging time is quite difficult as it involves the consideration of numerous factors which influence the production rate. Computer aided technology tools for programmed forging is the basis for innovative and cost effective technology planning which consider the performance limits of forging equipment and material in order to achieve the optimum productivity. It must consider all of the important factors including spread behaviour, die geometry and the speeds of the press and manipulators. The required pressing force relative to the material resistance is calculated as a function of the instantaneous temperature and compared to the maximum available press force.

Optimization of the pass schedules in the open-die forging technology and activities for successful implementation of the computer aided forging technology demand close cooperation between forging plants and science. Technology developed in cooperation must be constantly maintained and adapted to the latest technological breakthroughs.

THEORETICAL FRAMEWORK FOR PROGRAMMED FORGING

The open-die forging as mentioned before is incremental process where after one forging pass on a square bar the side faces take on an irregular shape, commonly termed barrelling, which is due to frictional constraint at the tool faces and to

the influence of the adjacent undeformed portion of the bar. The influence of the machine operator experience on the monitoring of the process must be decreased in order to ensure reproducible process that increases productivity and improve quality of the forgings hence reducing machine operator experience related fluctuations. Moreover computer aided forging technology enables judgment of the characteristic forging capabilities of the plant and their influence on the productivity[4]. However the machine operator has ability to initiate corrections to the programmed forging schedule any time if it is necessary.

Pass schedule calculation is determination of relevant process data for processing a defined end piece from initial ingot. Such calculation is very demanding due to complexity of open-die forging process. For instance to enable a mutual harmonisation between forging press and manipulator a proper description of the material being pressed between two flat dies is required. Moreover material does not only deform in the forging direction but also towards the manipulator. In order to fully exploit capabilities of forging equipment manipulator feeding rate or manipulator bite has to be determined. This can be achieved by employing the empirical formula proposed by Tomlinson and Stringer[3] which is based on assumption of constant volume during plastic deformation and describes the relationship between manipulator feeding rate, material shape and reduction for steel. The change of length and width of a forging can be described by a spread factor and the reduction ratio. From practical experience with programmed forging it is known that the influence of reduction ratio on the spread is negligible[4].

To compute the forging pass schedules for bars and predict the changes of shape as well as other important parameters during the forging process empirical formulae have been proposed. The pass procedure for the forging of final shape depends on initial and final cross section shape of bar and are: 1) from square stock to a square bar, 2) from square to round, 3) from round to square and round to round, where same forging principle is used. Breakdown procedure is as follows 1) square to square process goes through next shapes: square – rectangular – square where the reduction ratio can be varied every second pass. A square forged down to a rectangular section with a certain reduction ratio, turned 90° and forged down again with the same reduction ratio and the same bite ratio, turns automatically into a new square with smaller size. To obtain sharp corners of bar decrease of the reduction ratio is required. 2) The process square to round follows the same breakdown routine square – rectangular – square, ending in four passes with an octagon, which have about 7 % more area than the final round. Finish to the round is made in a swaging die. 3) Forging pass schedule of round to square and round to round follows the same forging principle. Forging of rectangular cross sections requires a different technology, where shape factor of h/w (height/width) plays important role leading to a variation of the spread factor. For example rectangular bars where a shape factor exceeds 1/6 results in the normal forging range practically no spread but only elongation[4].

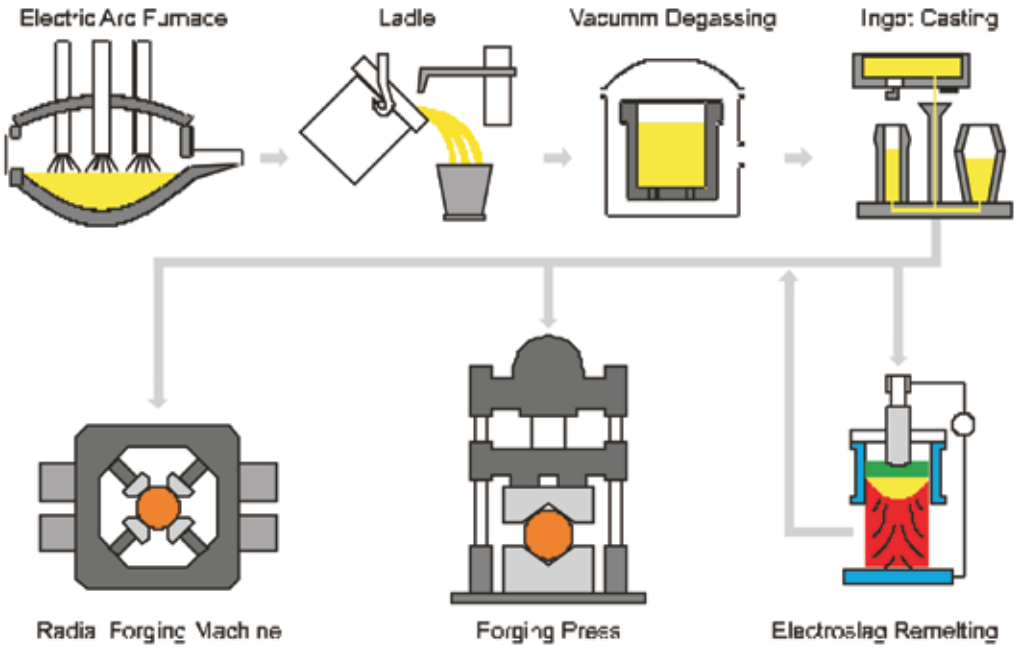

Figure 1. Material flow for open-die forged products
Slika 1. Tok materiala pri prostem kovanju

Ingots are extensively used as forging stock in the open-die forging of large components. In Figure 1 typical steelmaking material flow from electric arc furnace to forging press is shown. Whenever ingots are used it is often mandatory to adopt a forging procedure that will remove the cast structure in the finished forging.

Another important aspect of calculation and optimisation of apt pass schedule is to be aware of limits of ingots, products, materials and technology. When all properties are collected and stored to databases we can start calculating efficient pass schedule.

Use of computer aided technology, as depicted in Figure 2 for development and optimization of pass schedules in open-die forging requires some input of forging know-how. This applies particularly to the reduction factor which has to take care of the shape of the ingot, surface conditions, and brittleness of the material and in most cases must be varied with the dropping forging temperature. Also important is the bite ratio which defines the depth of deformation and grain change in the forging. Grater bite ratio is better but leads to increase of forging force, which is limited with equipment.

RESULTS AND DISCUSSION

HFS software fundamentals for calculation of pass schedules are models where some of them are physically based e.g. temperature. Other models are deductions

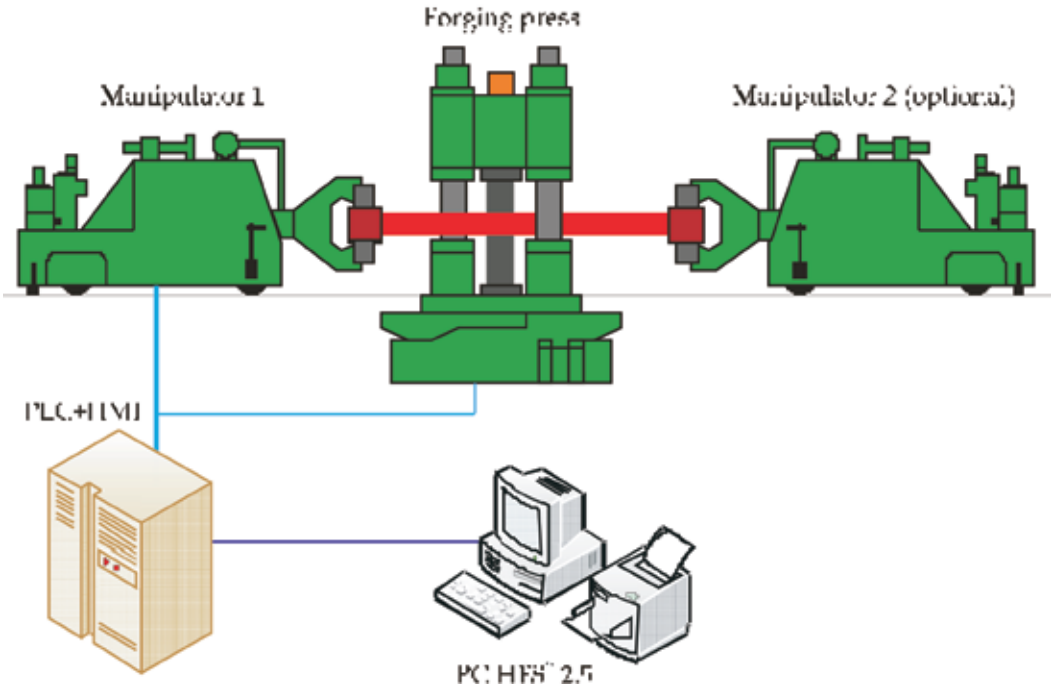

Figure 2. Modern open-die forging plant with additional PC for virtual aided technology
Slika 2. Moderen obrat kovačnice za prosto kovanje z dodatnim računalniškim vodenjem tehnologije

from experience e.g. material spreading. In software database also technological characteristics of the forging equipment e.g. maximum press force, press velocity and acceleration, manipulator velocity and acceleration, etc are stored. Users of HFS software have possibility and are limited to change only input data that are stored in input databases as follows. *Ingot database* where all geometrical characteristics of ingots are stored. *Product database* allows users to specify and store shape and dimensions of products. In *materials database* physical characteristics regarding hot workability, radiation and thermal properties for desired materials are stored. *Technological database* includes data linked to technological parameters used according to specific forging schedule e.g. shape and size of forging tool. For accurate pass schedule calculation user must constantly update parameters stored in input databases. Specifically important are parameters influencing calculation of temperature e.g. density, specific heat and radiation coefficient. Figure 3a shows influence on temperature calculation regarding specific heat, whereas in Figure 3b depicts influence of radiation coefficient on temperature respectively. Figure 3 shows that lowering specific heat coefficient decreases calculated temperature, on the other hand lowering radiation coefficient increases calculated temperature. All calculations plotted in Figure 3 were performed using upseted 24t ingot and material AISI H13.

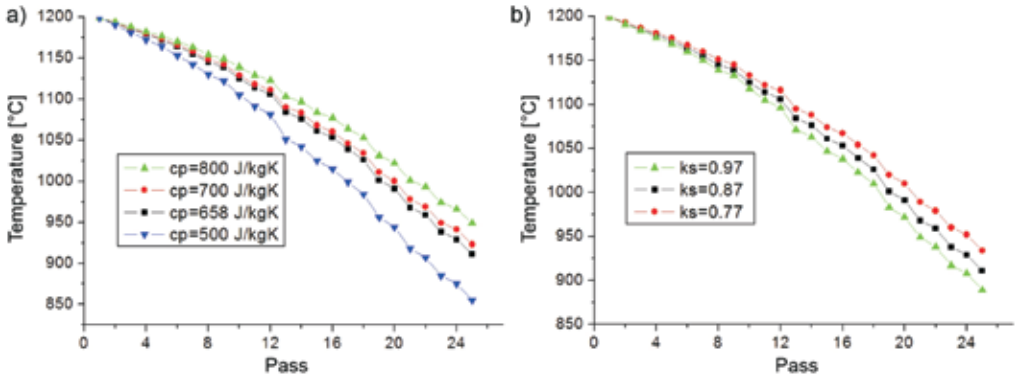

Figure 3. Influence of (a) specific heat and (b) radiation coefficient on temperature after passes while forging flat product from upseted 24t ingot to product dimensions of 1000×500

Slika 3. Vpliv (a) specifične toplote pri konstantnem tlaku cp in (b) koeficienta sevanja na potek temperature po različnih vtikih pri kovanju ploščatega izdelka iz 24t nakrčenega ingota za izdelek 1000×500

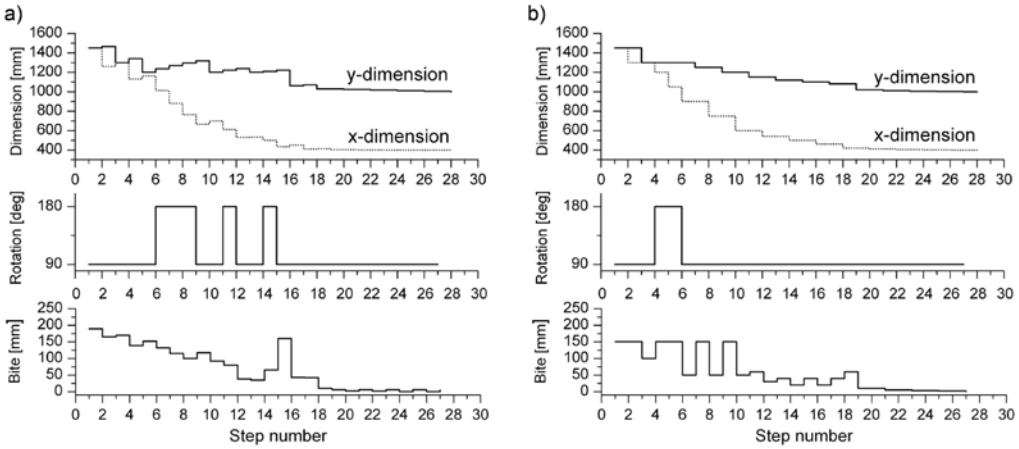

Figure 4. Graphical presentation of forging pass schedule for billet dimensions 1000×400; a) calculated pass schedule and b) acquainted forge masters pass schedule

Slika 4. Grafični prikaz plana vtikov za gredice dimenzije 1000×400; a) izračunan plan in b) izmerjen plan kovaških mojstrov

Table 1. Detailed characteristics of pass schedules for billet dimensions 1000×400
Tabela 1. Natančen prikaz planov vtika za gredico z dimenzijami 1000×400

Calculated pass schedule					Acquainted pass schedule				
Step	Height	Width	Bite	Rotation	Step	Height	Width	Bite	Rotation
1	1450	1450	189.43	90	1	1450	1450	150	90
2	1260	1464.07	164.61	90	2	1300	1450	150	90
3	1299.46	1299.46	169.76	90	3	1300	1300	100	90
4	1129.69	1339.02	139.02	90	4	1200	1300	150	180
5	1200	1164.22	152.1	90	5	1050	1300	150	180
6	1012.13	1236.74	132.23	180	6	900	1300	50	90
7	879.9	1268.24	114.95	180	7	1250	900	150	90
8	764.95	1295.32	99.93	180	8	750	1250	50	90
9	665.01	1317.36	117.36	90	9	1200	750	150	90
10	1200	700	91.53	90	10	600	1200	50	90
11	609.09	1220.84	79.57	180	11	1150	600	60	90
12	529.51	1238.28	38.28	90	12	540	1150	30	90
13	1200	533.68	34.7	90	13	1120	540	40	90
14	498.99	1207.66	65.19	180	14	500	1120	20	90
15	433.8	1221.09	159.53	90	15	1100	500	40	90
16	1061.57	451.5	42.74	90	16	460	1100	20	90
17	408.76	1070.83	42.05	90	17	1080	460	40	90
18	1028.78	413.58	10	90	18	420	1080	60	90
19	403.58	1028.78	6	90	19	1020	420	10	90
20	1022.78	403.58	2	90	20	410	1020	10	90
21	401.58	1022.78	6	90	21	1010	410	5	90
22	1016.78	401.58	1.58	90	22	405	1010	5	90
23	400	1016.78	6	90	23	1005	405	3	90
24	1010.78	400	0	90	24	402	1005	3	90
25	400	1010.78	6	90	25	1002	402	2	90
26	1004.78	400	0	90	26	400	1002	2	90
27	400	1004.78	4.78	90	27	1000	400	0	90
28	1000	400			28	400	1000		

HFS simulator allows prediction and verification of pass schedules for automatically and manually operated open-die forging technology. To certify and confirm calculations of recently developed virtual aided tool for simulation of hot open die forging, HFS, a comparison of calculated and industrial pass schedules is necessity. For later pass schedules of most experienced forge masters from industry were selected. Industrial equipment used to validate accuracy of developed software package was a forging plant with 25/30 MN forging press and one railbound forging manipulator.

The calculated forging plan shows good correlation with the acquainted forging plan as one can see from comparison of Figure 4a and Figure 4b and Figure 5a and Figure 5b. The bite rate is much more equally distributed through the passes. The 180° rotation of the billet is more often used compared to acquainted plan. This results in a straighter billet because the deformation is more evenly distributed. The HFS calculated forging plan also takes into account the spread of billet in the direction normal to forging direction as can be seen as the increase of dimension in direction square to forging direction in Figure 3a and in Figure 4a. Detailed values for forging pass schedule for billet with dimensions 1000×400 are given in Table 1 and for billet with dimensions 1000×500 in Table 2.

In Tables 1 and 2 the calculated pass schedule appears to be as good as that of the best forge master and in some cases even better regarding number of pass steps to obtain final dimensions. HFS also calculates spreading later used for press management and much more accurate and therefore the calculated dimensions for height and width are given in decimal numbers. Forge masters pass schedule does not consider spreading and the values were measured by press control program and are therefore rounded.

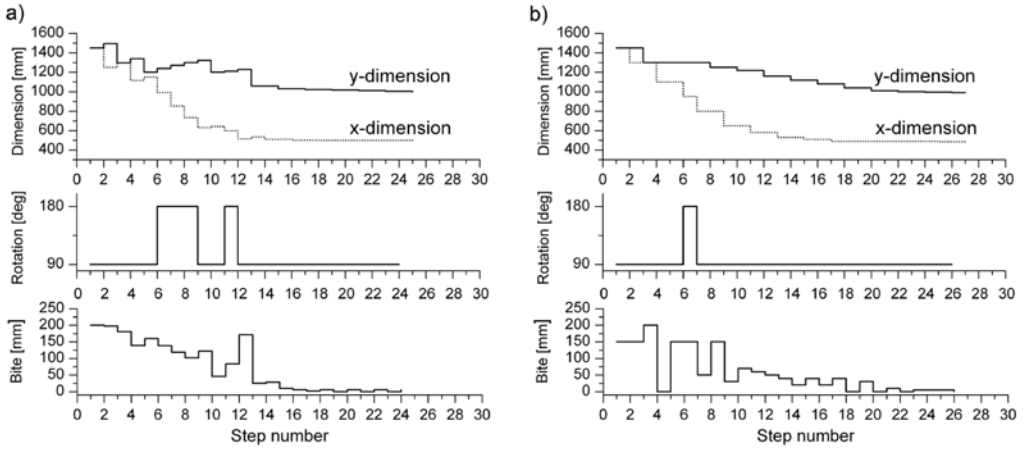

Figure 5. Graphical presentation of forging pass schedule for billet dimensions 1000×500; a) calculated pass schedule and b) acquainted forge masters pass schedule

Slika 5. Grafični prikaz plana vtikov za gredice dimenzije 1000×500; a) izračunan plan in b) izmerjen plan kovaških mojstrov

Table 2. Detailed characteristics of pass schedules for billet dimensions 1000×500
Tabela 2. Natančen prikaz planov vtika za gredico z dimenzijami 1000×500

Calculated pass schedule					Acquainted pass schedule				
Step	Height	Width	Bite	Rotation	Step	Height	Width	Bite	Rotation
1	1450	1450	200	90	1	1450	1450	150	90
2	1250	1494.48	197.62	90	2	1300	1450	150	90
3	1296.86	1296.86	180.64	90	3	1300	1300	200	90
4	1116.22	1339	139	90	4	1100	1300	0	90
5	1200	1150.94	160.32	90	5	1300	1100	150	90
6	990.62	1238.72	138	180	6	950	1300	150	180
7	852.63	1271.57	118.77	180	7	800	1300	50	90
8	733.87	1299.52	102.22	180	8	1250	800	150	90
9	631.65	1322.03	122.03	90	9	650	1250	30	90
10	1200	644.21	45.54	90	10	1220	650	70	90
11	598.67	1210.37	83.39	180	11	580	1220	60	90
12	515.28	1228.71	171.15	90	12	1160	580	50	90
13	1057.56	534.22	24.94	90	13	530	1160	40	90
14	509.27	1057.56	28.38	90	14	1120	530	15	90
15	1029.17	511.95	10	90	15	515	1120	40	90
16	501.95	1029.17	6	90	16	1080	515	10	90
17	1023.17	501.95	1.95	90	17	505	1080	40	90
18	500	1023.17	6	90	18	1040	505	0	90
19	1017.17	500	0	90	19	505	1040	20	90
20	500	1017.17	6	90	20	1020	505	0	90
21	1011.17	500	0	90	21	505	1020	10	90
22	500	1011.17	6	90	22	1010	505	0	90
23	1005.17	500	0	90	23	505	1005	5	90
24	500	1005.17	5.17	90	24	1000	505	5	90
25	1000	500			25	500	1000	0	90
					26	1000	500	0	90
					27	500	1000		

A case study comparison was made between a calculated and measured pass schedule for two different billet sizes. The calculated pass schedule shows good correlations with the measured one and is in some cases even better than that of the best forge masters, resulting in less passes needed for reaching the end dimensions of the forged billet. The bite rate in calculated pass schedule is much more evenly distributed between the passes thus resulting in more evenly distributed deformation and should provide better material properties and minimise the risk of an onset of cracks.

Ability of HFS is also spread calculation of a billet. This can be later on used for a complete automation of a forging press leading to minimisation of the cost of open-die forging process and increase the yield.

Conclusions

Efforts to increase productivity and improve quality of technological processes are of a high importance in open-die forging. The investments costs of open-die forging equipment are high and profitability depends to large extent on intensive and flexible use. Automatic forging sequences ensure higher productivity and better quality of products. The developed software for open-die forging HFS allows the calculation of pass schedules and gives support for selection and verification of optimal pass schedule. Technology engineer using the HFS program has a good control over open-die forging process, thus resulting in an opportunity to select optimal process parameters for each product and material. Accuracy of calculated pass schedules largely depends on accurate initial data needed in HFS software.

Analysis and detailed comparison of data obtained online in open-die forging plant and calculated offline using HFS software shows good agreement. We believe that are possible further technological optimizations of pass schedules and therefore savings when technologists familiar with open-die process and equipment abilities when HFS in used.

Povzetek

Orodje za programsko vodeno prosto kovanje – študija primera

Poizkusi za povečanje produktivnosti in izboljšanje kvalitete tehnoloških procesov so izrednega pomena v obratih prostega kovanja. Cene investicij za opremo, ki je potrebna za prosto kovanje so izredno visoke zato je dobičkonosnost odvisna predvsem od razširjenosti in fleksibilnosti uporabe. Avtomatizirni postopki kovanja zagotavljajo večjo produktivnost in boljšo kvaliteto končnih izdelkov.

Z razvita programsko opremo HFS je moč izračunati plan vtikov in s tem nudi oporo pri optimalni izbiri plana. Tehnolog, kateremu je v pomoč HFS, ima dobro kontrolo nad procesom prostega kovanja. Tako se lahko osredotoči na izbiro optimalnih parametrov za vask proizvod in material. Natančnost izračuna s programom HFS pa

je v veliki meri odvisna od natančnsti začetnih podatkov v programu.

Narejena je bila študija primera med izračunanim in izmerjenim planom vtika za dve različni dimenziji gredic. Izračunan plan kaže dobro ujemanje s planom, ki je bil izmerjen pri ekipi najboljših kovaških mojstrov. V nekaterih primerih je ta celo boljši, saj je bilo potrebnih manj vtikov za dosego končnih dimezij.

Stopnja odvzema je pri izračunanem planu bolj enakomerno razporejena med prevleki. S tem je dosežena tudi bolj enakomerna razporeditev deformacije med prevleki, kar ima za posledico boljše materialne lastnosti in preprečuje vrjetnost nastanka razpok.

Program HFS izračunava in upošteva tudi širjenje gredice. Vse te lastnosti je moč uporabiti kasneje za avtomatizacijo preše za prosto kovanje. To bi zmanjšalo stroške prostega kovanja in povečalo končni izplen.

References

[1] Aksakal, B., Osman, F.H., Bramley, A.N. (1997): Upper-bound analysis for the automation of open-die forging. *Journal of Materials Processing Technology*.; Vol. 71, pp. 215-223.

[2] Choi, S.K., Chun, M.S., Van Tyne, C.J., Moon, Y.H. (2006): Optimization of open die forging of round shapes using FEM analysis. *Journal of Materials Processing Technology*.; Vol. 172, pp. 88-95.

[3] Tomlinson, A., Stringer, J.D. (1959): Spread and elongation in flat tool forging. *Journal of Iron Steel Institute*.; Vol. 193-2, pp. 157-162.

[4] Phanke, H.J. (1983): Grundlagen des programmierten Schmidens. *Stahl und Eisen*.; Vol. 103, pp. 547-552.

A laboratory test for simulation of solidification on Gleeble 1500D thermo-mechanical simulator

Laboratorijski test simulacije strjevanja na termo-mehanskem simulatorju Gleeble 1500D

Boštjan Bradaskja[1], Jurij Koruza[2], Matevž Fazarinc[2], Matjaž Knap[2], Radomir Turk[2]

[1]ACRONI d.o.o., Cesta Borisa Kidriča 44, SI-4270 Jesenice, Slovenia;
E-mail: bostjan.bradaskja@acroni.si
[2]University of Ljubljana , Faculty of Natural Sciences and Engineering,
Departmant of Materials and Metallurgy, Aškerčeva cesta 12, SI-1000 Ljubljana, Slovenia;
E-mail: jurij.koruza@ntf.uni-lj.si, matevz.fazarinc@ntf.uni-lj.si,
matjaz.knap@ntf.uni-lj.si, rado.turk@ntf.uni-lj.si

Received: November 18, 2007 **Accepted:** January 7, 2008

Abstract: A highly repeatable solidification test was developed. It was designed to study the effect of process parameters on solidified micro and macrostructures. Different cooling rates were used for solidification and cooling of S 355 J2 construction steel. It was observed that cooling rate has a substantial influence on final grain size and on columnar-to-equiaxed transition zone (CET). Within the interval of constant thermal gradient, different macro- and micro-structural features have been provided, which consequently enables the study of dynamics of precipitation dependence on solidification processing parameters.

Izvleček: Razvit je bil visoko ponovljiv test strjevanja. Razvit je bil kot orodje, za preučevanje vpliva procesnih parametrov na lito mikro in makrostrukturo. Za strjevanje konstrukcijskega jekla S 355 J2 so bile uporabljene različne ohlajevalne hitrosti. Opažen je bil močan vpliv ohlajevalne hitrosti tako na končno velikost zrn, kot tudi na mejno plast med stebričastimi in ekviaksialnimi zrni. Znotraj intervala, kjer je bil temperaturni gradient konstanten, so bile s pomočjo različnih ohlajevalnih hitrosti, v vzorcih dobljene različne mikro in makrostrukturne značilnosti, kar omogoča študij dinamike izločanja v odvisnosti od parametrov strjevanja.

Key words: solidification test, macrostructure, cooling rate, Gleeble
Ključne besede: test strjevanja, makrostruktura, ohlajevalna hitrost, Gleeble

Scientific paper

Introduction

The solidification of molten steel is one of the most important processes in the processing path of steel manufacturing. The microstructure that derives from the solidified ingot or slab has a large influence on the characteristic of the produced material and process path that follows.

The micro and macrostructures in ingots usually show spatial variations of features and properties. This can be simulated with combination of computer simulation of ingot/slab cooling and high temperature testing with controlled solidification and cooling of the specimens.

The high temperature experiments on the Gleeble testing machine that were found in literature are mainly focused on characteristics of metal in the mushy zone or the mechanical properties of solidified specimens for continuous casting application and do not deal with the development of microstructure. The investigations have not been focused on influence of process parameters on development of micro and macrostructure. In these tests, the solidification process was only the first stage followed by tensile mechanical loading and no observations of solidified structure were made.

Seol et al.[1,2] were studying the behavior of material under tensile loading of in-situ melted and solidified cylindrical specimens. The tensile strength and ductility of carbon steels was measured in the temperature range of mushy zone. Also the stress – strain relations in austenite and δ-ferrite phase regions at various temperatures and strain rates were analyzed. Na et al.[3] used the Gleeble system to investigate cracking occurrence during continuous casting of steels by tensile testing. In this work effects of carbon content, strain rate and sampling orientation on hot ductility were investigated. Glowacki et al.[4] used tensile test to study the deformation behavior of steel within the mushy zone. Suzuki et al.[5-7] employed different methods of laboratory simulation of continuous casting and direct rolling of steels with special emphasis on embrittlement in dependence to chemical composition, thermal history, strain rate and fracture mode.

Nevertheless some investigations were made on development of solidified microstructure of aluminum alloys, using the Gleebe system, by Kostrivas and Lippold[8]. Although the testing procedure was similar, the difference between the physical properties of aluminum and steel brings up new problems and requires some different approaches.

Because of the above mentioned reasons it was decided that a highly repeatable solidification test should be developed with accurate knowledge and control of the temperature field in the specimen. The test was developed using a Gleeble 1500D thermo-mechanical simulator. This machine enables simultaneous, computer guided, thermal and mechanical loading of the specimen, within a very precise range. The main goal was to track the development of micro and macrostructure in dependence to testing parameters.

Experimental procedure and material

The laboratory test for controlled solidification has been developed using Gleeble 1500D thermo-mechanical simulator, which has been equipped with specially developed additional parts for solidification simulation.

Cylindrical specimens, 110 mm long with a diameter of 10 mm, as shown in Figure 1 were used for the experiments. A 10 mm screw-thread was engraved on each side of the specimen which enabled the fixation of the specimen into the jaws with aim to perform tensile and compression loadings. To support the melt zone a 30 mm quartz crucible with a 1 mm wall thickness has been placed around the center part of the specimen. Quartz material was used because of its high temperatures endurance, small linear coefficient of thermal expansion and negligible diffusion with the specimen material. Crucibles have been furnished with axially running 2 mm slot for insertion of the thermo couples and also to provide an opening for exiting gasses. To decrease the radial thermal gradient, refractory material was placed over the crucible. Additionally two special water-cooling ribs made from copper were placed on each side of the specimen, to attain sufficient thermal gradient in axial direction. Varying the position of the ribs enabled the control of the axial thermal gradient and consequently the width of the melting zone. Schematic plan of placing of the specimen is shown on Figure 2.

Temperature was controlled by 0.35 mm thick S-type (Pt10wt%Rh-Pt) thermocouple, spot-welded in the middle of the specimen and isolated with alumina tubes. An additional thermocouple stand was applied to prevent the motion of the leading thermocouple and to assure the correct temperature measurements during the upset of liquid phase. In order to minimize the surface oxidation and consequently the detachment of the welded thermocouple, all experiments were conducted in protective Ar atmosphere.

Before setting up the temperature program for the test, Thermo-Calc software was used to define the liquidus and solidus temperature of the material studied. The specimen was heated with the heating rate of 15 K/s up to 100 K below liquidus temperature. The heating rate was then decreased to 1 K/s for better control of temperature near the melting temperature. If necessary, the

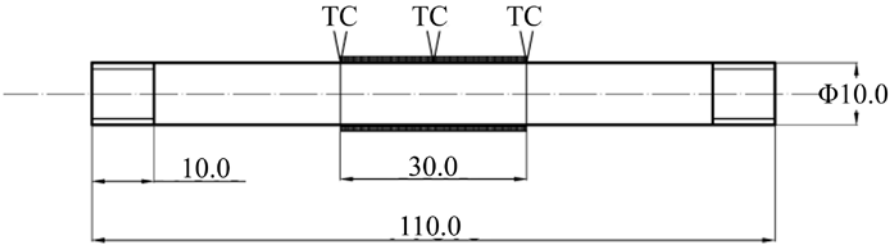

Figure1. Cross section of the specimen
Slika 1. Shematski načrt preizkušanca

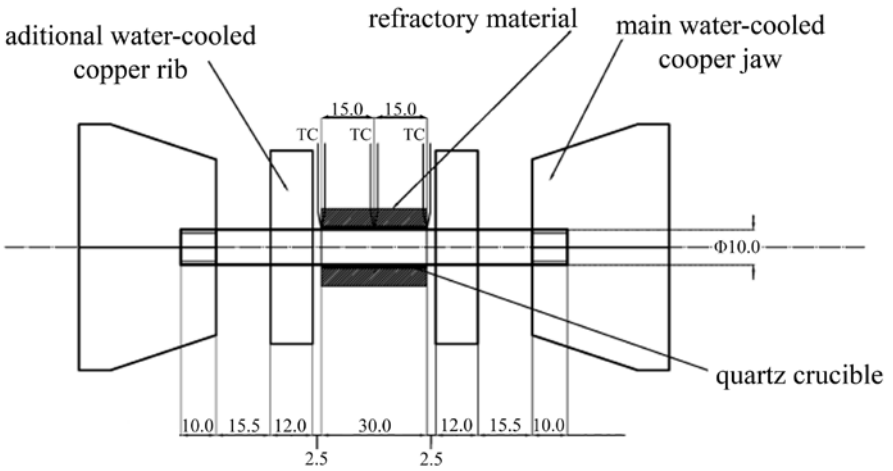

Figure 2. Schematic plan of the mounted specimen
Slika 2. Shematski načrt namestitve preizkušanca

temperature was raised manually to attain the desired width of the melted zone. For stabilization of melted zone the specimen was held at the liquidus temperature for 30 - 40 seconds. Afterwards it was cooled with a predefined cooling rate between 1 K/s and 10 K/s.

During the cooling an adequate mechanical program was applied with the movement of the main jaws to compensate solidification shrinkage and to prevent formation of cracks. Value of stroke depends on the material properties and the width of the melt zone. After the whole volume has been solidified, a constant compression loading was applied to prevent appearance of cracks caused by further temperature shrinkage of material.

In order to evaluate the developed equipment the construction steel, S 355 J2, with chemical composition listed in Table 1, was selected.

After the tests, the solidified samples were sectioned longitudinally and axially along their mid-plane for metallographical observation. To reveal the macrostructure and microstructure, 10 % HNO_3 and 2 % HNO_3 etching agents were used, respectively. The etched specimens were examined by means of optical microscopy using Olympus SZX12 binocular and Olympus BX51M optical microscope.

Results and discussion

The axial thermal gradient was adjusted by setting two additional cooling ribs at different positions from the center of the specimen. By this way the solidification conditions (steepness of the gradient) can be controlled. Figure 3 represents the measured axial temperature difference at different positions of cooling ribs: 17.5, 20.0 and 25.0 mm from each side of the center of the specimen. Thermocouples were spot

Table 1. Chemical composition of the S 355 J2 steel in wt. %
Tabela 1. Kemijska sestava jekla S 355 J2 v ut.%

Element	C	Si	Mn	P	S	Al	Nb
wt. %	0.15	0.45	1.03	0.012	0.001	0.028	0.019

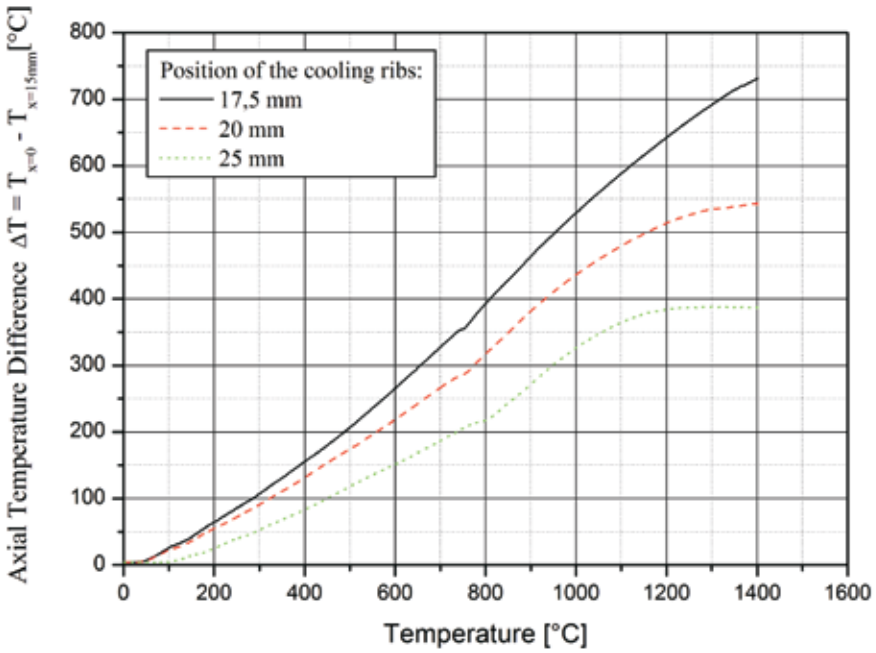

Figure 3. Comparison of axial temperature difference measured between the center part of the specimen and 15 mm from the center along the axis of the specimen, using different placements of the water-cooled copper ribs (17.5, 20, and 25 mm from the center of the specimen)
Slika 3. Primerjava temperaturnih razlik izmerjenih med sredino vzorca ter 15 mm od sredine vzorca v osni smeri vzorca, v odvisnosti od postavitve dodatnih hladilnih reber (postavitev 17,5, 20 in 25 mm od sredine vzorca)

welded on the surface of the specimen as could be seen on Figure 2. The specimen was isolated with refractory material.

The effect of the refractory material on the radial temperature difference between the surface and the center of the specimen was measured for the isolated and unisolated specimen. The results are shown in Figure 4. This difference was measured using the same technique as described by GLOWACKI et al.[4].

With isolation the heat loss through the surface was minimized and consequently more directional solidification achieved.

Four isolated specimens were melted and solidified using different cooling rates, 1 K/s, 3 K/s, 5 K/s and 10 K/s. For comparison, one experiment without isolation and with cooling rate of 3 K/s was carried out. The obtained macrostructures in axial and radial cross-section are presented in Figure 5a-d for isolated specimens and in Figure 5e for un-isolated specimen. Position of the cooling ribs was the same in all experiments that is 17.5 mm from the center on each side as shown on Figure 2. The width of the melted zone was between 12 and 15 mm and was surrounded by 5 to 8 mm wide heat affected zones on each side.

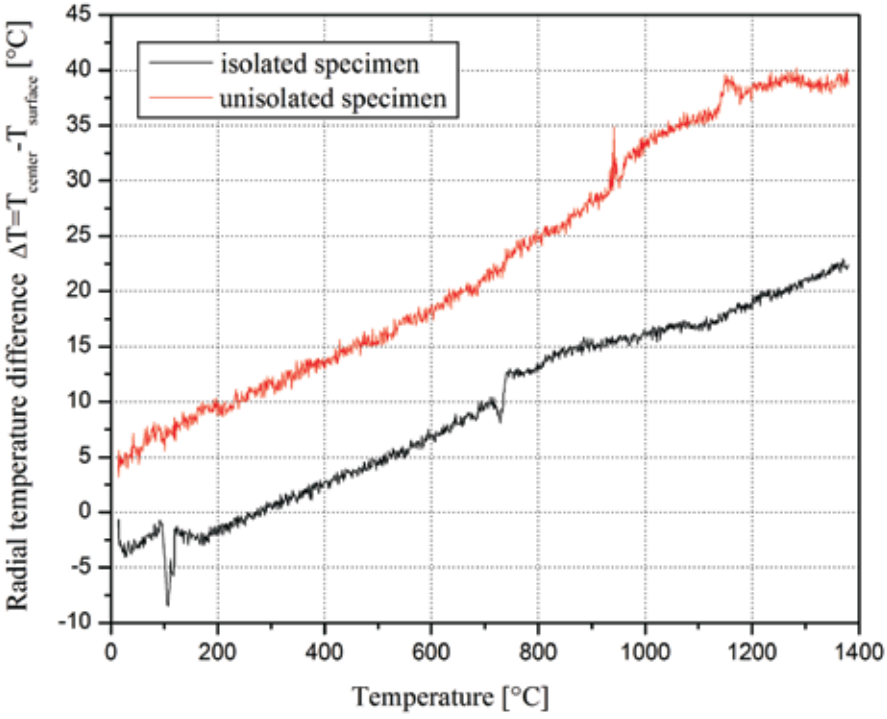

Figure 4. Comparison of the measured radial temperature difference between isolated and un-isolated specimens
Slika 4. Primerjava radialne temperaturne razlike med izoliranim in neizoliranim vzorcem

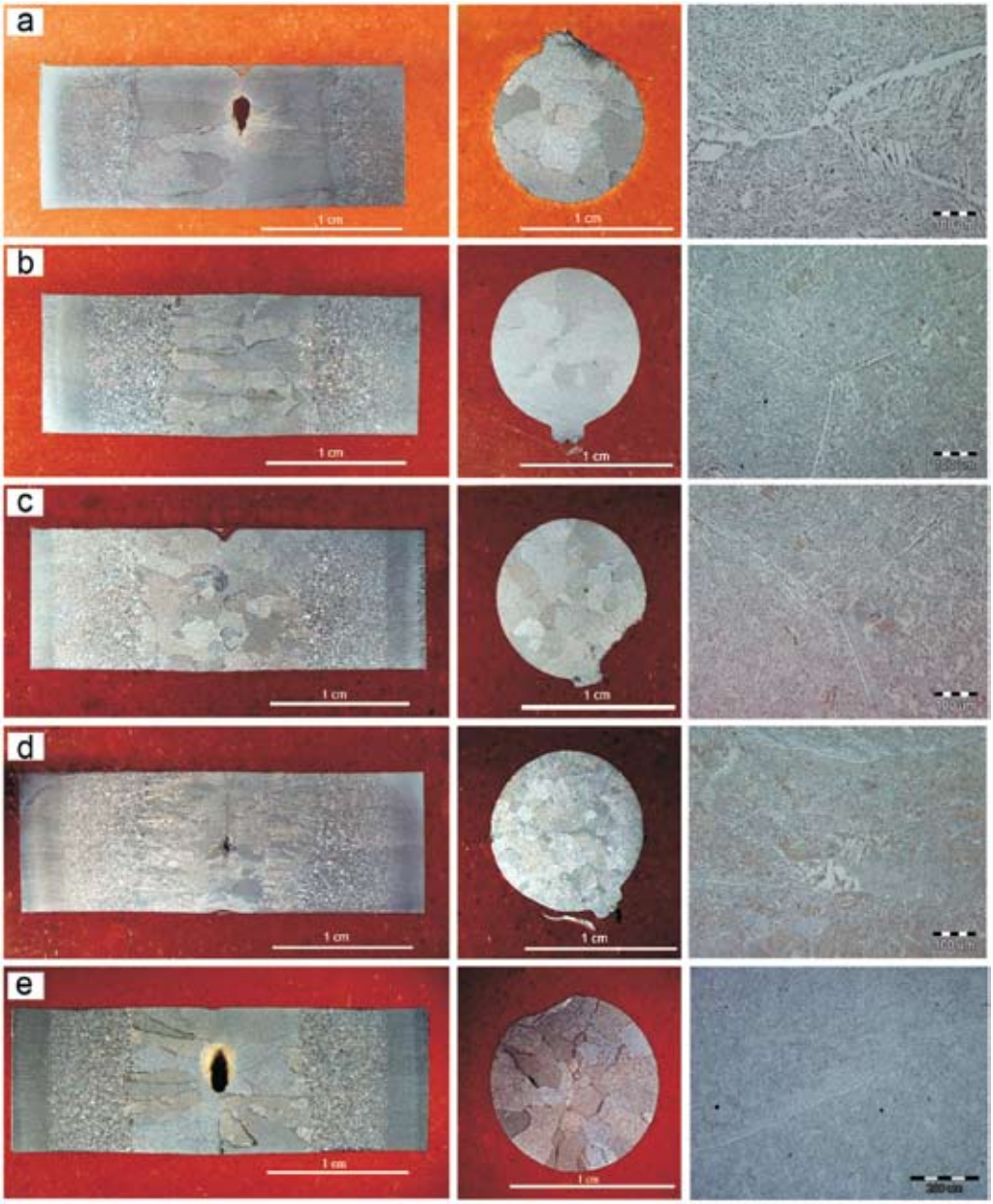

Figure 5. Longitudinal and axial cross-section of the isolated specimens with cooling rates 1 °C/s, 3 °C/s, 5 °C/s, 10 °C/s from a) to d) respectively and an un-isolated specimen e) with cooling rate 3 °C/s

Slika 5. Vzdolžni ter prečni prerez vzorcev s pripadajočo mikrostrukturo: a) hitrost ohlajanja 1 °C/s, b) hitrost ohlajanja 3 °C/s, c) hitrost ohlajanja 5 °C/s, d) hitrost ohlajanja 10 °C/s, e) hitrost ohlajanja 3 °C/s. Vzorci od a) do d) so bili izolirani, vzorec e) je bil strjen brez izolacije

Lower cooling rates caused the formation of columnar grains which can be observed in the macrostructures presented in the Figure 5a-d. These grains start to form on the solid material on the edge of the melted zone and grow into the center of the melt, in the opposite direction of the heat flow.

With increase of the cooling rate the solidification time shortens which resulted in increased number of smaller sized grains (Figure 5a-d). Above a certain threshold of cooling rate, as seen in Figure 5d, a relatively large amount of latent heat is momentarily set free. The heat flow is not sufficient thus the cooling rate of the remained liquid in the center of the specimen is reduced. Therefore the center of the specimen is solidified with a slower cooling rate. Consequently the observed solidified structure consists of two different grain structures where the CET zone is clearly seen. The first grains are columnar and are more numerous than those obtained from the specimens solidified with slower cooling rate. The second type of grains is more globular type and is solidified last. These grains did not solidify directionally.

In order to investigate the effect of the isolation on macro- and microstructure, one specimen was solidified without isolation. The cooling rate was 3 °C/s and the macrostructure is shown on Figure 5e. Because of the large radial heat loses due to radiation the solidification was not directional and there was also a large shrinkage cavity. The surface was solidified prior to the center of the specimen and the lack of the material appears because it could not be compensated by compression loading. The grain size does not differ from that obtained from the specimen which was solidified with isolation.

Conclusions

A solidification test was developed, using thermo-mechanical simulator Gleeble 1500D which enables simultaneous computer guided mechanical and thermal loading.

Additional cooling ribs were used to control the axial thermal gradient. With varying the position of these ribs different temperature fields were obtained. The radial temperature difference was minimized by means of refractory material, placed around the quartz crucible. With an additional test without refractory material it was proven that solidification was not unidirectional and a large shrinkage cavity was observed.

A comparison between four samples solidified and cooled with different cooling rates was made. It was observed that cooling rate has a substantial influence on final grain size. With increasing the cooling rate the grains are found to be smaller. CET zone was also observed in the sample that was cooled with the highest cooling rate.

Povzetek

Laboratorijski test simulacije strjevanja na termo-mehanskem simulatorju Gleeble 1500D

Razvit je bil test za strjevanje kovinskih materialov. Test je bil razvit kot dodatek termo-mehanskemu simulatorju metalurških stanj, Gleeble 1500D, ki omogoča simultano računalniško vodenje temperaturnega in mehanskega programa obremenjevanja vzorca.

Z dodatnimi, vodno hlajenimi, bakrenimi, hladilnimi rebri je bil kontroliran aksialni temperaturni gradient. S premikanjem leteh je moč doseči različna temperaturna polja. Radialni temperaturni gradient je bil zmanjšan z uporabo ognjevzdržnega materiala, ki je obdajal kvarčno cevko. Z dodatnim testom, ki je bil izveden brez ognjevzdržnega materiala, je bilo pokazano, da strjevanje ni potekalo usmerjeno, oziroma ni bilo enoosno.

Narejena je bila primerjava med štirimi vzorci, strjenimi in ohlajenimi z različnimi ohlajevalnimi hitrostmi. Opaženo je bilo, da ima ohlajevalna hitrost močan vpliv na končno velikost zrn. Z povečevanjem ohlajevalne hitrosti so zrna postajala manjša, v vzorcu, ki je bil ohlajen z najvišjo hitrostjo, pa je moč opaziti prehodno cono med stebričastimi in ekviaksialnimi kristali.

References

[1] Seol, D.J., Won, Y.M., Oh, K. H., Shin, Y.C. and Yim, C.H. (2000): Mechanical Behaviour of Carbon Steels in the Temperature Range of Mushy Zone. *ISIJ International*.; Vol. 40, No. 4, pp. 356-363.

[2] Seol, D. J., Won, Y.M., Yeo, T., Oh, K.H., Park, J.K. and Yim, C. H. (1999): High Temperature Deformation Behavior of Carbon Steel in the Austenite and δ-Ferrite Regions. *ISIJ International*.; Vol. 39, No. 1, pp. 91-98.

[3] Na, W., Zijiu D., Weichang, C., Yan, Z. (1989): Hot Ducility of Continuous Casting Carbon Steel. *SPT3*.; vol. 10-12, Vienna.

[4] Glpwacki, M., Malinowski, Z., Hojny, M., Jedrzejczyk, D. (2004): The phisical and mathematical modelling of plastic deformation of samples with mushy zone. *Inverse Problems, Design and Optimization Symposium*. Rio de Janeiro, Brazil.

[5] Suzuki, H.G., Nishimura, S. and Yamaguchi, S. (1988): Physical Simulation of the Continuous Casting of Steel. *The International Symposium on Physical Simulation of Welding, Hot Forming and Continuous Casting held in Ottawa*. Canada.

[6] Suzuki, H.G., Nishimura, S. and Yamagutchi, S. (1984): Improvement of Hot Ductility of Continuously Cast Carbon Steels. *Transactions ISIJ*.; Vol. 24, pp. 54-59.

[7] Suzuki, H.G., Nishimura, S. and Yamagutchi, S. (1982): Charac-

teristics of Hot Ductility in Steels. *Transactions ISIJ*.; Vol. 22, pp. 48-56.

[8] KOSTRIVAS, A. and LIPPOLD, J.C. (2000): A Method for Studying Weld Fusion Boundary Microstructure Evolution in Aluminum Alloys. *Welding Research Supplement*. pp. 1-8.

Comparative test of active and passive multichannel analysis of surface waves (MASW) methods and microtremor HVSR method

Primerjalni test aktivne in pasivne večkanalne analize površinskih valov (MASW) ter metode mikrotremorjev (HVSR)

Andrej Gosar[1,2], Robert Stopar[3], Janez Rošer[2]

[1]Environmental Agency of the Republic of Slovenia, Seismology and Geology Office, Dunajska cesta 47, SI-1000 Ljubljana, Slovenia, E-mail: andrej.gosar@gov.si
[2]University of Ljubljana, Faculty of Natural Sciences and Engineering, Aškerčeva cesta 12, SI-1000 Ljubljana, Slovenia; E-mail: janez.roser@ntf.uni-lj.si
[3]Geoinženiring d.o.o., Dimičeva ulica 14, SI-1000 Ljubljana, Slovenia; E-mail: robert.stopar@geo-inz.si

Received: December 5, 2007 **Accepted:** January 15, 2008

Abstract: Shallow shear-wave velocity structure is important for seismological ground motion studies and for geotechnical engineering, but it is quite difficult and expensive to derive by using conventional geophysical techniques. Multichannel analysis of surface waves (MASW) and microtremor methods are therefore a valuable alternative developed in the last decade. A test of active and passive MASW and microtremor HVSR method was conducted in the southern part of Ljubljana which is characterised by soft sediments and strong seismological site effects. Land streamer which allows fast movement of geophones array in the field was successfully applied for the first time. Shear-wave velocities in the range 50-200 m/s were obtained in the 25 m thick layer of Quaternary sediments overlying Palaeozoic bedrock. The correspondence of velocity profiles obtained with different methods was satisfactory. Active MASW proved most useful in a case of target depth which does not exceed 30 m and passive MASW for greater depths. The advantage of microtremor HVSR is that it yields direct estimate of the fundamental resonance frequency of the sediments.

Izvleček: Hitrost strižnih seizmičnih valov v površinskih plasteh je pomembna za seizmološke analize nihanja tal ob potresu in v geotehniki, vendar pa jo je dokaj težko in drago določiti z uveljavljenimi geofizikalnimi metodami. V zadnjem desetletju pa so razvili nove metode večkanalne analize površinskih valov (MASW) in spektralnih razmerij mikrotremorjev (HVSR). V južnem delu Ljubljane, za katerega so značilni mehki sedimenti in izra-

Scientific paper

ziti lokalni seizmološki vplivi na potresne valove, smo izvedli test aktivne in pasivne MASW metode ter metode mikrotremorjev. Pri tem smo prvič uporabili »land streamer«, ki omogoča hitro premikanje geofonov na terenu. V 25 m debeli plasti kvartarnih sedimentov, ki prekrivajo paleozojsko podlago smo ugotovili hitrosti strižnih valov v razponu 50-200 m/s. Ujemanje hitrostnih profilov določenih z različnimi metodami je bilo zadovoljivo. Pokazalo se je, da je aktivna MASW metoda najbolj uporabna na območjih, kjer ciljna globina ne presega 30 m, pasivna MASW metoda pa tudi pri večjih globinah. Prednost metode mikrotremorjev (HVSR) je, da daje neposredno oceno osnovne resonančne frekvence sedimentov.

Key words: multichannel analysis of surface waves (MASW), microtremors, horizontal-to-vertical spectral ratio (HVSR), Rayleigh waves, shear-wave velocity, Ljubljana Moor

Ključne besede: večkanalna analiza površinskih valov (MASW), mikrotremorji, spektralno razmerje horizontalne in vertikalne komponente (HVSR), Rayleighovi valovi, hitrost strižnih valov, Ljubljansko barje

INTRODUCTION

Determination of a shallow shear-wave velocity structure is important for any quantitative microzonation study in seismic hazard assessment. The soil classification is according to Eurocode 8 standard for the design of earthquake resistant structures (EUROCODE 8, 2003) based primarily on average shear-wave velocity in the upper 30 m of the soil profile ($V_{S,30}$). If this is not available, the results of the Standard Penetration Test (N_{SPT}) or shear modulus (c_u) are also used. All are directly linked to a material's stiffness. From the seismological point of view the shear-wave velocity is the best indicator. Besides determination of a ground type the shear-wave velocity is a critical input parameter for any numerical ground motion simulation and estimation of site amplification. Since it is directly related to the shear modulus, it is also very important in geotechnical engineering and environmental studies.

The conventional approaches for near-surface shear-wave velocity investigations have been shear-wave seismic refraction method and down-hole velocity measurement in boreholes. Seismic signals from these surveys consist of wavelets with frequencies usually higher than 30 Hz. Application of both methods is relatively expensive in terms of field operation, data analysis and overall costs to be adequately included in microzonation studies. Usually such studies should cover large urbane areas and therefore require a pattern of measurements which is dense enough for a given geological setting to be representative. The obvious drawback of a down-hole method is the high cost of drilling. Seismic refraction method is also time consuming because it should be conducted separately using longitudinal- (P) and shear- (S) waves using two sets of geophones (vertical and horizontal) and different ways of signal generation by a sledgehammer. The P-waves are needed to determine the depth

structure and the S-waves to obtain relevant velocities for seismological site characterisation. In noisy urban environment, it is often difficult to generate enough strong signal to be effective.

In the last decade a new method called Multichannel Analysis of Surface Waves (MASW) was developed (Park et al., 1999; Wightman et al., 2002) which has several advantages in comparison to conventional seismic refraction and borehole measurements in determination of a shallow shear-wave velocity structure. It is based on the study of the dispersion of surface seismic (mainly Rayleigh) waves. These waves have much lower frequencies (e. g. 1-30 Hz) than body waves used in conventional seismic investigations. The sampling depth of a particular frequency component of surface waves is in direct proportion to its wavelength. This property makes the surface wave velocity frequency dependent, i. e. dispersive. The shear-wave velocity structure can be therefore obtained by the inversion of surface-waves dispersion curve (Xia et al., 1999), depending how the surface waves are generated active and passive MASW techniques are known (Park et al., 2007). In active MASW method the surface waves are generated through an impact source like a sledgehammer, similar as in refraction seismic method. On the other hand the passive MASW method utilizes surface waves generated passively (seismic noise) by natural (tidal motion, sea waves, wind, rivers) or artificial (traffic, industry) activities.

Ambient vibrations (seismic noise of natural and artificial origin) are used also in microtremor method. In this method microtremors are recorded with single three-component seismometer and analyzed in a frequency domain. Spectral ratio between the records on horizontal and vertical component yield fundamental frequency of soft sediments deposited over hard bedrock. The method is therefore called Horizontal to Vertical Spectral Ratio (HVSR) method. It is used mainly in quantitative microzonation to identify the areas where the danger of resonance between sediments (soil) and buildings exist. This method does not provide directly shear-wave velocity structure, but this can be derived by modelling of spectral ratio curve if necessary.

For the Ljubljana (the capital of Slovenia) region a new quantitative microzonation based on microtremor measurements in a very dense grid of 200 m x 200 m (Figure 1) is in preparation (Gosar, 2007b). Particular attention is given to the southern part of Ljubljana, which is built on very soft lacustrine and marsh deposits of the Ljubljana Moor where strong site effects can be expected. Most of this area is based on preliminary data classified as Eurocode 8 ground type S_1 (Zupančič et al., 2004). For S_1 and S_2 ground types Eurocode 8 standard does not give soil factors but prescribes site investigations to derive the amplification factor. Therefore we decided to perform a comparative test of two different MASW methods and microtremor method to asses their applicability for further investigations in this area. The test site was located near Ljubljanica river on Dolgi breg (Figure 1). For this location the depth to the bedrock (approx. 25 m) is known from nearby borehole and from geophysical measurements (Figure 2). In addition Standard Spectral Ratio (SSR) analysis of

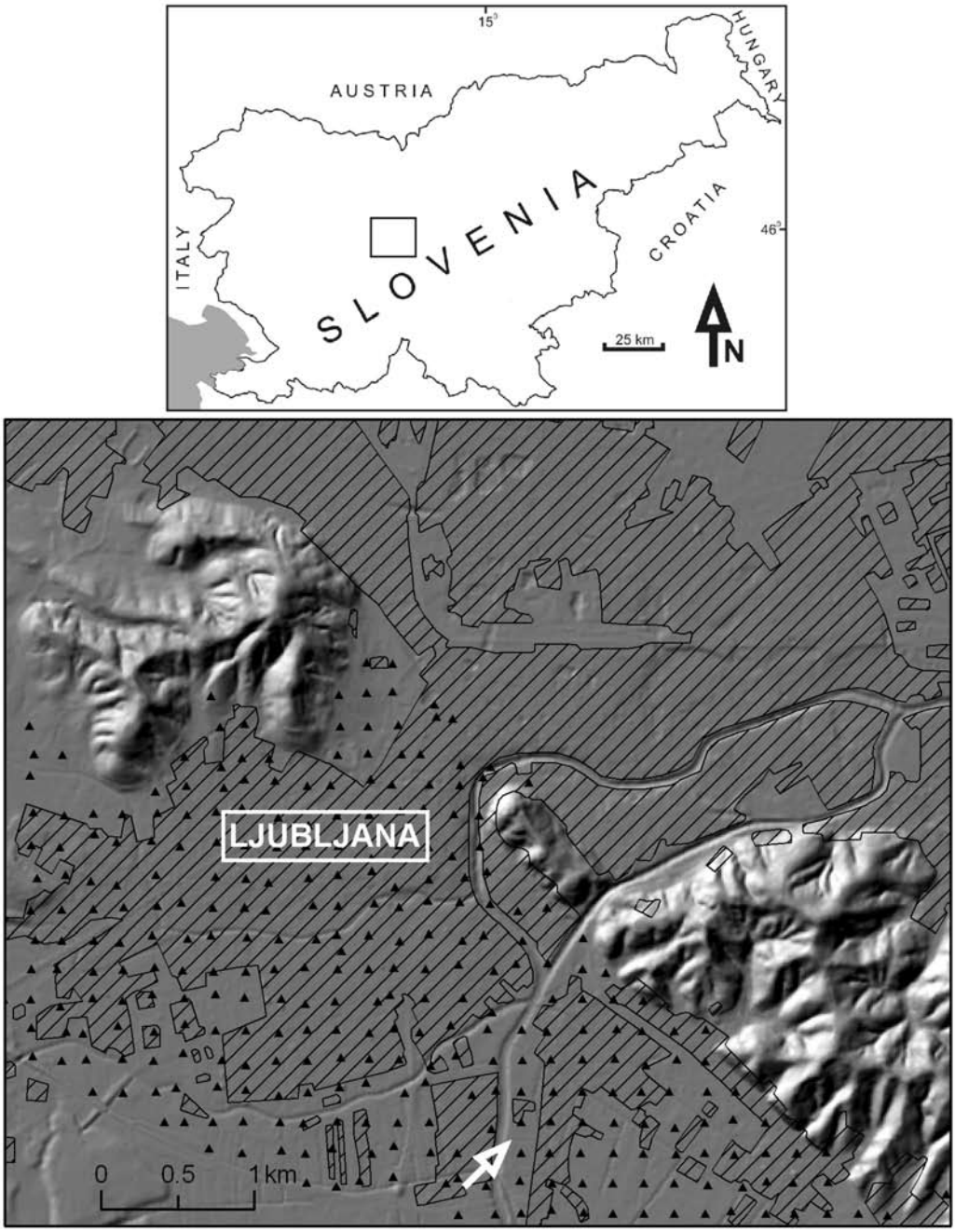

Figure 1. Location map of seismic measurements at Dolgi breg in the southern part of Ljubljana. Triangles indicate planed microtremor measurements.
Slika 1. Položaj seizmičnih meritev na Dolgem bregu v južnem delu Ljubljane. Trikotniki označujejo načrtovane meritve mikrotremorjev.

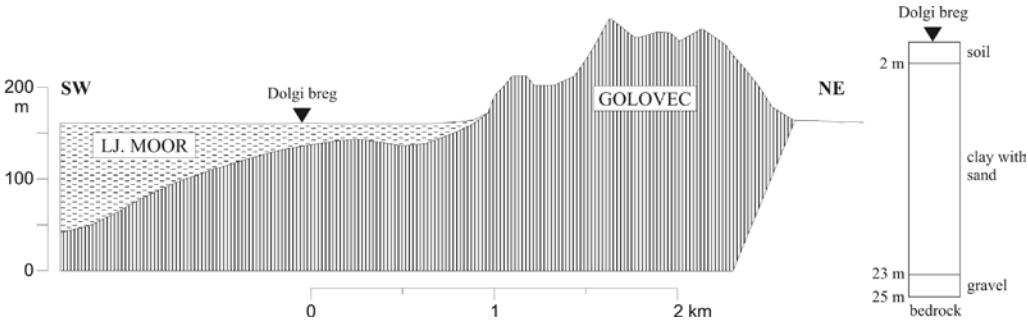

Figure 2. Profile across the Ljubljana Moor (Quaternary sediments) and Golovec hill (Permian and Carboniferous sandstones, conglomerates and shales) with the location of measurements at Dolgi breg
Slika 2. Profil prek Ljubljanskega Barja (kvartarni sedimenti) in Golovca (permski in karbonski peščenjaki, konglomerati in skrilavci) z lokacijo meritev na Dolgem bregu

earthquake data was available (Gosar & Živčić, 1998) which allowed comparison of site amplification.

Seismogeological setting

Ljubljana, the capital of Slovenia is situated in a young sedimentary basin filled with Quaternary deposits. According to the seismic hazard map of Slovenia for 475-years return period (Lapajne et al., 2001), a relatively high seismic hazard is characteristic of the area with design ground acceleration values of 0.20-0.25 *g* for a rock site. At the same time this is the most densely populated area of Slovenia with more than 300.000 inhabitants. The strongest earthquake in the history of the city occurred in 1895, when Ljubljana was hit by M=6.1 earthquake which caused extensive damage of VIII-IX MCS maximum intensity.

Strong site effects were characteristic of the southern part of Ljubljana, which is built on very soft lacustrine and marsh deposits of the Ljubljana Moor. The topography of the basins bedrock is here very rugged and its depth ranges from 0 m to 200 m (Figure 2). It is composed of Permian and Carboniferous sandstones, conglomerates, shales and Triassic dolomites. The Quaternary sediments are very heterogeneous, composed of clay, gravel, sand, lacustine chalk and peat. The uppermost layers are very soft.

The existing microzonation of Ljubljana was prepared in 1970 (Lapajne, 1970) using the nowadays outdated methodology of Medvedev (1965) to be used with the old seismic hazard intensity map of Slovenia which is given in MSK scale. The quantitative parameters to calculate "intensity increments" were obtained from P-wave seismic refraction measurement, but according to the methodology of Medvedev, no S-wave velocity information was collected. After the preparation of a new seismic hazard map of Slovenia (Lapajne et al., 2001) which specifies design ground acceleration for rock or firm soil, a need

arose for a new microzonation prepared according to Eurocode 8 and specifying soil factors (EUROCODE 8, 2003). The first attempt of a new microzonation of Ljubljana to be used in disaster prevention only, and not for earthquake resistant design, was prepared exclusively from existing data (ZUPANČIČ et al., 2004). The majority of the southern part of Ljubljana was classified in this map as ground type S_1 and minor parts in the border shallower parts as ground type E.

The main weakness of used existing data is a lack of shear-wave velocity information, because only at three locations S-wave refraction seismic data were available to calculate soil factors for ground type S_1.

METHODOLOGY

Active MASW

The active MASW was introduced by PARK et al. (1999). It adopts the conventional seismic refraction mode of survey (Figure 3a) using an active seismic source (usually sledgehammer) and a linear receiver array, collecting data in a roll-along mode. It utilizes surface waves, mainly horizontal travelling fundamental-mode Rayleigh waves, directly from impact point to receivers. Rayleigh waves are characterized by elliptical and retrograde particle motion. Its amplitude decreases exponentially with depth (Figure 3b). Different types of waves are recorded with multichannel array including: direct and refracted arrivals, air waves, reflections, fundamental and higher modes of Rayleigh waves, backscattering of surface waves and ambient noise. Dispersion nature of different types of waves is imaged through a 2D wavefield transformation into dispersion image (XIA et al., 2004). Certain noise wavefields such as back- and side-scattered surface waves and several types of body waves are automatically filtered out during this transformation (PARK et al., 2007). From the dispersion image a dispersion curve of the fundamental mode of Rayleigh waves is picked, which is then inverted for a 1D Vs profile (XIA et al., 1999; ROTH & HOLINGER, 1999). Multiples of them recorded in a roll-along mode can be used to prepare a 2D Vs map.

Typical field configuration consists of 24-channels connected to engineering seismograph (Figure 3a). Low-frequency geophones (e. g. 4.5 Hz) are recommended. Although the highest sensitivity is obtained with conventional geophones equipped with spikes, a land streamer (Figure 4) is a very good alternative on a flat ground, because of significant convenience in field operation.

Maximum depth of investigation (*Zmax*) is usually in 20-30 m range. However, it can vary with different sites and different strength of active sources used. Length of the receiver spread (*xT*) is directly related to the longest wavelength (λmax) that can be analyzed and is connected to the maximum depth of the investigation. On the other hand, receiver spacing (*dx*) is related to the shortest wavelength (λmin) and therefore to the shallowest resolvable depth of investigation. The source offset (*x1*) controls the degree of the record contamination by the near-field effects (PARK et al., 2006).

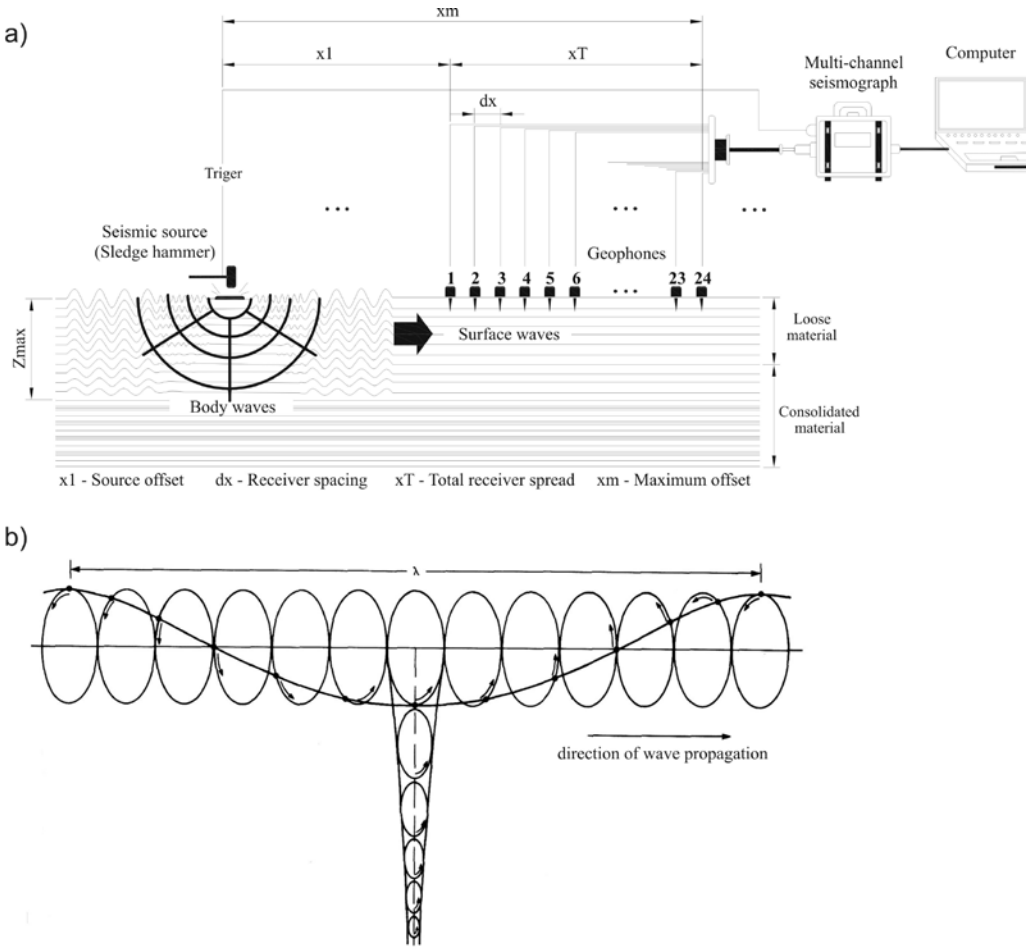

Figure 3. a) Schematic representation of active MASW measurements. b) Particle motion for Rayleigh waves showing amplitude decrease with depth (after SHERIFF & GELDART, 1995).
Slika 3. a) Shematski prikaz aktivnih MASW meritev. b) Gibanje delcev pri Rayleighjevem valovanju, ki kaže upadanje amplitude z globino (po SHERIFF & GELDART, 1995).

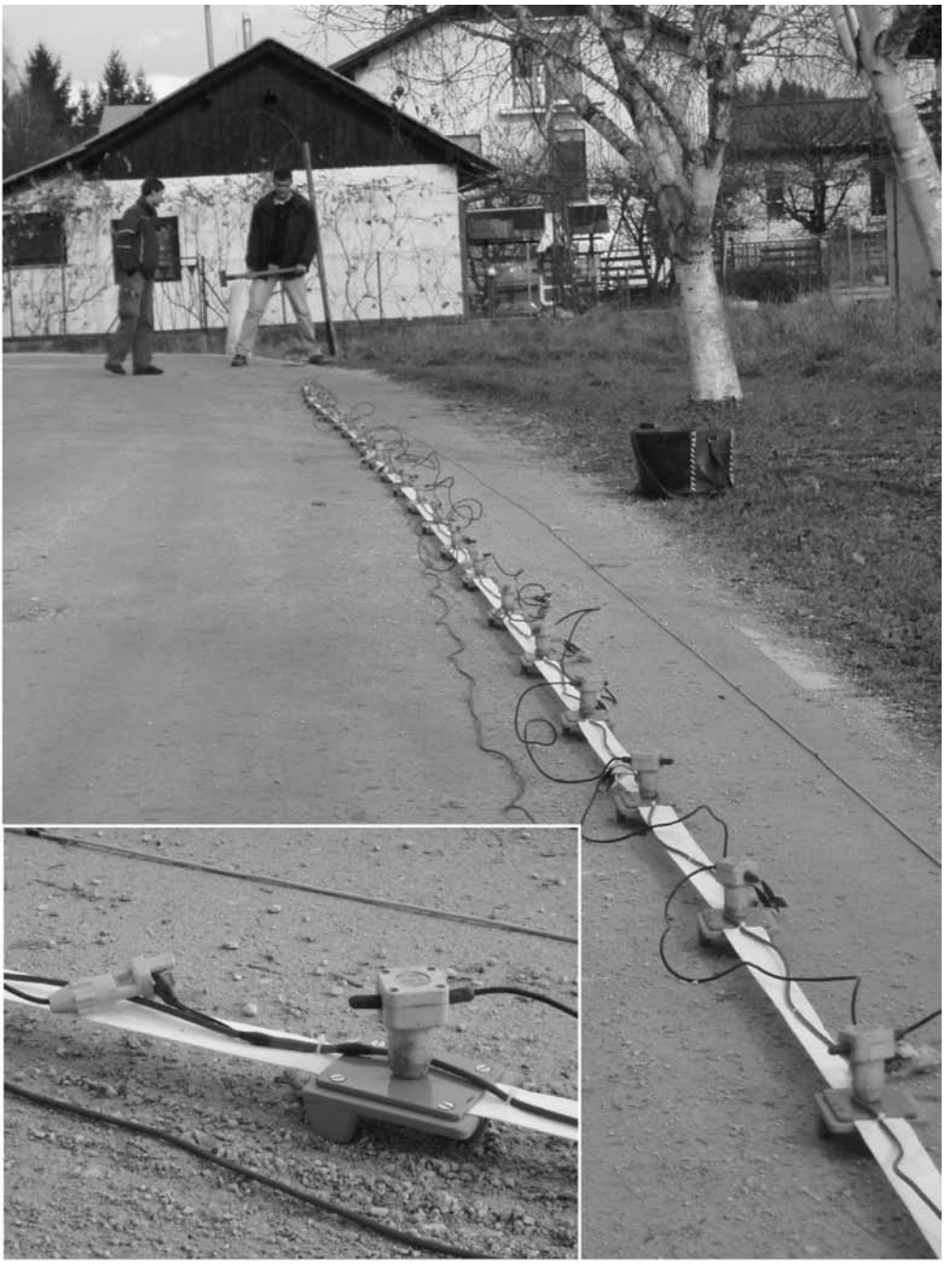

Figure 4. Land streamer with 24 vertical geophones and a sledgehammer as a seismic source; on a small insert a detail of geophone mount is shown
Slika 4. Land streamer z 24 navpičnimi geofoni in kovaško kladivo kot seizmični vir; majhna slika prikazuje izvedbo pritrditve geofona

When using sledgehammer or weight drop as a source a vertical stacking of multiple impacts can suppress ambient noise significantly.

Passive MASW

The main disadvantage of active MASW is the maximum depth of investigation which is usually 20-30 m. The amount of active-source energy needed to gain a few more Hz at the low-frequency end of the dispersion image, and thereby to increase investigation depth by several tens of meters, often rises several orders of magnitude, rendering efforts with an active source impractical and uneconomical (Park et al., 2007). On the other hand, passive surface waves generated by natural (tidal motion, sea waves, wind, rivers) or artificial (traffic, industry) activities are usually of a low frequency (1-30 Hz) with wavelengths ranging from few km (natural sources) to a few tens or hundreds of meters (artificial sources), providing a wide range of penetration depths.

This method was originally developed in Japan and called microtremor survey method (Okada, 2003) and adopted a smaller number (usually less than ten) of receivers. It is sometimes called also Microtremor Array Measurements or MAM (Hayashi et al., 2006). Louie (2001) first introduced linear refraction microtremor arrays (ReMi method). These methods were later developed as passive MASW method, which uses 24 or more geophones to fully exploit the advantages of multichannel recording and processing (Park et al., 2007). It therefore has an increased resolution in the analysis of both the modal nature and azimuthal properties of surface waves.

The passive MASW method employs a 2D geophone array such as a cross (Figure 8) or circular layout to record passive surface waves. Other array types as triangular or square are also common, but it is recommended that they have a symmetric shape. Any asymmetry can bias a result toward a specific direction of incoming surface waves that do not necessarily coincide with the actual direction of major surface-wave energy.

Array dimension is directly related to the longest wavelength (λmax) that can be analyzed and is connected to the maximum depth of the investigation. On the other hand, minimum receiver spacing is related to the shortest wavelength (λmin) and therefore to the shallowest resolvable depth of investigation. The typical depth of investigation for passive MASW is up to 100 m.

Data processing and analysis is similar as in active MASW and includes three steps: 1) generation of the dispersion image (phase velocity-frequency chart), 2) extraction of the dispersion curve from the image and 3) inversion of 1D shear-wave velocity profile from the dispersion curve (Park et al., 2006). Some techniques like ReMi use slowness instead of phase velocity.

It is often useful to combine dispersion images from active and passive sets for two reasons: to enlarge the usable bandwidth of dispersion (and therefore the depth range) and to better identify the modal nature of dispersion trends (Park et al., 2005).

Microtremor HVSR

The microtremor HVSR method is in the

last decade widely used for microzonation and site effects studies (e. g. GOSAR, 2007a, 2007b). However, the theoretical basis of HVSR method is still debated and different explanations have been given. "Body waves" explanation is based on S-wave resonance in soft sediments layer with minor or neglecting influence of surface waves. More widely accepted is the "surface waves" explanation that HVSR is related to the ellipticity of Rayleigh waves which is frequency dependent (BARD, 1999). HVSR exhibits therefore a sharp peak at the fundamental frequency of the sediments, if there is a high impedance contrast between the sediments and the underlying bedrock. Criticism of the HVSR method was often related to the fact that there is no common practice for data acquisition and processing. Attempts to provide standards were only recently been made (SESAME, 2004). It is widely accepted today that the frequency of the HVSR peak reflects the fundamental frequency of the sediments. Its amplitude depends mainly on the impedance contrast with the bedrock and cannot be used as a site amplification. However, a comparison with results of standard spectral ratio method has shown that the HVSR peak amplitude underestimates the actual site amplification (BARD, 1999; SESAME, 2004). HVSR also does not provide any estimate of the actual bandwidth over which the ground motion is amplified. The main advantages of HVSR method are therefore simple and low-cost measurements and direct estimates of the resonance frequency of sediments without knowing the geological and S-velocity structure of the underground. Any knowledge about the thickness or/and velocity of sediments and the comparison of HVSR results with other methods and with the observed earthquake damage can significantly improve the reliability of the results.

Microtremor HVSR method does not provide directly shear-wave velocity structure, but this can be derived by modelling of spectral ratio curve if necessary. It is usually based on the search for the model whose theoretical HVSR response best matches the observed HVSR by random perturbation of model parameters within preselected limits (HERAK, 2007).

DATA ACQUISITION AND ANALYSIS

A comparative test of three different methods was performed at Dolgi breg near Ljubljanica river on the Ljubljana Moor (Figures 1 and 2). This site was selected for several reasons: a) the depth to the bedrock (approx. 25 m) is known from nearby borehole and geophysical measurements, b) the thickness of soft sediments is inside the depth penetration of active MASW method (less than 30 m), c) strong acoustic impedance contrast between sediments and bedrock is known from previous microtremor measurements (GOSAR, 2007b) and d) at a nearby location earthquake data were recorded which allows Standard Spectral Ratio (SSR) analysis (GOSAR & ŽIVČIĆ, 1998) for comparison.

Data acquisition parameters for all three methods are summarized in Table 1. Active and passive MASW measurements were performed using 24 channel ABEM Terraloc Mk6 seismograph with 24 bit digitiser. Because active MASW and mi-

Table 1. Summary of data aquisition parameters
Tabela 1. Povzetek parametrov zajema podatkov

Survey type	Active MASW	Passive MASW	Microtremor HVSR
Source	8 kg sledgehammer	noise	noise
Seismograph	ABEM Terraloc Mk6	ABEM Terraloc Mk6	Tromino
Geophones	4.5 Hz (land streamer)	4.5 Hz (spike coupling)	three-component electrodynamic
Receiver array	24 channel linear	24 channel cross	
Array dimension (xT)	23 m	55 m	
Receiver spacing (dx)	1 m	5 m	
Source offset (x1)	5 m		
Receiver array move	5 m		measur. at 5 points
Sampling frequency	2000 Hz (0.5 ms)	500 Hz (2 ms)	128 Hz
Recording time	2 s	32 s	20 min
No. of records	20	20	5

crotremor HVSR methods are both sensitive to noise introduced by wind, were the measurements realized on a calm day without wind. Active and passive MASW data were processed and analysed using SurfSeis software (Park et al., 2006) and microtremor HVSR data using Grilla software (Micromed, 2006).

Active MASW

Active MASW measurements were performed along a walking path covered with compacted sand. The 4.5 Hz vertical geophones (24) were mounted on a "land streamer" (Figure 4) designed at Geoinženiring which allows fast movement of the receiver array between measuring points without planting the geophones equipped with spikes into the ground. Land streamer is composed of small sledges equipped with screws to mount geophones, linked with textile ribbon which allows pulling the whole array to a new position. The distance between geophones was 1 m, the source offset 5 m and the array move between subsequent records 5 m. A sledgehammer was used as a source and 10 hits vertically stacked at each point. This produced a clear surface waves signal over the total recording length of 2 s (Figure 5). Together 20 records were measured along a 100 m long profile.

Data were processed in the following way. After data conversion from SEG-2 to KGS format the field geometry was encoded into the header of seismic traces. Dispersion images were calculated separately

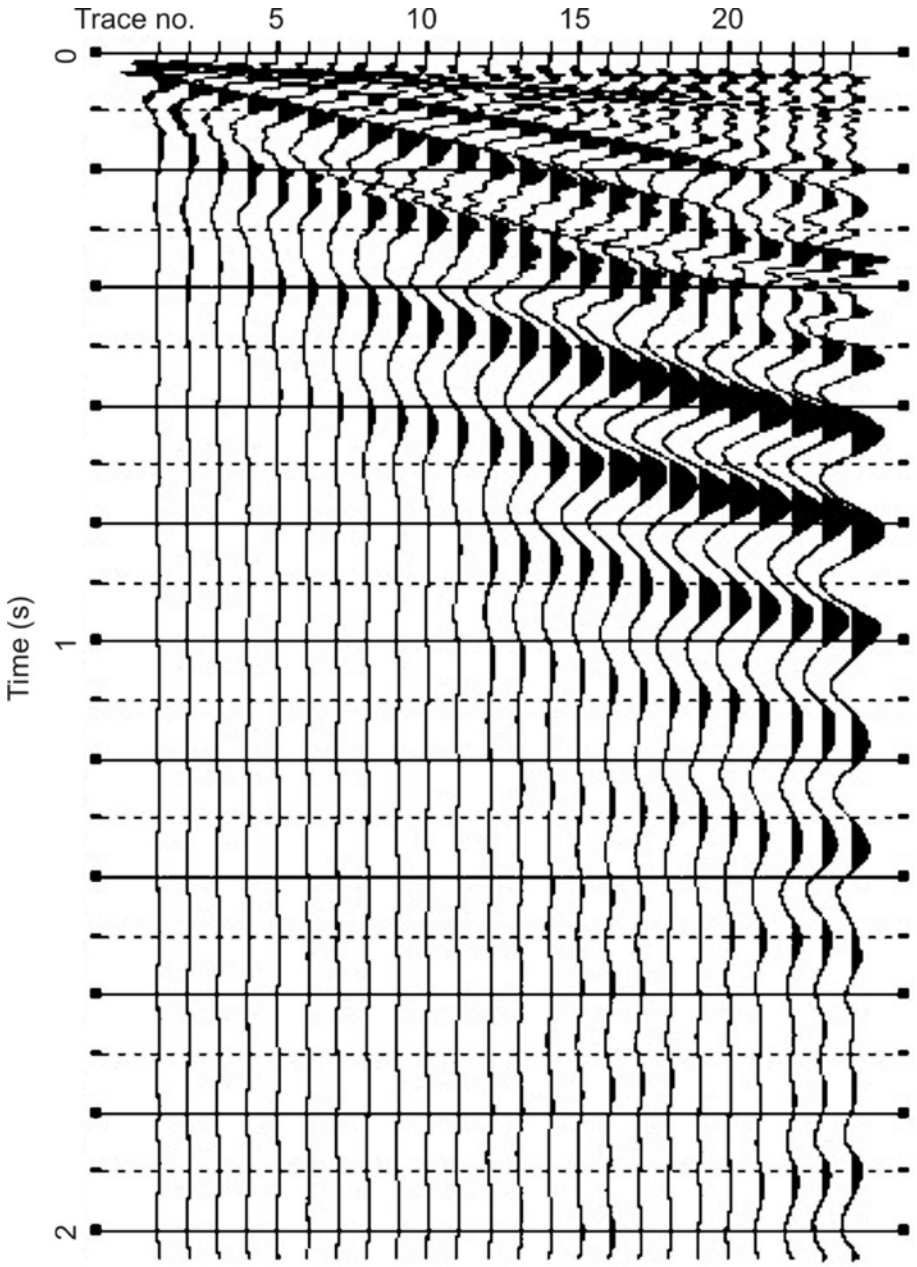

Figure 5. Seismogram example of active MASW measurements
Slika 5. Primer seizmograma aktivnih MASW meritev

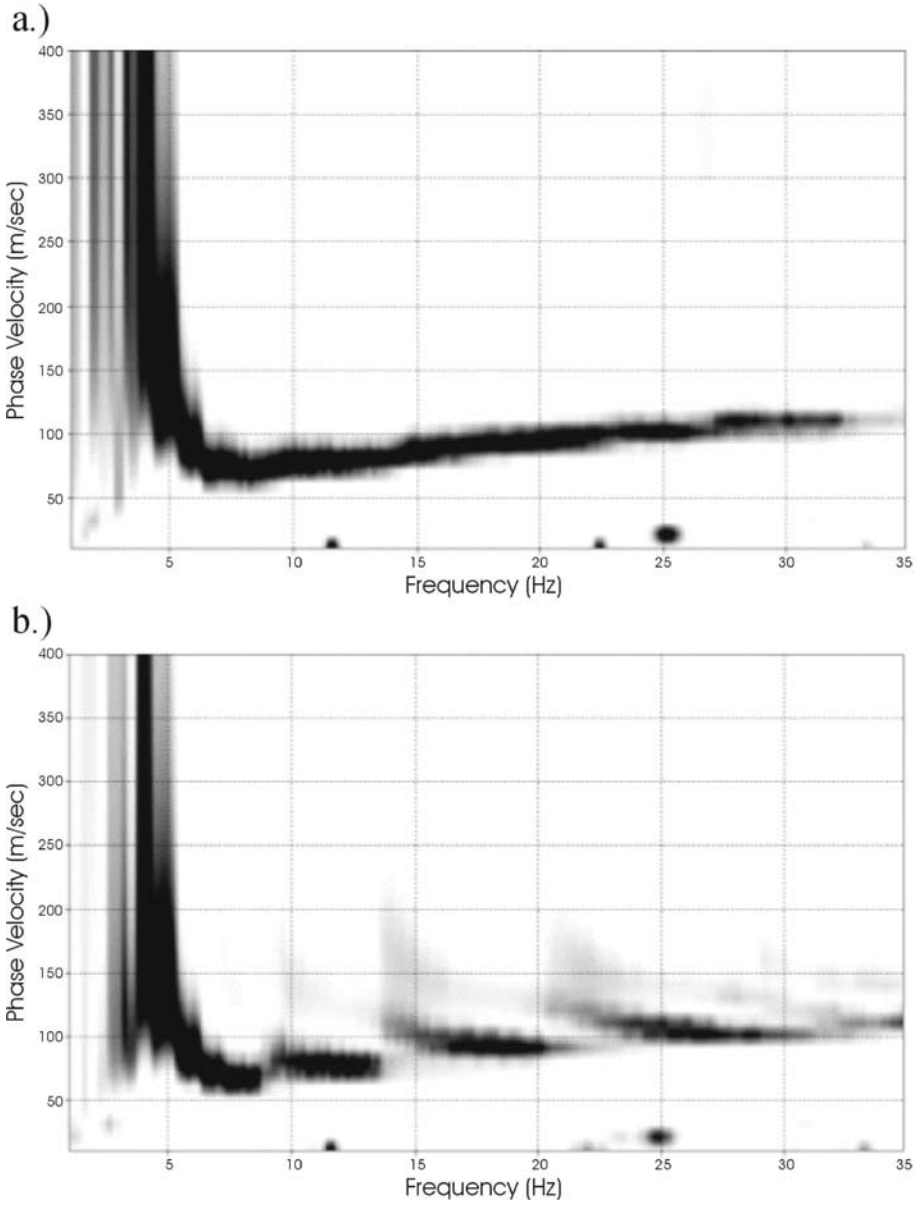

Figure 6. Dispersion images of two active MASW measurements: a) example with only fundamental mode of surface waves visible, b) example with higher modes of surface waves at frequencies ≥8 Hz

Slika 6. Disperzijski sliki dveh aktivnih MASW meritev: a) primer z vidno le osnovno obliko površinskih valov, b) primer z višjimi oblikami površinskih valov pri frekvencah ≥8 Hz.

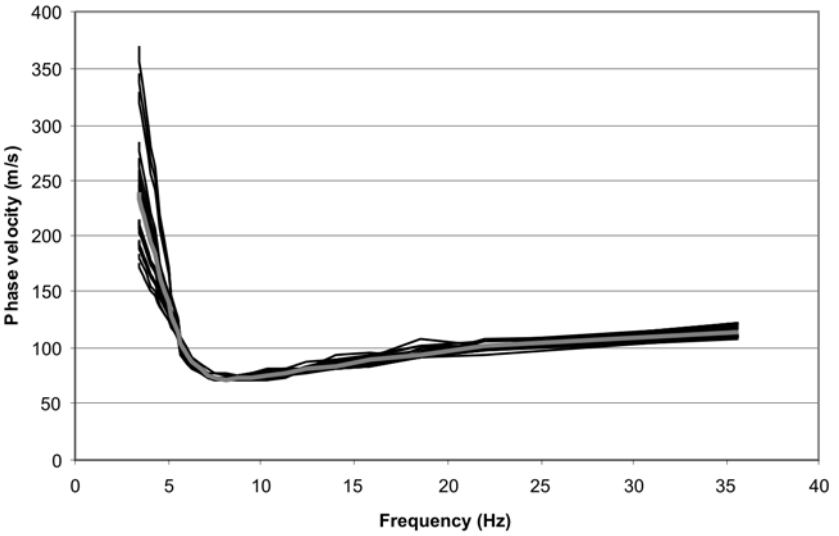

Figure 7. Dispersion curves of twenty active MASW measurements (thin black lines) with average curve (thick grey line)
Slika 7. Disperzijske krivulje dvajsetih aktivnih MASW meritev (tanke črne črte) s povprečno krivuljo (debelejša siva črta)

for all 20 records using frequency range 1-40 Hz and phase velocity range 10-400 m/s. The dominant frequency of surface waves was around 5 Hz. A very good signal to noise ratio was obtained for all records (Figure 6). The dispersion (Figure 6a) of the fundamental mode of surface waves is therefore very clear in the frequency range from 3 to 35 Hz with a steep decrease of phase velocity in the range 2-7 Hz down to minimum phase velocity of around 70 m/s, followed by a slight increasing of the phase velocity up to 32-35 Hz. In some of dispersion images (Figure 6b) some higher modes of surface waves are clearly visible above 8 Hz. After the definition of the bounds (lower and upper limits of phase velocities for the dispersion curve to be extracted) was the automatic picking algorithm successful in extraction of the dispersion curve due to good signal to noise ratio. The total number of points constituting the dispersion curve was set to 30 with equal-wavelength frequency interval used to make the frequency interval more dense at low and coarse at high frequencies. Dispersion curves for all 20 records are together with average curve shown in Figure 7. They are very similar, there is some discrepancy only in the initial part (low frequency) of the curves.

One-dimensional (1D) inversion of dispersion curves was performed using a gradient based iterative solution to the weighted equation (XIA et al., 1999) using Levenberg-Marquardt method. A variable model (the thickness of layers is increasing with depth) of ten layers was applied. The maximum depth defined by the size of the array and the lowest frequency of dispersion curve was around 30 m. The stopping criteria for inversion was maximum 12 iterations or

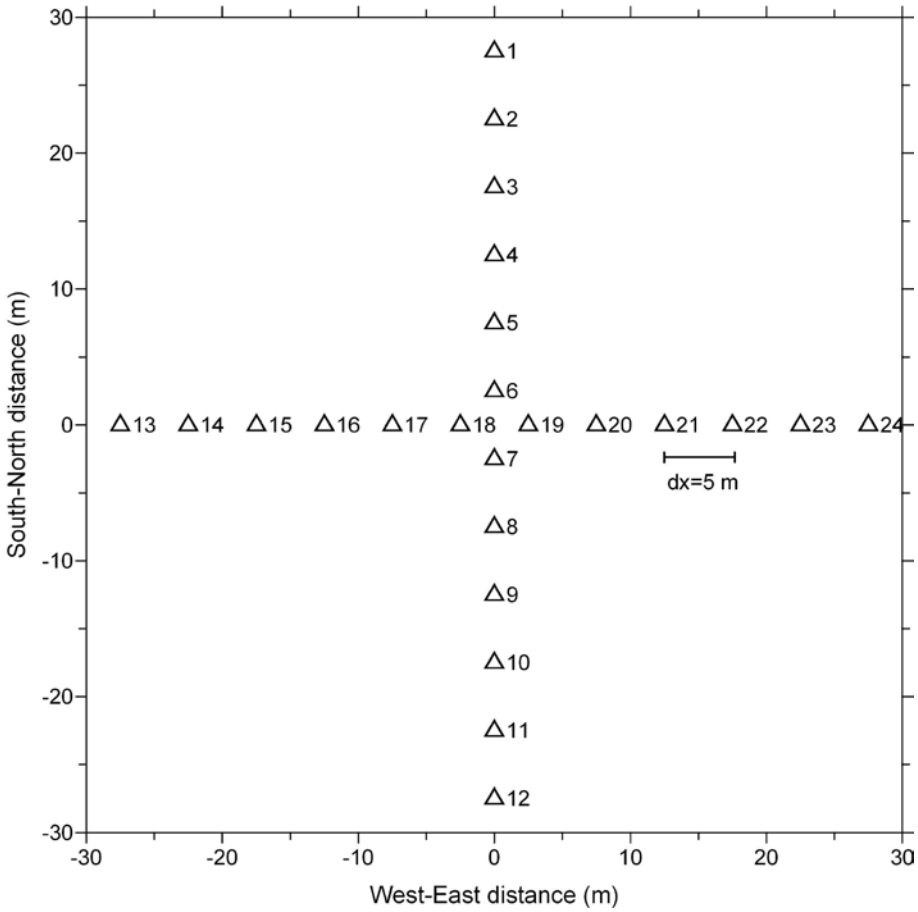

Figure 8. Cross geophone array used for passive MASW measurements
Slika 8. Križna geofonska razvrstitev uporabljena za pasivne MASW meritve

RMS error in phase velocity lower than 5. P-wave velocity was fixed to S-wave velocity using the Poisson ratio of 0.4. The average result of inversion for all 20 records is together with ± one standard deviation shown in Figure 14a. The variability of the results was quite small, because of the similarity of dispersion curves. It becomes greater only below the sediments/bedrock boundary which is clearly defined at around 25 m as a steep increase of S-velocity from around 200 m/s to 350 m/s.

Passive MASW

Passive MASW measurements were performed using symmetric cross-array (Figure 8) on a land covered with grass. The 4.5 Hz vertical geophones equipped with spikes were planted in equidistance with 5 m spacing in N-S and E-W direction. The array dimension in each direction was 55 m, which roughly determines the maximum depth of investigation. Together 20 records of 32 s length (Figure 9) were measured without moving the geophone array.

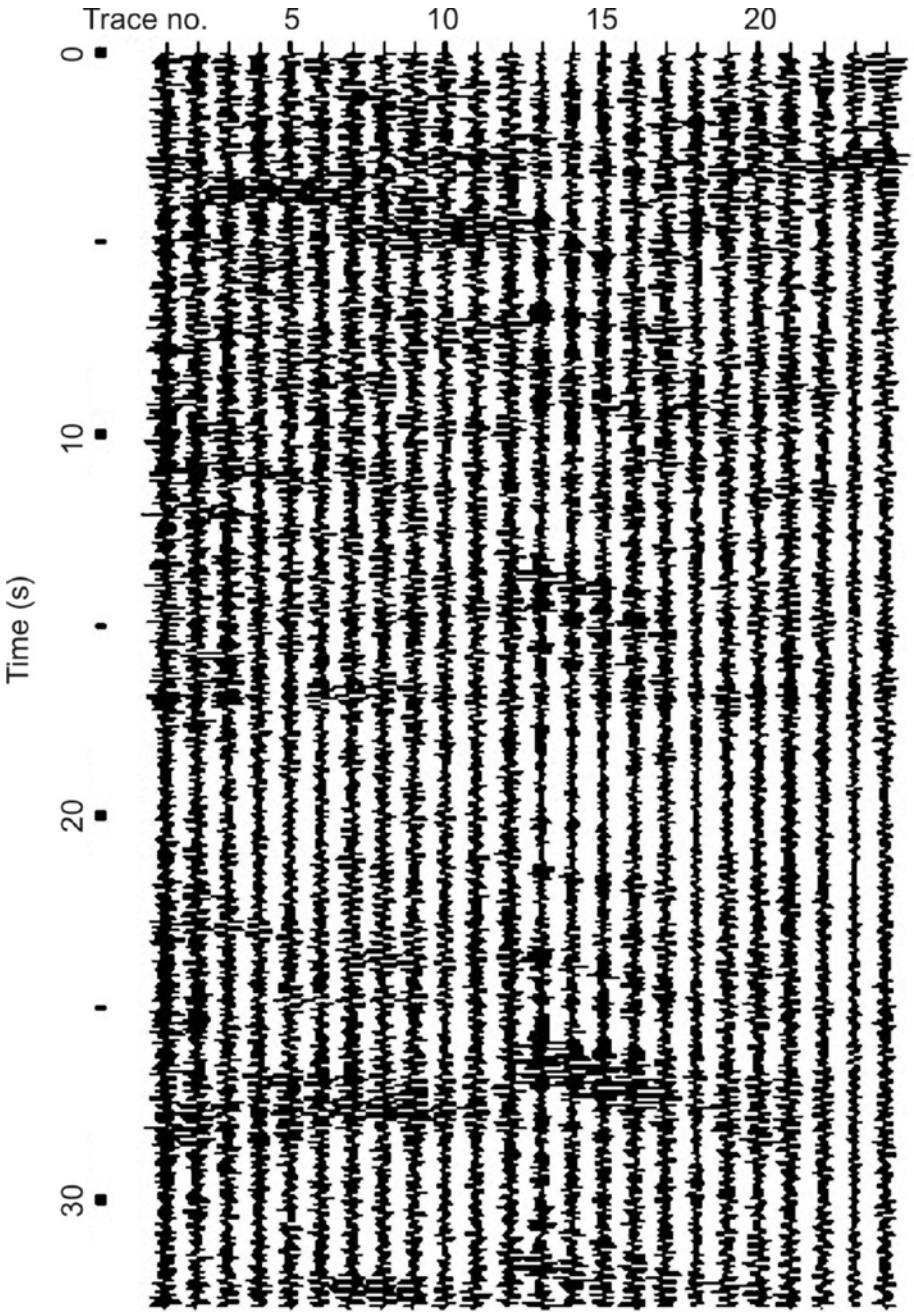

Figure 9. Seismogram example of passive MASW measurements
Slika 9. Primer seizmograma pasivnih MASW meritev

Data were processed in the following way. After data conversion from SEG-2 to KGS format the field geometry was encoded into the header of seismic traces. Dispersion image was calculated separately for all 20 records and the dispersion images than stacked together (Figure 10). The frequency range of calculation was 1-25 Hz and phase velocity range 10-300 m/s. A signal to noise ratio is obviously lower in passive than in active measurements. Nevertheless is the fundamental mode of surface waves quite clear in the frequency range 3-14 Hz, whereas higher modes prevail above 14 Hz. Dispersion curve was extracted in the frequency range 2-14 Hz using the same parameters as in active MASW. Both dispersion curves, average for active MASW and for passive MASW, are shown in the Figure 11. The shape of both curves is similar with a clear bend at around 7 Hz, but the curve of passive MASW is slightly shifted towards lower frequencies and lower phase velocities. In the frequency range 8-14 Hz is the passive MASW dispersion curve almost flat and shows a phase velocity of around 30 m/s.

For one-dimensional (1D) inversion of dispersion curve the same method was applied as in active MASW using a variable model (the thickness of layers is increasing with depth) of 13 layers to obtain a comparable layer thicknesses in upper 30 m as in active MASW. The maximum depth defined by the size of the array and the lowest frequency of dispersion curve was around 56 m. The stopping criteria for inversion was maximum 12 iterations or RMS error in phase velocity lower than 5. P-wave velocity was fixed to S-wave velocity using the Poisson ratio of 0.4. The result of the inversion is shown in Figure 14b.

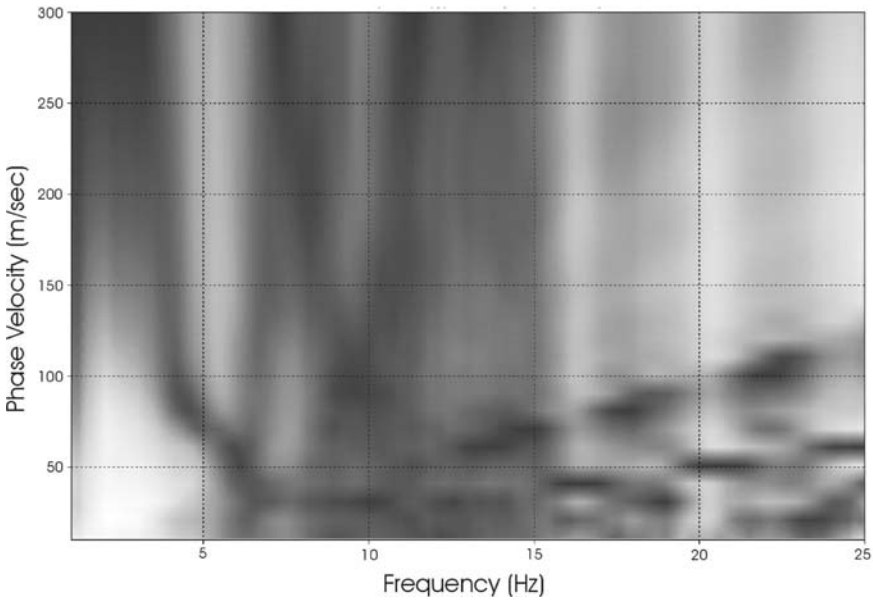

Figure 10. Dispersion image of passive MASW measurements
Slika 10. Disperzijska slika pasivnih MASW meritev

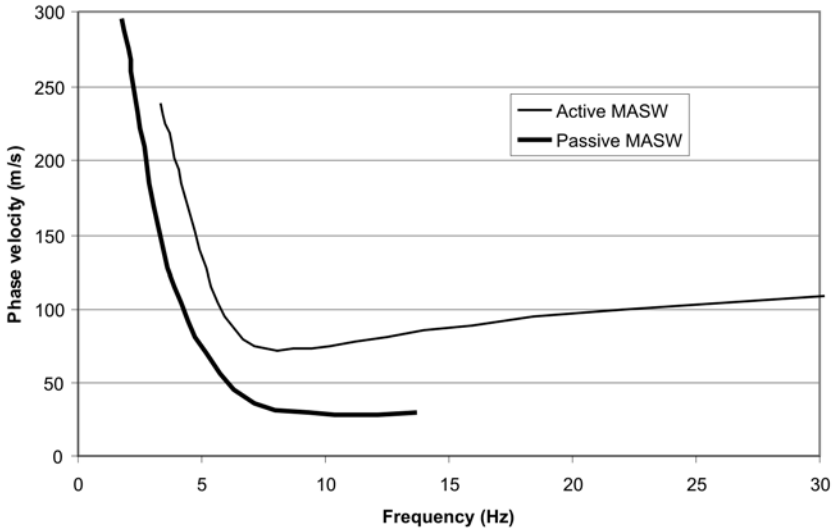

Figure 11. Dispersion curves of active (average) and passive MASW measurements
Slika 11. Disperzni krivulji aktivnih (povprečje) in pasivnih MASW meritev

Microtremor HVSR

Microtremor measurements were performed by using five portable seismographs Tromino (Micromed) composed of three orthogonal electrodynamic velocity sensors, 24 bit digitizer and recording unit with flash memory card. All parts are integrated in a common case to avoid electronic and mechanical noise that can be introduced by wiring between equipment parts. Good ground coupling on soft soils was obtained by using long spikes mounted at the base of the seismograph. Seismographs were deployed along the same 100 m long profile as used for active MASW measurements with 25 m spacing between instruments. The recording length was 20 minutes, which allows spectral analysis down to 0.5 Hz.

HVSR analysis was performed in the following way. Recorded time series were visually inspected to identify stronger transient noise. Each record was then split into 30 s long non-overlapping windows for which amplitude spectra in a range 0.5-64 Hz were computed using a triangular window with 5 % smoothing and corrected for sensor transfer function. HVSR was computed as the average of both horizontal component spectra divided by the vertical spectrum for each window. From the colour coded plot of HVSR functions for all 40 windows, the windows including strong transient noise were identified in order to be excluded from further computation. At the end, the average HVSR function with a 95 % confidence interval was computed.

All five HVSR curves are shown in Figure 12. They all show a sharp peak related to the fundamental frequency of sediments at 1.5 Hz (range 1.4-1.6 Hz). The amplitude of the peak which is less stable parameter

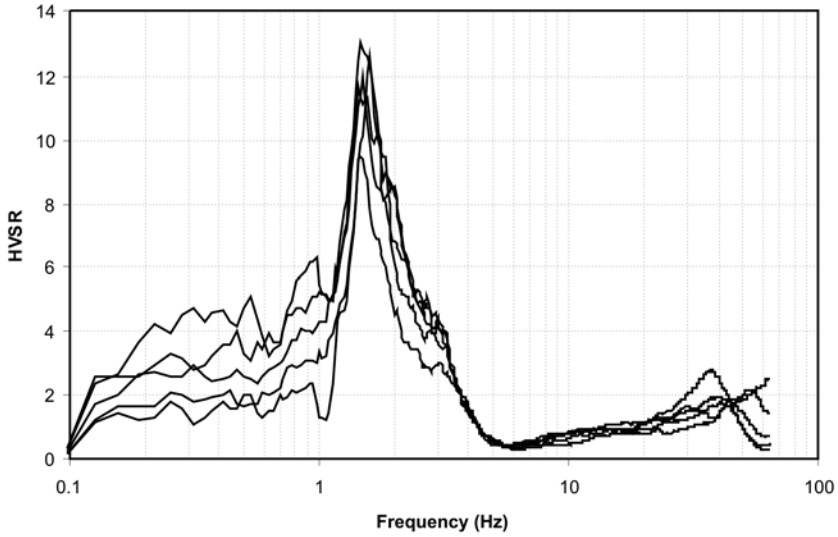

Figure 12. HVSR curves of five microtremor measurements
Slika 12. Krivulje HVSR petih meritev mikrotremorjev

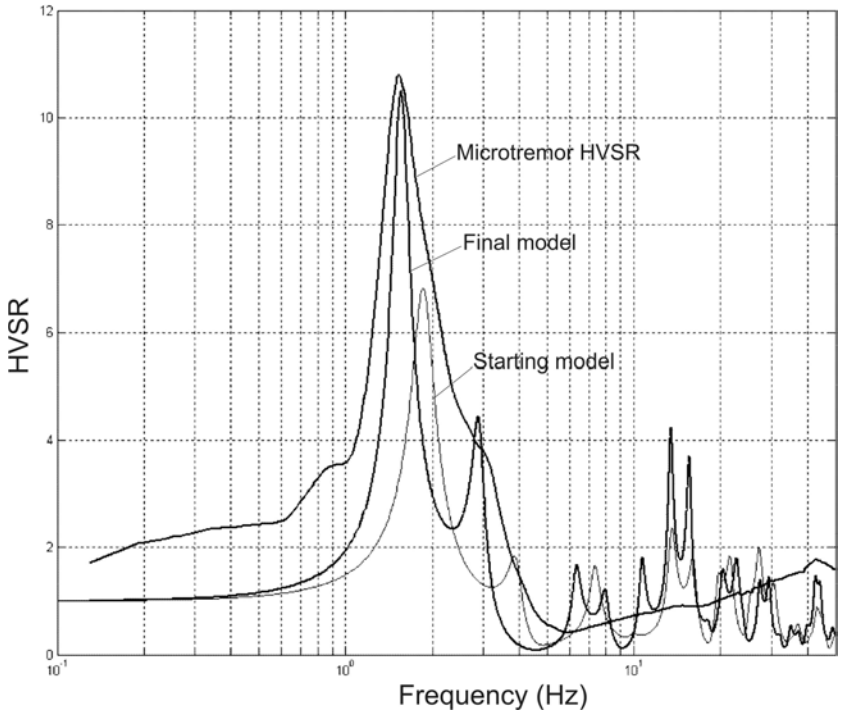

Figure 13. Results of modelling of average microtremor HVSR curve
Slika 13. Rezultat modeliranja povprečne krivulje HVSR iz meritev mikrotremorjev

of HVSR analysis is from 9.5 to 13 (average 10.5) what is an indication of a strong acoustic impedance contrast between sediments and bedrock. Average curve calculated from all five HVSR curves is shown in Figure 13.

The obtained fundamental frequency and HVSR amplitude is comparable to the results of Standard Spectral Ratio (SSR) analysis performed at nearby Rakova jelša, where seismograms of two regional earthquakes were recorded. Their amplitude spectra was divided by the spectra of the records of same earthquakes measured at a rock site on a Golovec hill to obtain a SSR. The dominant frequency of amplification obtained was around 2 Hz and the maximum amplification around 12 (Gosar & Živčić, 1998).

One-dimensional modelling of the average HVSR curve was performed using ModelHVSR program (Herak, 2007) which computes the theoretical P- and S-wave transfer function (amplification) of a layered, viscoelastic model for vertical incident P- and S-waves and use it for the calculation of a theoretical HVSR curve. Since only seismic impedances and travel times through layers have an influence on defining a transfer function, both depths and velocities can not be resolved at the same time. Therefore we used the same layer thicknesses as in active MASW inversion and keep them constant in a modelling procedure. For a starting model we also took velocities obtained by the inversion of active MASW measurement and then in a random model perturbation allowed a maximum 25 % variation of *Vp* and *Vs*. The number of random tries was 1000. The results are shown in Figure 13 as: measured average HVSR curve, curve which corresponds to the starting model and a curve which corresponds to the final model shown in Figure 14c. The fit between measured and calculated HVSR curve in terms of frequency and amplitude is very good, but there is a difference in the width of the peak.

Results

The one-dimensional shear-waves velocity profiles obtained with three different methods are shown in Figure 14. Despite determination of the depth of sediments/bedrock boundary is not the strong part of applied methods, is it clearly reflected at around 25 m in both profiles obtained by active MASW and microtremor HVSR as a sharp increase of S-velocity from around 200 m/s to 350-400 m/s. Passive MASW is less sensitive to the strong contrast of acoustic impedance and therefore is this boundary not so clear. However is the increase of S-velocity to around 300 m/s below the depth of 26 m already indicative for a bedrock.

Comparison of all three velocity profiles inside the sediments shows the following:

a) all the profiles start with thin (1-2 m thick) low-velocity layer followed by 1-1.5 m thick higher velocity layer (120-150 m/s); since the passive MASW was recorded on a grass is the soft surface layer there thicker in comparison to active MASW measurements recorded on a path built of compacted sand,

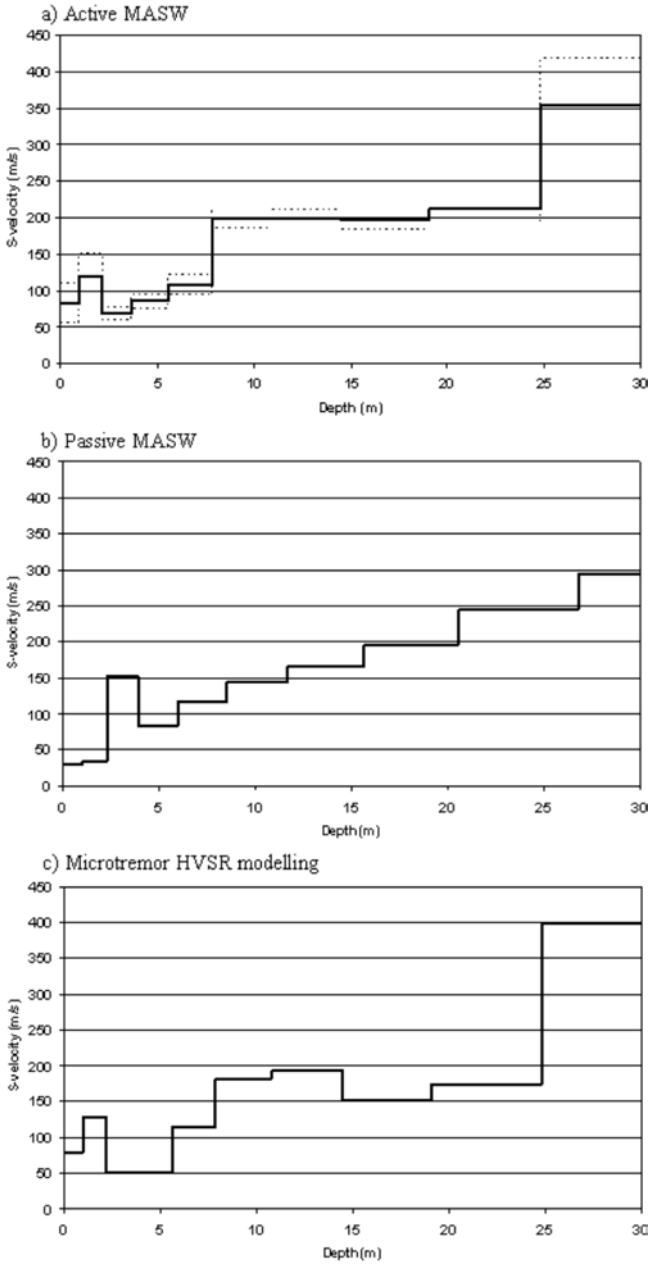

Figure 14. Shear-wave velocity profiles from a) active MASW (with ± one standard deviation), b) passive MASW and c) microtremor HVSR modelling
Slika 14. Profili hitrosti strižnih valov za a) aktivni MASW (z ± enim standardnim odklonom), b) pasivni MASW in c) modeliranje krivulje HVSR iz mikrotremorjev

b) in the depth range 2-7.5 m there is a low velocity layer (50-120 m/s),
c) in the depth range 7.5-25 m is the velocity according to active MASW and microtremor HVSR quite stable (150-210 m/s), while according to passive MASW there is a gradual increase of velocity from 150 to 250 m/s.

The S-velocities from dispersion of surface waves for the upper five meters are comparable to the velocities from shallow seismic refraction measurements performed at geologically similar location at Park Svoboda, also in the southern part of Ljubljana, where the velocities between 95 and 180 m/s were measured in the first five meters (ŽIVANOVIĆ & STOPAR, 1995).

The parameter widely applied in seismic microzonation, also the main parameter for ground type classification in Eurocode 8 standard (EUROCODE 8, 2003), is average shear-wave velocity in upper 30 m ($V_{S,30}$). It is computed according to the following expression

$$V_{S,30} = \frac{30}{\sum_{i=1,N} \frac{h_i}{V_i}}$$

where h_i and V_i denote the thickness (in m) and shear-wave velocity (in m/s) in the *i*-th formation of layer, in a total of *N*, existing in the top 30 metres.

Since the shear-wave velocity in the bedrock can not be well defined with applied methods we computed equivalent average velocity for the total thickness of sediments (around 25 m) and obtained the following values:

- active MASW – 145 m/s,
- passive MASW – 120 m/s,
- microtremor HVSR – 120 m/s.

Considering only this parameter to define the ground type in Eurocode 8, can be the investigated site classified as ground type D (Vs<180 m/s). But if we consider also a description of the stratigraphic profile, it is more likely ground type S_1 (Vs<100 m/s) described as: deposits consisting - or containing a layer at least 10 m thick – of soft clay/silts with high plasticity index and high water content.

CONCLUSIONS

Performed investigations with three different methods have shown that they are all effective in the determination of a shallow shear-waves velocity profile, but there are also some important differences between them. Obtained one-dimensional velocity profiles are similar to acceptable extent. The average shear-wave velocity in the 25 m thick layer of sediments is between 120 m/s and 145 m/s. The value obtained by active MASW (145 m/s) is 20 % greater than the values obtained by passive MASW and microtremor HVSR modelling (120 m/s). We found no explanation for this, but the difference is not too big to have a considerable influence on the determination of the ground type in seismic microzonation. The ground at investigated site can be therefore according to Eurocode 8 classified as type D or more likely S_1, if we consider also a description of the stratigraphic profile.

Comparison of active and passive MASW has shown that if the depth of investigation does not exceed 30 m much more clear dis-

persion image of surface waves is obtained with active method and is therefore preferable. A possible solution to increase the usable frequency range of dispersion would be to combine dispersion images obtained from active and passive measurements at the same location with different geophone arrays (Park et al., 2005) or using even the same linear array along a road where the traffic represents strong enough source of surface waves (Park et al., 2006). In the later case a long record is used triggered by a single hit of a sledgehammer. Initial part of the record is then processed as active and the remaining part as passive MASW.

Land streamer array of geophones was tested for the first time and proved very efficient for active MASW measurements along a two-dimensional profile. The only condition is that the surface of the ground is flat enough to assure near-vertical position of geophones. In a case of expected lateral variations of velocity, two-dimensional measurements have additional advantages with respect to passive measurements.

Microtremor HVSR method yield directly the fundamental frequency of the sediments overlying the bedrock which itself is a very valuable parameter of any microzonation, because it provides an estimate of the danger of soil-structure resonance. S-velocity profile can be derived by modelling of HVSR curve only if a reliable constraint on the thickness of the sediments can be done. If this is a case, as shown in our test, also microtremor data can provide a good estimate of one-dimensional S-velocity profile. Moreover, applicability of microtremor HVSR method highly depends on a strength of the impedance contrast between sediments and bedrock. On the contrary, MASW methods provide velocity profiles also for sites with gradual increase of velocity with depth.

Povzetek

Primerjalni test aktivne in pasivne večkanalne analize površinskih valov (MASW) ter metode mikrotremorjev (HVSR)

Hitrost strižnih seizmičnih valov v površinskih plasteh je pomembna za seizmološke analize nihanja tal ob potresu in v geotehniki, vendar pa jo je z uveljavljenimi geofizikalnimi metodami dokaj težko in drago določiti. V zadnjem desetletju pa so razvili nove metode večkanalne analize površinskih valov (MASW) in spektralnih razmerij mikrotremorjev (HVSR). MASW metoda temelji na disperziji površinskih (predvsem Rayleighjevih) valov, ki imajo precej nižje frekvence (1-30 Hz) kot prostorski seizmični valovi. Pri aktivnem MASW generiramo seizmične valove z udarci kladiva, pri pasivnem MASW in pri metodi mikrotremorjev pa uporabljamo seizmični nemir naravnega in umetnega izvora, ki je stalno prisoten v okolju.

V južnem delu Ljubljane, za katerega so značilni mehki sedimenti in izraziti lokalni seizmološki vplivi na potresne valove, smo izvedli test aktivne in pasivne MASW metode ter metode mikrotremorjev. Testno območje se nahaja na Dolgem bregu ob Ljubljanici, kjer je debelina kvartarnih sedimentov okoli 25 m. Pri aktivnem MASW smo prvič uporabili geofone pritrjene na posebnih nosilcih povezanih s

trakom (»land streamer«), ki omogoča hitro premikanje linearne razvrstitve 24-ih geofonov v medsebojni razdalji 1 m. Pri pasivnem MASW smo uporabili križno razvrstitev 2 x 12 geofonov v medsebojni razdalji 5 m. Meritve mikrotremorjev pa smo izvedli s posebnimi trikomponentnimi seizmografi. Pokazalo se je, da je aktivna MASW metoda najbolj uporabna na območjih, kjer ciljna globina ne presega 30 m, pasivna MASW metoda pa tudi pri večjih globinah. Prednost metode mikrotremorjev (HVSR) je, da daje neposredno oceno osnovne resonančne frekvence sedimentov. Pri slednji smo hitrostni profil določili z eno-dimenzionalnim modeliranjem spektralnega razmerja obeh vodoravnih glede na navpično komponento zapisa.

V 25 m debeli plasti kvartarnih sedimentov v katerih prevladujeta glina in pesek smo ugotovili hitrosti strižnih valov v razponu 50-200 m/s, v podlagi iz paleozojskega peščenjaka, konglomerata in skrilavca pa 350-400 m/s. Pod 1-2 m debelo površinsko nizkohitrostno plastjo je 1-1,5 m debela višjehitrostna plast (120-150 m/s). V globini 2-7,5 m sledi nižjehitrostna plast (50-120 m/s). Med 7,5 m in 25 m je hitrost po aktivnem MASW in mikrotremorjih dokaj stalna (150-210 m/s), po podatkih pasivnega MASW pa postopoma narašča od 150 do 250 m/s. Ujemanje hitrostnih profilov določenih z različnimi metodami je bilo zadovoljivo. Povprečna hitrost sedimentov v vrhnjih 30 m ($V_{S,30}$), ki se po standardu Eurocode 8 uporablja za klasifikacijo tal v potresni mikrorajonizaciji, je med 120 in 145 m/s. To bi uvrstilo obravnavana tla v vrsto D (Vs<180 m/s). Če pa upoštevamo še dodaten opis stratigrafskega profila, pa je bolj ustrezna uvrstitev v S_1 (Vs<100 m/s) saj profil vsebuje debelejšo plast zelo mehkih glinenih sedimentov z visoko vsebnostjo vode.

Acknowledgments

The authors are indebted to Ivan Majhen for the construction of a land streamer and to Sandi Kmetič for his help in field measurements.

References

Bard, P.Y. (1999): Microtremor measurements: a tool for site effect estimation? *The effects of surface geology on seismic motion*. Editors: (Irikura, K., Kudo, K., Okada, H. and Sasatami, T.), Balkema, pp. 1251-1279.

Hayashi, K., Inazaki, T., Suzuki, H. (2006): Buried incised-channels delineation using microtremor array measurements at Soka and Misato Cities in Saitama Prefecture. *Bull. Geol. Surv. Japan*.; Vol. 57/9-10, pp. 309-325.

Gosar, A., Živčić, M. (1998): Ojačanje nihanja tal zaradi lokalne geološke zgradbe na južnem obrobju Ljubljane (Rakova jelša). *Potresi v letu 1997*.; pp. 59-66.

Gosar, A. (2007a): Microtremor HVSR study for assessing site effects in the Bovec basin (NW Slovenia) related to 1998 Mw5.6 and 2004 Mw5.2 earthquakes. *Engineering geology*.; Vol. 91, pp. 178-193.

Gosar, A. (2007b): Raziskave vpliva lokalne geološke zgradbe na potresno nihanje tal in ranljivosti objektov z mikrotremorji. *Geologija*.; Vol. 50/1, pp. 65-76.

Herak, M. (2007): *ModelHVSR 3.3 user manual*. University of Zagreb, 6 pp. <http://nato.gfz.hr/Software.html>.

Eurocode 8 (2003): *Design of structures for earthquake resistance. Part 1: General rules, seismic actions and rules for buildings*. European Committe for Standardization.

Lapajne, J. (1970): Seizmična mikrorajonizacija Ljubljane. *Geofizikalne raziskave 1969-1970*. Geološki zavod Ljubljana, 16 pp. (unpublished report).

Lapajne, J., Šket Motnikar, B., Zupančič, P. (2001): *Karta potresne nevarnosti Slovenije – projektni pospešek tal*. Agencija RS za okolje.

Louie, L.N. (2001): Faster, Better: Shear-wave velocity to 100 meters depth from refraction microtremor arrays. *Bul. Seism. Soc. Am*.; Vol. 91, pp. 347-364.

Medvedev, S. V. (1965): *Inženjerska seizmologija*. Gradjevinska knjiga, 270 pp.

Micromed (2006): *Grilla 2.2, spectral and HVSR analysis - user manual*. Micromed, 48 pp.

Okada, H. (2003): *The microtremor survey method*. Society of Exploration Geophysicists, 135 pp.

Park, C.B., Miller, R.D., Xia, J. (1999): Multichannel analysis of surface waves (MASW). *Geophysics*.; Vol. 64, pp. 800-808.

Park, C.B., Miller, R.D., Ryden, N., Xia, J., Ivanov, J. (2005): Combined use of active and passive surface waves. *Journal of Engineering and Environmental Geophysics*.; Vol. 10/3, pp. 323-334.

Park, C.B., Ivanov, J., Brohammer, M. (2006): *SurfSeis 2.0 user manual*. Kansas Geological Survey, 38 pp.

Park, C.B., Miller, R.D., Ryden, N., Xia, J., Ivanov, J. (2007): Multichannel analysis of surface waves (MASW)-active and passive methods. *The Leading Edge*.; Vol. 26/1, pp. 60-64.

ROTH, M., HOLLIGER, K. (1999): Inversion of source-generated noise in high-resolution seismic data. *The Leading Edge*.; Vol. 18/12, pp. 1402-1406.

SESAME (2004): *Guidelines for the implementation of the H/V spectral ratio technique on ambient vibrations: measurements, processing and interpretation*.; 62 pp. <http://sesame-fp5.obs.ujf-grenoble.fr/Delivrables/Del-D23 HV_User_Guidelines.pdf>.

SHERIFF, R.E., GELDART, L.P. (1995): *Exploration seismology*. Cambridge University Press, 592 pp.

WIGHTMAN, W.E., JALINOOS, F., SIRLES, P., HANNA, K. (2002): *Multichannel Analysis of Surface Waves Method*. http://www.cflhd.gov/agm/engApplications/Pavements/414MultichannelAnalysisSurfWaves-Method.htm

XIA, J., MILLER, R.D., PARK, C.B. (1999): Estimation of near-surface shear-wave velocity by inversion of Rayleigh waves. *Geophysics*.; Vol. 64, pp. 691-700.

XIA, J., MILLER, R.D., PARK, C.B., IVANOV, J., TIAN, G., CHEN, C. (2004): Utilization of high-frequency Rayleigh waves in near-surface geophysics. *The Leading Edge*.; Vol. 23/8, pp. 753-759.

ZUPANČIČ, P., ŠKET-MOTNIKAR, B., GOSAR, A., PROSEN, T. (2004): Karta potresne mikrorajonizacije mestne občine Ljubljana. *Potresi v letu 2002*.; pp. 32-54.

ŽIVANOVIČ, M., STOPAR, R. (1995): *Geofizikalne raziskave lokacij monitoringa močnih potresov na območju mesta Ljubljane*. Geoinženiring, 14 pp. (unpublished report).

Application of seismic tomography in investigations of the motorway alignment in the Šentvid tunnel area

Uporaba seizmične tomografije pri raziskavah AC trase na območju predora Šentvid

Janez Rošer[1], Robert Stopar[2], Andrej Gosar[1,3]

[1]University of Ljubljana, Faculty of Natural Sciences and Engineering, Aškerčeva cesta 12, SI-1000 Ljubljana, Slovenia; E-mail: janez.roser@ntf.uni-lj.si
[2]Geoinženiring d.o.o., Dimičeva ulica 14, SI-1000 Ljubljana, Slovenia; E-mail: robert.stopar@geo-inz.si
[3]Environmental Agency of the Republic of Slovenia, Dunajska cesta 47, SI-1000 Ljubljana, Slovenia; E-mail: andrej.gosar@gov.si

Received: December 19, 2007 **Accepted:** January 12, 2008

Abstract: The motorway tunnel Šentvid construction area has a very demanding geotechnical structure. On the basis of previous investigations, it was not possible to exactly define the best locations of merging caverns with ramp tunnels. That is why initially an exploration gallery has been constructed, in which different geological, geomechanical and geophysical investigations have been carried out. The goal of geophysical investigations was to obtain seismic parameters to define geomechanical rock mass characteristics in the region of planned merging caverns. Final solution is the velocity field of longitudinal and transversal seismic waves in the investigated region. Dynamic elastic moduli distribution of rock mass was also computed from seismic parameters. Seismic velocity fields and the distribution of dynamic elastic moduli well define areas of more compact rock mass.

Izvleček: Območje AC predora Šentvid je v geotehničnem smislu zelo zahtevno. Ker na podlagi predhodno izvršenih preiskav ni bilo mogoče natančno določiti lokacij kavern dveh priključnih predorov, je bil najprej izdelan raziskovalni rov, v katerem so bile izvedene različne geološke, geomehanske in geofizikalne raziskave. Cilj geofizikalnih raziskav je bil s pomočjo seizmičnih parametrov določiti geomehanske lastnosti posameznih kamnin v območjih načrtovanih priključnih kavern. Končni rezultat je hitrostno polje longitudinalnega in transverzalnega seizmičnega valovanja preiskovanega območja ter iz njiju izračunani dinamični elastični moduli hribine. Seizmična tomografija je dobro opredelila območja kompaktnejše kamnine, kar odražajo tako hitrosti longitudinalnega in transverzalnega valovanja kot tudi dinamični elastični moduli.

Review paper

Key words: geophysics, seismic tomography, Šentvid tunnel, dynamic elastic moduli
Ključne besede: geofizika, seizmična tomografija, predor Šentvid, dinamični elastični moduli

Introduction

The Šentvid tunnel is part of the motorway bypass of Ljubljana, section Šentvid – Koseze, which connects Ljubljana with Gorenjska motorway part. There were several attempts to establish motorway bypass in the past years, but all the suggested solutions were postponed because of their pretentiousness. Due to the unbearable traffic situation the investigations for tunnel construction finally commenced in 1999.

The twin-tube tunnel system Šentvid is divided into four units (Figure 1): two lane tunnel, ramp tunnels, merging caverns and three lane tunnel. The length of all tubes is approximately 3000 m and excavation profiles vary from 81 m^2 in ramp tunnels to 300 m^2 in merging caverns (Žigon et al., 2004). Due to outstanding dimensions of planning caverns and variable geological conditions, additional investigations were required to exactly define locations of the merging caverns. To satisfy all the requests an exploration gallery has been constructed (Figure 1).

Additional geophysical investigations were performed in several stages. In October 2004 the surface seismic refraction profiling was performed as the starting point for further seismic investigation activities. After the construction of the exploration gallery had finished in 2005, the seismic investigations between the surface, the exploration gallery and the boreholes were performed. The scope of the survey was characterization of the geotechnical conditions in the motorway tunnel Šentvid

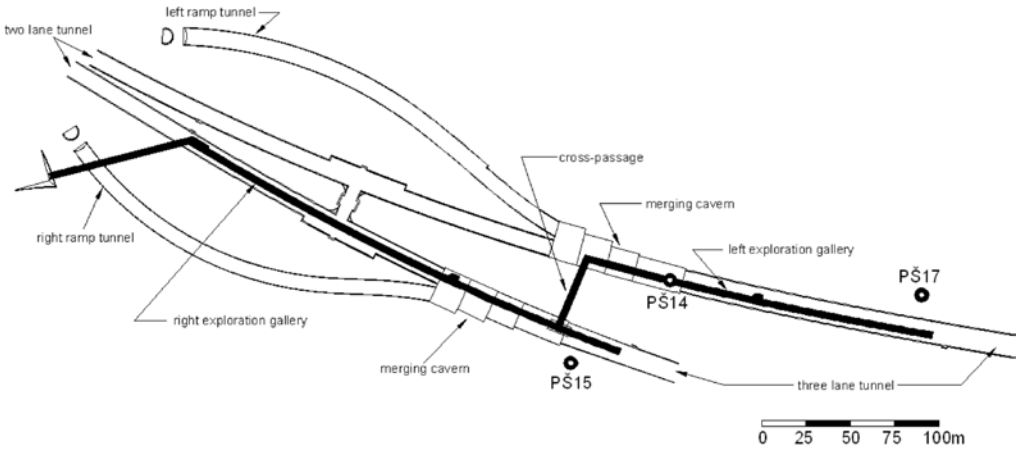

Figure 1. Alignment of the Šentvid tunnel and the exploration gallery
Slika 1. Trasa predora Šentvid in raziskovalnega rova

Table 1. Geomechanical parameters of Permian and Carboniferous layers
Tabela 1. Geomehanski parametri permokarbonskih plasti

Geomechanical parameters	*Layers of dark grey siltstone and clayed shalestone*	*Layers of light grey sandstone and dark grey micaceous siltstone*	*Tectonic clay and breccia*
RMR	class IV (35 points)	class III (42 points)	class V (< 20 points)
σ_c [*MP*a]	1.00	2.50 – 3.30	0.04 – 0.06
φ [°]	25 – 28	27 – 30	18 – 22
φ_{rez} [°]	22 – 25	24 – 27	15 – 19
c [*MP*a]	0.40	0.36 – 0.46	0.00
v [/]	0.26 – 0.27	0.25 – 0.26	0.29 – 0.31
E [*GP*a]	1.70 – 3.10	2.10 – 4.10	0.11

construction area. The goal of geophysical investigation activities was to use seismic parameters to define geomechanical rock mass characteristics in the region of planned merging caverns.

Geological conditions

The Šentvid tunnel alignment passes through Permian and Carboniferous sediments that include sandstone, siltstone and claystone, which are disintegrated from surface to about 30 m deep. In the tunnel area siltstone is prevalent. The region has undergone intense tectonic deformations, presumably during several deformation phases (Čadež et al., 2004). Tectonised zones consist of shalestone and highly tectonised clay.

Rock masses were characterized in terms of RMR (Rock Mass Rating). The following parameters for each different rock type were determined in laboratory: σ_c – uniaxial compressive strength of rock mass, E – modulus of elasticity, φ – angle of internal friction, φ_{rez} – residual friction angle, c – cohesion and v – Poisson's ratio (Fifer Bizjak et al., 2003). Geomechanical parameters are summarized in Table 1.

The lithological layers are generally sheared parallel to their schistosity. Fault gouge and fault breccias of all lithologies occur in association with faults and shear planes. The lateral continuity of the lithological layers is inconsistent due to frequent displacements along intersecting faults (Čadež et al., 2004).

Hydrogeological conditions in tunnel area are suitable and are classified as poorly permeable and small groundwater extractions (from 0.1 to 1.0 l/s per m of tunnel tube) are expected (Brenčič, 2000). In the tunnel area two hydrogeological units were defined: weathered and disintegrated rock in portal area and the interior rock mass. Both units differ in permeability and porosity.

FIELD INVESTIGATIONS

First phase investigations for Šentvid tunnel commenced in 1991. Later additional investigations began in 1999. In December 1999 the tunnel region was geologically and hydrogeologically mapped. In this phase five structural and nine geomechanical boreholes were drilled, which were all geologically monitored and cored. In boreholes seismic down-hole surveys, presiometric tests, SPT and slug tests were performed. Laboratory investigations of the mineralogical and geomechanical properties of characteristic rock samples were also done.

In October 2004 surface seismic refraction investigations started. On the basis of those results further geophysical investigations were planned. When the construction of the exploration gallery was finished at the beginning of 2005, geophysical measurements in the exploration gallery and between gallery, surface and boreholes were performed. Seismic investigations included surface refraction measurements along the tunnel alignment (10 linear arrays), tomography between the exploration gallery and the surface (5 linear arrays), tomography between the exploration gallery and the boreholes (2 linear arrays) and tomography between the right and left gallery (2 linear arrays).

SEISMIC TOMOGRAPHY

The mathematical basis for tomographic imaging was laid down by Johann Radon already in 1917. He showed that a form of an object could be obtained from its cross-sectional images. Due to computing power progress the tomographic method became very useful in astronomy, followed by great success in medicine and also in geophysics. The main restrain in geophysical tomography is that geometric factors are less determinable and that the investigation plain is mostly accessible only from two directions. Seismic tomography is used to image the interior of the Earth, for determining the elastic properties of the rock masses involved in geotechnical engineering and is particularly suitable for detecting and characterizing local structures, such as faults, fractures, cavities and other discontinuities.

For processing of tomographic data, the investigated area is divided into square grid, where cell dimensions depend on the seismic ray coverage (Figure 2). It is essential for a successful solution that every cell is intersected by multiple rays from different angles.

Travel time of the seismic ray between the source and the receiver is equal to the sum of travel times through every single cell. Consider that the source of seismic wave motion is in point *M (x, y)* and the receiver (geophone) is in point *N (x, y)*. Travel time of the signal is then written as (Figure 2):

$$t_{M,N} = \int_{L_{M,N}} \frac{1}{v(x,y)} ds$$

After discretisation:

$$T_{M,N} = \sum_i \sum_j \frac{1}{v_{i,j}} \cdot \Delta S_{i,j\,M,N}$$

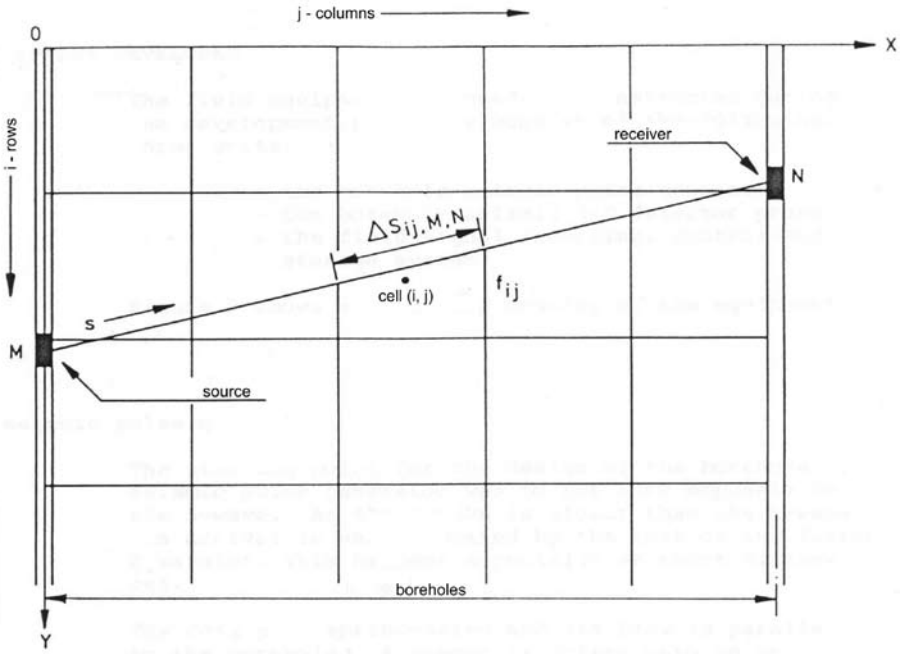

Figure 2. Velocity field in matrix form (Cosma et al., 1984)
Slika 2. Slika hitrostnega polja v matrični obliki (Cosma et al., 1984)

Tomographic inversion

By the tomographic inversion, the information obtained from field measurements is transformed to a model of the structure of the rock. Tomographic data sets often consist of many measurements. The result is that matrices can be large, sparse, and difficult to invert directly. A variety of computational methods have been developed to implement matrix inversions, such as generalized simulated annealing algorithm (SeisOpt, 2002) and simultaneous iterative reconstruction technique – SIRT (Jackson and Tweeton, 1994), which are both iterative solvers. These two methods were used to reconstruct the seismic velocity models in Šentvid tunnel tomography.

The generalized simulated annealing algorithm performs repeated forward modelling, where new models are conditionally accepted or rejected based on a probability criterion. This criterion allows the algorithm to escape from non-unique, local, travel-time minima to achieve a unique, globally optimized model of subsurface velocity structure (SeisOpt, 2002).

Another processing was performed by using the inversion algorithm based on the SIRT method. It updates an initial model through repeated cycles of forward travel time computation. Then the curved-ray inversion was performed. In the curved-ray tomography inversions the starting velocity model plays a crucial role, because the routine can be trapped in local minima misidentifying the global minimum solution (Dines and Lytle, 1979).

Seismic data acquisition

First we performed seismic refraction survey on the surface. Above the right exploration gallery there were 6 geophone arrays and above the left exploration gallery 4 arrays. Every array is composed of 24 geophones which record the seismic waves. Distance between receivers (4.5 Hz geophones) was 4 m. Three 24-channel digital seismographs with sample rate of 0.1 ms were used. The main purpose of refraction survey was to establish a reasonable starting model for tomography between the exploration gallery and the surface. The propagation of longitudinal (P) waves as well as transversal (S) waves was measured with all surface arrays. Because of a different kind of seismic noise (particularly traffic) and large source-receiver distances, a more powerful source was needed. Therefore explosive was used as a seismic source. It was placed in approximately 1 m deep boreholes spreading along the seismic profile. In this manner we successfully acquired refraction data from a depth of up to 50 m (Stopar, 2005). As a source of transversal wave motion we used a sledgehammer and specially designed wooden plank.

The same shot-points as for surface refraction were then used also for tomographic survey between the surface and the exploration gallery. Geophones were installed in the ceiling of the exploration gallery as shown in Figure 3. Seismic profile in the right exploration gallery consists of three linear arrays (72 geophones) and in the left exploration gallery of two arrays (48 geophones). The distance between geophones was also 4 m.

Figure 3. Vertical and horizontal geophone mounted on the ceiling of exploration gallery
Slika 3. Vertikalni in horizontalni geofon pritrjena na stropu raziskovalnega rova

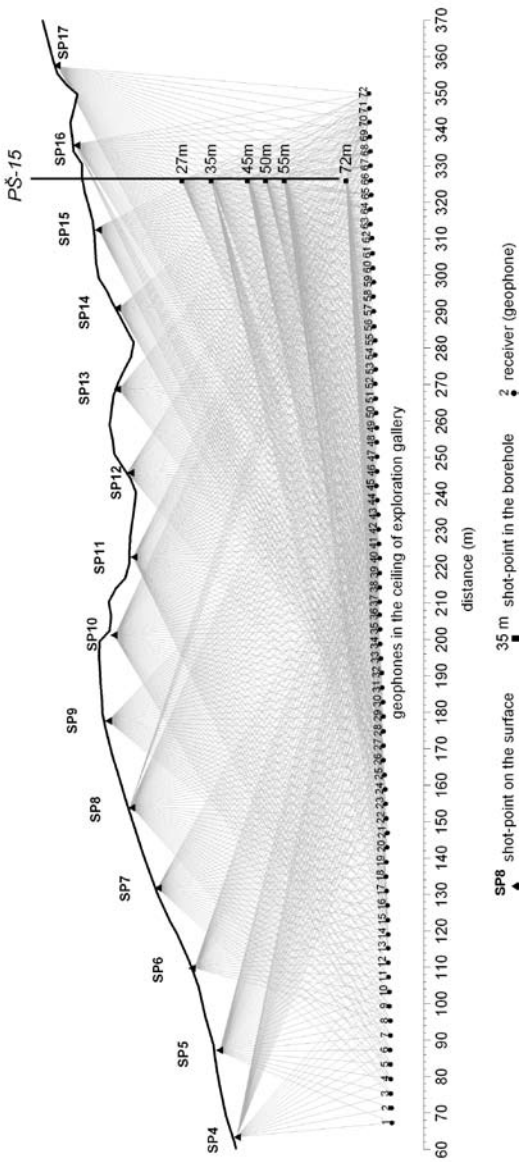

Figure 4. Tomography ray-density coverage for seismic rays between the right exploration gallery, the surface and the borehole PŠ-15
Slika 4. Gostota seizmičnih žarkov pri tomografiji med desnim rovom, površino in vrtino PŠ-15

Tomography was performed also between the right and the left exploration galleries. Geophones were located in the left gallery and the shot-points in a short section of the right exploration gallery and cross-passage (Figure 10). For the shot-points we drilled shallow boreholes (approximately 1 m) in which we inserted explosive.

To improve tomographic velocity fields in the lateral direction, tomography between boreholes and the exploration gallery was also conducted. The geophones were in the same locations in the ceiling as for tomography between the exploration gallery and the surface. Shot-points locations for tomography in the right exploration gallery were inside the borehole PŠ-15. The borehole PŠ-15 was 72 m deep. The shot-points in this borehole were at depths of 72 m, 55 m, 50 m, 45 m, 35 m and 27 m. The shot-points locations for tomography between the left exploration gallery and the boreholes PŠ-14 and PŠ-17 were in the borehole PŠ-17 at depths of 83 m, 78 m, 66 m, 53 m, 43 m, 33 m and 23 m. In the borehole PŠ-14 an obstruction occurred so that it was only possible to reach a depth of 50 m. Therefore the shot-points in PŠ-14 were at depths of 50 m, 40 m, 30 m and 25 m. Figure 4 represents tomography ray-density coverage for seismic rays between the right exploration gallery, the surface and the borehole PŠ-15. The boreholes PŠ-15 and PŠ-17 were out of the exploration gallery alignment for 15 m and 17 m, respectively (Figure 1). Thus corrections of the measured travel times were made.

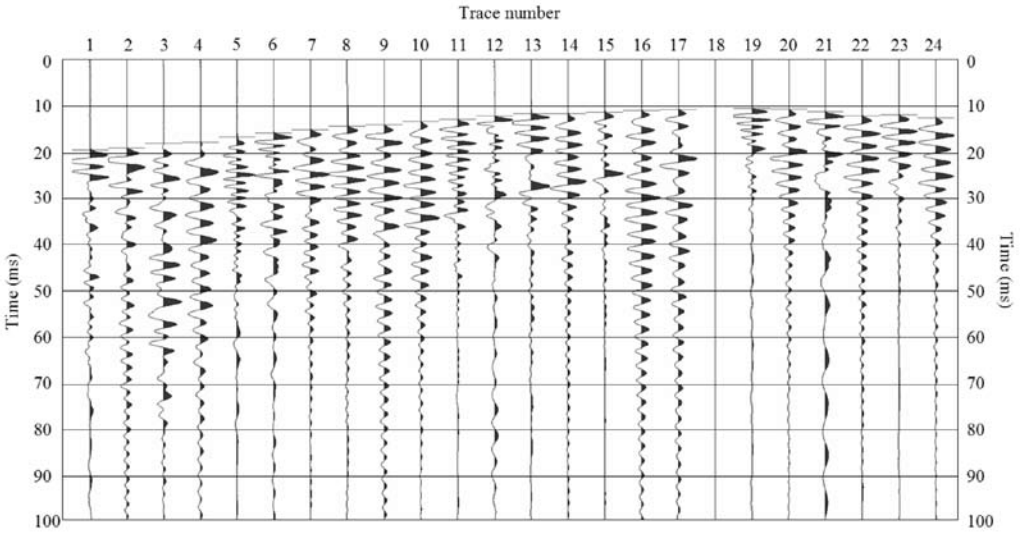

Figure 5. A representative seismic record with first arrivals picks obtained with explosive source on the surface and receivers in the exploration gallery
Slika 5. Značilen seizmični posnetek s prvimi prihodi seizmičnega signala pridobljen s proženjem eksploziva na površini in sprejemniki v raziskovalnem rovu

SEISMIC DATA ANALYSIS AND MODELLING

A total of 10176 travel times were recorded. Figure 5 shows a representative example of seismic records with corresponding picks of first arrivals of seismic waves, obtained with seismic tomography between the exploration gallery and the surface.

Initial data processing involved tomographic inversion based on a nonlinear optimization method using a generalized simulated annealing algorithm. The preliminary velocity data from the surface refraction seismic, interval velocities from the boreholes PŠ-14, PŠ-15 and PŠ-17 and the lithological data were used as constraints in the starting model. The final velocity model of the P waves acquired from tomography data between the surface, the right exploration gallery and the borehole PŠ-15 with 17901 nodes (81 by 221) and cell dimensions of about 1.5 m in both directions, is shown in Figure 6a. For seismic tomography of the S waves between the surface and the right exploration gallery, the tomographic calculations were carried out on a regular rectangular grid that occupied an area of about 330 m (horizontal) by 100 m (vertical), with 588 nodes (14 by 42) spaced at intervals of about 8 m in both directions (Figure 7).

Next, a more detailed processing by the use of the inversion algorithm based on the SIRT was performed. For seismic P-wave tomography between the surface, the right exploration gallery and the borehole PŠ-15 the tomographic calculations were carried out on a regular rectangular grid that occupied an area of about 300 m (horizontal) by 100 m (vertical), with 1220 nodes (20 by

61) spaced at intervals of about 5 m in both directions (Figure 6b). Figure 8 represents the final velocity model of the P waves acquired from tomography data between the surface, the left exploration gallery and the boreholes PŠ-14 and PŠ-17. The model consists of 700 nodes (25 by 28) spaced at intervals of about 7 m and 6 m in the *x* and *y* directions, respectively. In order to build a reasonable initial model for the curved-ray inversion, we started by inverting the travel time data with a straight-ray approximation using an initial velocity model obtained from the surface refraction data. A smoothed version of the updated model, obtained after 16 straight-ray iterations, was then used as a starting model for the successive curved-ray iterations. Before running new iterations, however, several explicit global and node constraints were incorporated into the model. Global constraints were imposed specifying the maximum and minimum allowable velocities, which equal to 6000 and 340 m/s (the P-wave velocity in the air), respectively. Node constraints, which force the solution to match known boundary values, were applied with a fuzzy logic approach (Jackson and Tweeton, 1994) using measured specimen velocities and other supplemental site information. Constraining the grid node is mainly where low ray-coverage imposed by source-to-receiver geometry, improved mathematical resolution by reducing the ill-conditioning of the inversion. For seismic tomography of the S waves between the surface and the left exploration gallery the tomographic calculations based on the SIRT technique was also performed. Due to a bad signal-to-noise ratio in the S wave data we had to use a smaller amount of data. That is why the model consists of 121 nodes and the cell dimensions are approximately 28 by 10 m (Figure 9). The tomographic calculations of the P waves data between the right and the left exploration gallery were carried out on a regular rectangular grid with 450 nodes (45 by 10) spaced at intervals of about 6.7 m and 5.5 m in *x* and *y* directions, respectively (Figure 10).

From the relation between the longitudinal and the transversal wave velocity, the dynamic elastic moduli were calculated. For the calculations we also needed the rock density data. The data were obtained from observations, laboratory and in situ measurements and are shown in Table 2 (Likar and Čadež, 2006). Calculations were based on a regular rectangular grid that occupied an area of about 340 m (horizontal) by 110 m (vertical), with 588 nodes (42 by 14) spaced at intervals of about 8 m in both directions. Rock density distribution inside the grid was determined with linear interpolation based on the range of wave velocity inside individual cells. We consider that higher seismic velocity corresponds to higher rock density and vice versa.

Results and discussion

Tomography between the right exploration gallery, the surface and the borehole PŠ-15

With the tomography between the right exploration gallery, the surface and the borehole PŠ-15 we acquired the exact data above the right tube of the Šentvid tunnel (Figure 6). From the result of modelling based on a nonlinear optimization method a low P velocity zone (velocities under 3000

Table 2. Rock density in the Šentvid tunnel area
Tabela 2. Gostota kamnin na območju predora Šentvid

Lithology	φ (g/cm^3)
Intercalations of meta-sandstone and meta-siltstone, meta-sandstone typically prevailing	2.65
Meta-siltstone with meta-sandstone layers/lenses, locally with slate layers	2.55
Slate, locally with meta-sandstone/ meta-siltstone layers	2.45
Fault breccia, fault gouge	2.30

m/s), which extends from the surface to the depth of about 30 m and indicates disintegrated rock, may be distinguished (Figure 6a). This low velocity zone is thicker on the side adjacent to the Celovška street, where parts of highly tectonised materials (probably shaly claystone) are anticipated. The second zone, characterized by P-wave velocities over 4000 m/s at distances of about 220 to 340 m, represents a more compact rock mass. With the use of the inversion algorithm based on the SIRT we acquired a more detailed P-wave distribution (Figure 6b). Up to distance of about 120 m we have disintegrated material, which resulting in low velocity zone. From that distance further a higher velocities are present, which corresponds to compact rock mass, presumably sandstone. In the vicinity of the shot-points on the surface are, due to higher resolution, noticeable abnormal areas with P-wave velocity around 3000 m/s. Individual curved shapes may indicate some geological structures, especially fault zones and incidental lithological layers. Low velocity zone in the right gallery, from 120 to 150 m, indicates highly tectonised zone. In general, the more compact rock masses correspond to P velocities of about 4000 m/s.

We obtained similar results from a tomographic S waves velocity image (Figure 7). Zone of the compact rock (S velocity over 1500 m/s) coincides with the results obtained from the tomographic P waves velocity image between the right exploration gallery, the surface and the borehole PŠ-15. Due to difference in cell dimensions between the S wave velocity model (cell size 8 by 8 m) and the P wave velocity model (cell size 1.5 by 1.5 m), the values of S wave velocity above the right exploration gallery are less reliable. From those models we can deduce that rock materials above the right tunnel tube is mostly tectonised, a minor zone of a compact rock is only in the lower right part of the tomogram, at distances of about 200 m to 320 m.

Tomography between the left exploration gallery, the surface and the boreholes PŠ-14 and PŠ-17

Figure 8 presents the result of the tomography between the left exploration gallery, the surface and the boreholes PŠ-14 and PŠ-17. As expected, lower P wave velocities (lower than 2000 m/s) are on the surface, where soil and weathered rock are present. With depth the velocity increases and in the central part of the tomogram, around elevation of 370 m, it exceeds 4000 m/s. This material corresponds to seismic compact rock mass. Relatively low seismic velocities (P velocity under 3500 m/s) appear at the beginning of the left exploration gallery, i.e. up to the distance of 140 m. This corresponds to a more tectonised rock, but also indicates a fault zone. At a distance of about 180 m in the left gal-

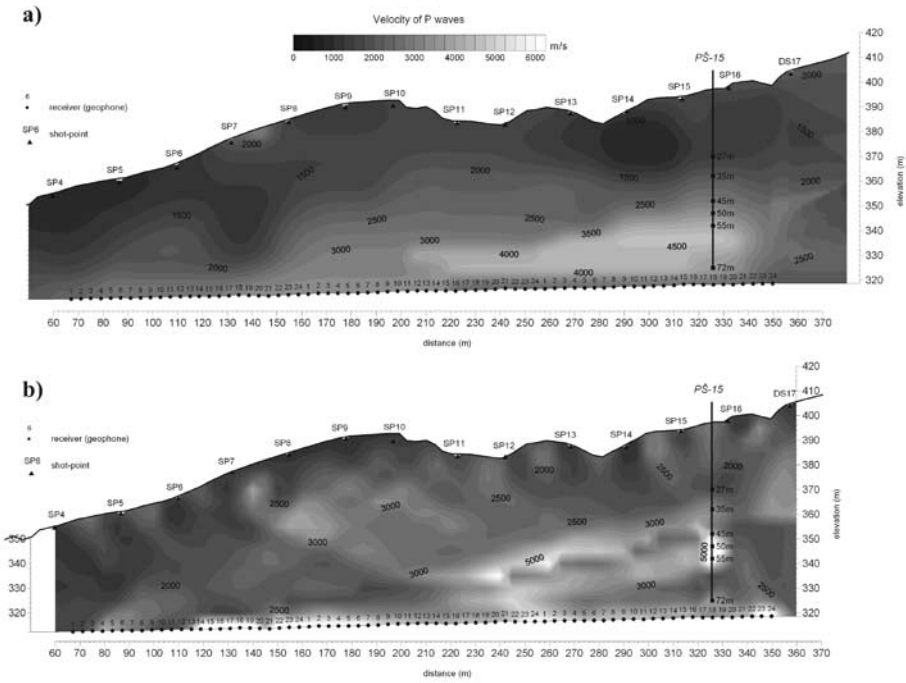

Figure 6. Tomographic P waves velocity image between the right exploration gallery, the surface and the borehole PŠ-15: a) nonlinear optimization method, b) SIRT method

Slika 6. Slika hitrosti P valov pridobljenih s tomografijo med desnim raziskovalnim rovom, površino in vrtino PŠ-15: a) nelinearna optimizacijska metoda, b) SIRT metoda

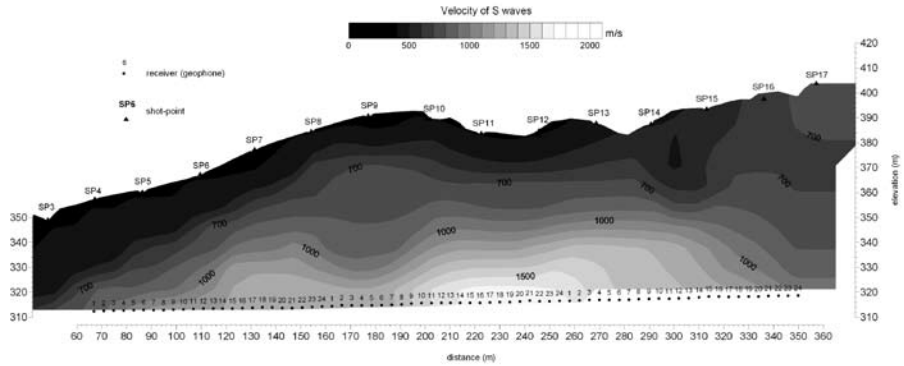

Figure 7. Tomographic S waves velocity image between the right exploration gallery, the surface and the borehole PŠ-15 (nonlinear optimization method)

Slika 7. Slika hitrosti S valov pridobljenih s tomografijo med desnim raziskovalnim rovom, površino in vrtino PŠ-15 (nelinearna optimizacijska metoda)

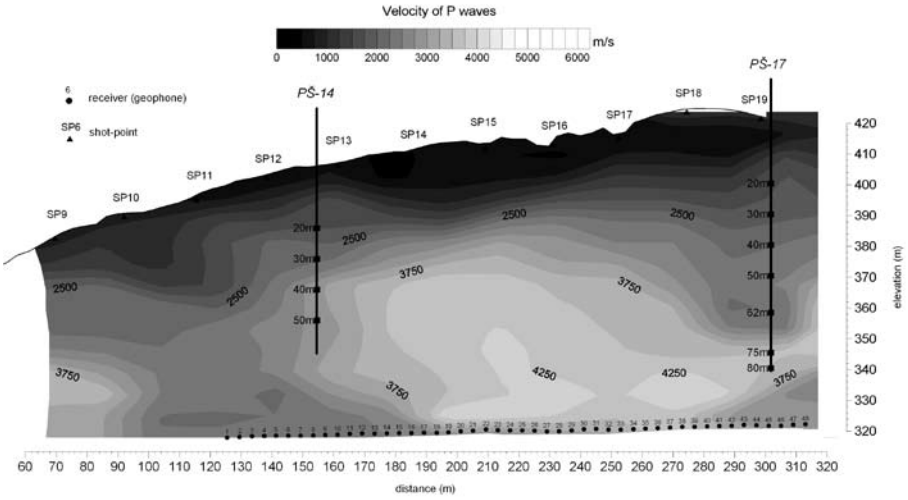

Figure 8. Tomographic P waves velocity image between the left exploration gallery, the surface and the boreholes PŠ-14 and PŠ-17 (SIRT)
Slika 8. Slika hitrosti P valov pridobljenih s tomografijo med levim raziskovalnim rovom, površino in vrtinama PŠ-14 in PŠ-17 (SIRT)

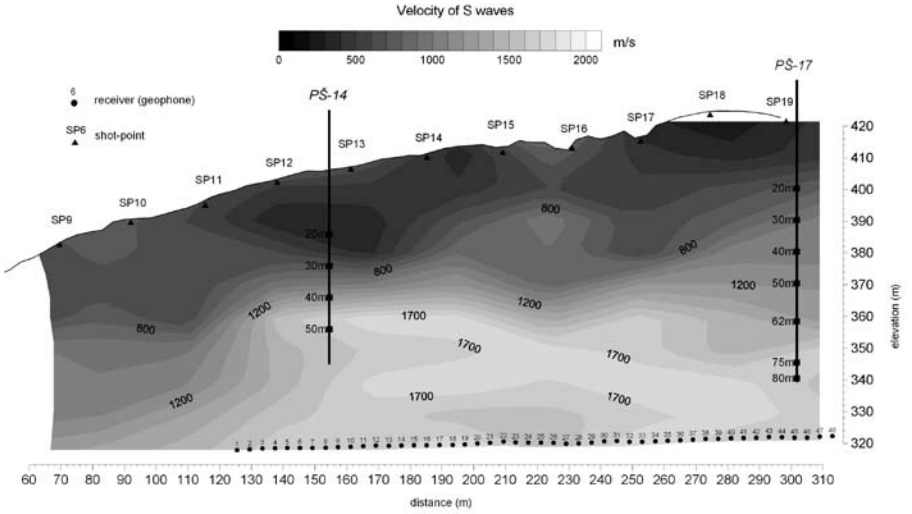

Figure 9. Tomographic S waves velocity image between the left exploration gallery, the surface and the boreholes PŠ-14 and PŠ-17 (SIRT)
Slika 9. Slika hitrosti S valov pridobljenih s tomografijo med levim raziskovalnim rovom, površino in vrtinama PŠ-14 in PŠ-17 (SIRT)

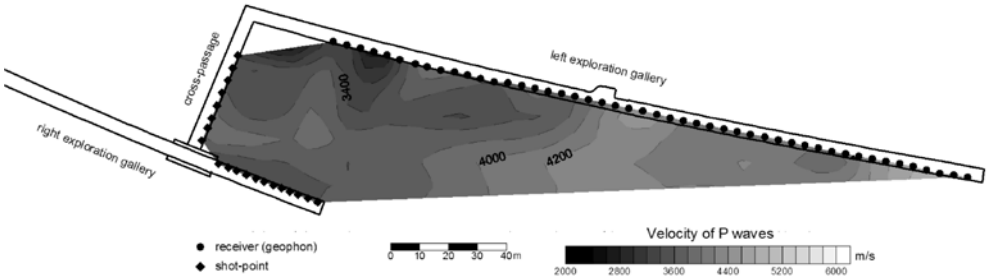

Figure 10. Tomographic P waves velocity image between the right and the left exploration gallery (SIRT)
Slika 10. Slika hitrosti P valov pridobljenih s tomografijo med desnim in levim raziskovalnim rovom (SIRT)

lery we find more favourable conditions. The P wave velocities over 4000 m/s correspond to a compact rock, most likely to sandstone. The overburden height in the left exploration gallery is higher than in the right exploration gallery. For that reason seismic data from tomography above the left exploration gallery did not have sufficient resolution to correctly image the low velocity zone at the beginning of the left gallery.

From the tomographic S waves velocity image (Figure 9) similar result was obtained. Because water does not influence propagation of the transversal waves, low velocity surface layers could be even thicker. Nevertheless, higher S velocities (above 1500 m/s) indicate more compact rock mass. In modelling of the S wave velocity field above the left exploration gallery only half the amount of data as for P waves velocities was used. Thus the S wave velocity image resolution is smaller than the resolution of the P wave velocity image (Stopar, 2005).

Tomography between the right and the left exploration gallery

The final velocity model of the P waves acquired from tomography data between the right and the left exploration galleries is shown in Figure 10. In the first 80 m from the cross-passage, the velocity model is rather reliable. From that point further the image of P wave velocity is unreliable, due to almost parallel seismic rays. At the start of the left exploration gallery a low velocity zone, with velocity varying from 3000 to 3500 m/s, was found. According to geological data acquired during the exploration gallery construction that low velocity zone correlates with highly tectonised claystone and siltstone. Velocity increases in the direction along the left exploration gallery, where one of the merging caverns is planned. Although that velocity is relatively high, the materials in this area are moderately tectonised. At tomography between the right and the left exploration galleries we do not have to deal with surface soil and weathered materials. Thus the P wave velocities are higher than the values

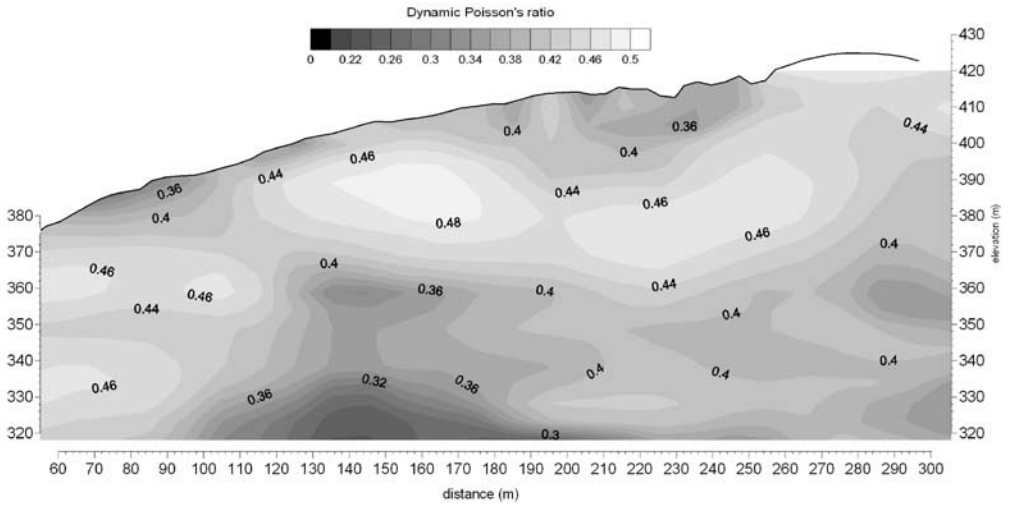

Figure 11. An example of obtained dynamic elastic moduli – values of dynamic Poisson's ratio above left exploration gallery
Slika 11. Primer pridobljenih dinamičnih elastičnih modulov – vrednosti dinamičnega Poissonovega količnika nad levim raziskovalnim rovom

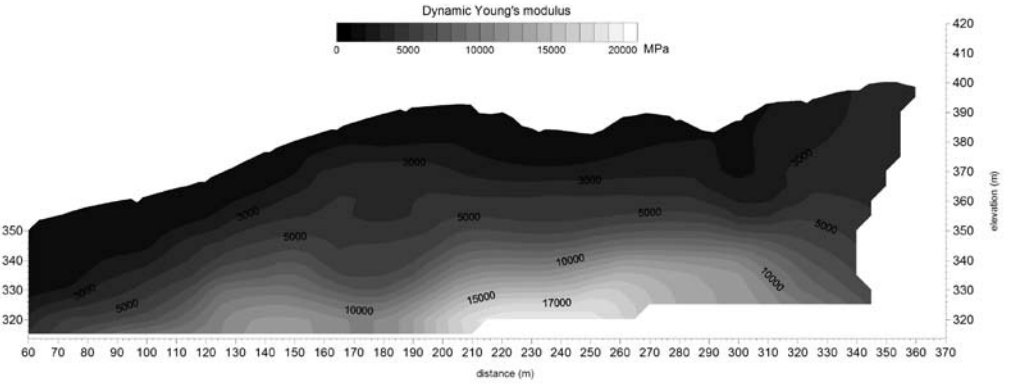

Figure 12. An example of obtained dynamic elastic moduli – values of dynamic Young's modulus above the right exploration gallery
Slika 12. Primer pridobljenih dinamičnih elastičnih modulov – vrednosti dinamičnega Youngovega modula nad desnim raziskovalnim rovom

obtained with tomography between the surface and the exploration gallery. Higher disintegration of material is also a consequence of the exploration gallery construction.

Seismic dynamic elastic moduli

We determined that values of dynamic Poisson's ratio vary from 0.24 to 0.48 (Figure 11). Higher values of dynamic Poisson's ratio near the surface are a consequence of saturated weathered and disintegrated material. The values of the dynamic Young's modulus vary from 1000 to 20000 MPa as shown in Figure 12. Compared to laboratory acquired Young's moduli for different rock types (Table 1), the calculated dynamic Young's moduli are one magnitude greater. The dynamic shear modulus varies from 200 to 7000 MPa and the dynamic bulk modulus varies from 100 to 40000 MPa. A larger anomaly appears along the right exploration gallery at distance of approximately 220 m, where values of the dynamic elastic moduli are higher. According to the seismic velocity data, the data from boreholes and other geological information, we can deduce that rock mass here is less tectonised.

Taking mutual relations between dynamic elastic moduli and P and S wave velocities into account, the similarity of geological structures in all the images is not surprising. The ratio between the static and dynamic elastic moduli depends on the type of material and is usually smaller than one. The real meaning of the dynamic elastic moduli is that we can use them to distinguish between geotechnically good and weak rock masses, because in contrast to laboratory measurements a larger volume of the material is taken into consideration.

Conclusions

The goal of geophysical investigations was to obtain seismic parameters to define geomechanical rock mass characteristics in the region of planned merging caverns. Final solutions are the P and S wave velocity fields with additional dynamic elastic moduli calculations. All the solutions well indicate areas of a more compact rock mass. The real value of acquired data is that it presents "in-situ" conditions along the tunnel alignment. Seismic measurements between the surface and the exploration gallery were, difficult to perform due to large distances, several communications, urban noise and construction works in the exploration gallery. In spite of all that, the seismic P wave propagation signal was of good quality, only the signal data of the S wave propagation was less satisfactory, especially those from the most distant shotpoints. The tomographic velocity models of the P waves present a satisfying complementary solution for locating merging caverns. The S wave velocity results of the tomography between the surface, the exploration gallery and the boreholes are not so good than the P wave velocity results. Reasons for that could be in a less accurate determination of the transversal waves arrivals, in a smaller amount of information due to worse signal-to-noise ratio and also because the variations of geomechanical parameters have a more significant effect on transversal than on longitudinal waves. Nevertheless the velocity fields of longi-

tudinal and transversal waves and the dynamic elastic moduli distribution well indicate areas of a more compact rock mass.

Povzetek

Uporaba seizmične tomografije pri raziskavah AC trase na območju predora Šentvid

Predmet geofizikalnih raziskav je bilo območje izgradnje predora Šentvid. Šentviški hrib bo avtocesta prečkala v obliki dveh ločenih predorskih cevi s priključnima cevema, poseg pa je zaradi neugodne geološke zgradbe zelo zahteven. Ker na podlagi predhodno izvršenih preiskav ni bilo mogoče natančno določiti lokacij priključnih kavern, je bil najprej izdelan raziskovalni rov, v katerem so bile izvedene različne geološke, geomehanske in geofizikalne raziskave. Cilj geofizikalnih raziskav je bil, s pomočjo seizmičnih parametrov, določiti geomehanske karakteristike posameznih kamnin v območjih načrtovanih priključnih kavern. Geofizikalne raziskave so vključevale površinsko seizmično refrakcijsko profiliranje in seizmično tomografijo med površino, vrtinami in raziskovalnim rovom.

Rezultati seizmičnih preiskav v in nad raziskovalnim rovom predora Šentvid odražajo predvsem mehanske lastnosti preiskovane kamnine v nadkritju predora. Vrednost pridobljenih podatkov je v tem, da predstavljajo "in-situ" podatek vzdolž zveznih profilov. Glede na to, da velik del vrednosti hitrosti longitudinalnega valovanja izvedenih raziskav seizmične tomografije dosega 3000 m/s in več, lahko govorimo o hribini. Izjema so površinske plasti, ki zlasti v smeri proti severnemu portalu dosegajo tudi debelino več deset metrov. Posamezne nižje hitrostne anomalije so posledica pretrte kamnine ali prelomnih con. Seizmične raziskave so dobro podale območja kompaktnejše kamnine, kar odražajo tako slike hitrosti longitudinalnega in transverzalnega valovanja kot tudi slike dinamičnih elastičnih modulov. Predvideni lokaciji priključnih kavern sta bili na osnovi dodatnih raziskav, med katere sodijo tudi geofizikalne, potrjeni.

References

Brenčič, M. (2000): *Hidrogeološko poročilo za predor Šentvid*. Geološki zavod Slovenije, Ljubljana, unpublished report, 45 p.

Cosma, C., Ihalainen, M., Korhonen, R. (1984): The Crosshole Seismic Method. *Report of phase II. of development programme*. Helsinki, 36 pp.

Čadež, F., Kleberger, J., Genser, W., Pöschl, I. (2004): Sentvid Motorway Tunnel – Interim Results from Slovenia's Most Recent Exploration Gallery. *7. mednarodno posvetovanje o gradnji predorov in podzemnih prostorov, zbornik referatov*. Uredila: Kostiov, L. in Likar, J., Ljubljana: Društvo za podzemne in geotehnične konstrukcije in Univerza v Ljubljani, pp. 50-56.

Dines, K. A. and Lytle, J.R. (1979): Computerized Geophysical Tomography. *Proceedings of the IEEE*.; Vol. 67, No. 7, pp. 1065-1073.

Fifer Bizjak, K., Petkovšek, B., Petrica, R. (2003): Geološke in geomehanske raziskave za predor Šentvid. *Gradbeni vestnik*.; Vol. 52, pp. 15-21.

Jackson, M.J., Tweeton, D.R. (1994): MIGRATOM – Geophysical tomography using wavefront migration and fuzzy constraints. *USBM Report of Investigation 9497*. United states department of the interior, Bureau of mines, 35 p.

Likar, J., Čadež, J. (2006): *Verification analysis of the stability of large underground caverns in the three-lane road tunnel Šentvid*. FLAC and Numerical Modeling in Geomechanics – 2006, proceedings of the 4th international FLAC symposium, Spain, pp 71 – 77.

SeisOpt@2d (2002): Ver. 3.0, *Seismic Refraction Tomography software copyright Optim, Inc.*, University of Nevada, Reno, Nevada.

Stopar, R. (2005): *Poročilo o geofizikalnih preiskavah na območju predora Šentvid (levi in desni raziskovalni rov)*. Geoinženiring d.o.o., Ljubljana, unpublished report, 16 p.

Žigon, A., Žibert, M. in Jemec, P. (2004): Projektiranje predorskega sistema Šentvid. *7. mednarodno posvetovanje o gradnji predorov in podzemnih prostorov, zbornik referatov.* Uredila: Kostiov, L. in Likar, J., Ljubljana: Društvo za podzemne in geotehnične konstrukcije in Univerza v Ljubljani, pp. 125-147.

Surveying for geophysical exploration, using a single-frequency global navigation satellite system receiver capable of 30 cm horizontal kinematical positioning uncertainty

Uporaba enofrekvenčnega sprejemnika GNSS s 30 cm negotovostjo v kinematičnem načinu dela za terenske geofizikalne preiskave

Franc Dimc[1], Branko Mušič[2], Radko Osredkar[3]

[1]University of Ljubljana, Faculty of Maritime Studies and Transportation, Pot pomorščakov 4, SI-6320 Portorož, Slovenia; E-mail: franc.dimc@fpp.uni-lj.si
[2]University of Ljubljana, Faculty of Arts, Department of Archaeology, Zavetiška 5, SI-1000 Ljubljana, Slovenia; E-mail: branko.music@ff.uni-lj.si
[3]University of Ljubljana, Faculty of Computer and Information Science, Tržaška cesta 25, SI-1001 Ljubljana, Slovenia; E-mail: radko.osredkar@fri.uni-lj.si

Received: January 7, 2008 **Accepted:** February 25, 2008

Abstract: Some preliminary tests of various types of inexpensive Global positioning system (GPS) receivers were performed in order to assess the utility of the technique to geophysical surveying conditions. A 30 cm basic kinematical accuracy of the fixes was sought. Different sources of positioning errors are analyzed under different, realistic conditions in the field (multipath, satellite obscuration, etc) and the influence of the sampling rate and phase data processing on the relative accuracy for static and kinematical positioning analyzed. It is demonstrated that under favorable conditions a 30 cm relative uncertainty of the kinematical positioning is achievable and that under conditions where a degradation of the GPS fixes occurs during the scans, it is possible to a certain extent, by post-processing of the measurement data, to compensate for the errors and to refine the positioning results.

Izvleček: V članku so predstavljeni začetni preizkusi različnih vrst cenejših sprejemnikov GPS, opravljenih z namenom ugotoviti uporabnost radionavigacijske satelitske tehnike za geofizikalne preiskave. Preizkuse smo začeli z namenom ugotavljanja, če je natančnost določitve položaja 30 cm dosegljiva. Na terenih smo analizirali različne vzroke napak (večpotje, zastrtost satelitov) in vpliv pogostnosti odčitavanja in obdelave faze na relativno natančnost statičnih in kinematičnih preizkusov. Pokazali smo, da je v dobrih pogojih relativna natančnost 30 cm dosegljiva in da je v določenih pogojih možno z naknadno obdelavo odčitkov (kompenzacijo napak) rezultate popraviti.

Scientific paper

Key words: GPS tracking, kinematic measurements, geophysical exploration
Ključne besede: sledenje z GPS, kinematične meritve, geofizikalne raziskave

INTRODUCTION

The idea behind the construction of an inexpensive single frequency GPS system that is simple to use arises from the need for flexibility and effectiveness of geophysical surveys. A sufficient degree of flexibility can only be assured by the complete autonomy of the team in the planning and executing of fieldwork through the positioning of identified anomalous areas. This is the data layer in integral bases, which in archaeo-geophysical prospection represents the basis for the planning of further systematic and detailed geophysical research on identified sites through the application of the multi-method approach (see: MUŠIČ & HORVAT, 2007; MUŠIČ et al., 2008).

GPS equipment (receivers) is relatively cheap, is easily portable, offers real-time fixes and thus makes kinematical positioning possible (WANG et al., 2002). Neither does its application require specialist skills. It makes GPS positioning technology well suited for autonomous geophysical prospection (GAFFNEY, 2003), in particular in large-scale evaluation projects, where total detailed survey is not as important as establishing background levels and acquiring a good understanding of the effects of the geology and pedology. Its efficient application is of crucial importance for surveys in the regions where geodetic fixed points for terestrial position meaurements are not accessible. The nominal accuracy of the GPS positioning can be greatly improved by advanced signal processing and post processing, which means that a 30 cm accuracy of kinematical relative positioning (VAN SICKLE, 2001), deemed sufficient for the autonomous use of the GPS for geophysical prospection, is attainable.

It is characteristic of GPS positioning methods that the accuracy of relative positions fixes is usually considerably better than the accuracy of absolute position fixes. After a comprehensive post-processing efforts a very accurate static positioning by single frequency GPS receiver it is also possible (BERAN, 2007). We have thus attempted to improve the performance of relatively inexpensive GPS receivers by use of reference points of known position in the field. We were concerned solely with horizontal positioning, which is of primary importance, leaving the more difficult problem of vertical positioning to a future project. In the autonomous mode with a single frequency receiver, the position of a reference point is first measured as accurately as possible. A roving receiver then continuously corrects its position outputs by calculating its pseudo range by using single pseudo range differences (DGPS) obtained from a nearby monitoring static GNSS station on a known location, from a network of such stations, or from geostationary satellites known also as SBAS (VAN SICKLE, 2001).

Kinematical sub-meter accuracy as determined by a single receiver was also stud-

ied. This requires time triggering and/or event triggering of the logging process, and a synchronization of the process with position output acquisition. In the kinematical acquisition mode, if there is insufficient time for the settlement of the position outputs, the positioning device must still ensure sufficient continuous accuracy. When settlement of geophysical results takes minutes, instead of seconds, semi-kinematical positioning is possible. This requires the surveyor to return to a reference measurement point after a certain period of time.

Positioning and accuracy of positioning by GPS

When at least four satellites are in view of the receiver, it is possible to calculate a three dimensional position from the received data. The computation of position is influenced by the propagation of the signals from the satellites through the atmosphere, and stability of the satellite clocks. Weak satellite signals, coded for higher accuracies, are distinguished from the noise with correlation techniques. In addition to time signals, the GPS receiver also receives

Table 1. Some of the frequently used abbreviations
Tabela 1. Seznam pogosteje uporabljanih kratic

CP	Carrier phase. A phase of a signal that carries the information
DGPS	An augmentation system whereby radionavigation signals are monitored at a known position and the corrections so determined are transmitted to users in the coverage area.
DOP	A dimensionless number that accounts for the contribution of relative satellite geometry to errors in position determination.
GNSS	Generic term for satellite navigation systems. GNSS-1 covers GPS and GLONASS augmented with additional ranging, differential and integrity signals (eg EGNOS, MSAS, WAAS).
GPR	Ground Penetrating Radar
HDOP	The factor by which a two-dimensional fix in a horizontal plane is degraded by geometrical considerations.
RMS	The variability of a measurement such as a single line of position in one dimension; with no bias also an estimate of the standard deviation of the errors.
2DRMS	Twice the root-mean-square of the radial distances from the true position to the observed positions obtained from a number of trials Should contain 95% of observed positions.
TPS	Total positioning station
UERE	User equivalent range error. Any error contributing to the error budget of a stand-alone satellite navigation receiver, expressed as an equivalent error in the range between the user's receiver and satellite. Total UERE is the root sum square of the individual errors.
UTM	Universal Transverse Mercator, a projection whereby a meridian as line of contact between projection plane and Earth surface are used
VDOP	The factor by which the one-dimensional vertical accuracy of a fix is degraded by geometrical considerations.

navigation signals comprising positions of satellites and their operational status. Receivers can operate in an autonomous mode or as rovers. Higher accuracies can normally be achieved by also taking into account the corrections transmitted by a primary positioning receiver station, located at a known position. Single, double and triple difference methods diminish some of the errors generated either by the primary station and/or the rover and the satellites (VAN SICKLE, 2001).

Equipment manufacturers normally state the accuracy of positioning of their products with respect to certain conditions (signal to noise ratio) of reception, and this is considered as the greatest possible absolute accuracy that can be achieved by a device. However, nominal accuracy does not depend solely on the stated conditions, but to a much larger extent on processing and post processing of the satellite data available to the receiver. In satellite positioning it is impossible to completely exclude all the environmental factors that may influence the results. They result in an accuracy interval, which is related to the experimental standard deviation (estimated position error, also known as (d)RMS error) (USM, 1999). Since more variables (dimensions) are observed, the accuracy is noted in each dimension separately. Two dimensional (2DdRMS) is calculated for two variables. The compound error of positioning is the result of all the contributing factors: inaccurate satellite ephemeris data and inaccurate clock corrections sent, changes of propagation delays due to ionosphere density fluctuations with solar or geomagnetic activity and signals reflected from highly conductive surfaces resulting in multipath signals at the receiver position, disturbing the processing of the directly received signals and receiver thermal noise. Processing methods (phase averaging, estimation filter scenarios) of the raw signals also influence the accuracy of the results.

Reducing the influence of the limited receiver view of satellite constellation (dilution of precision, DOP: HDOP – horizontal DOP, VDOP – vertical DOP) during signal processing yields the final positioning error, the so called "user equivalent range error" (UERE) (DE JONG et al., 2001). The precision of a position measurement output (known as the fix) depends both upon the measurement geometry, as represented by the DOP values, and range errors caused by signal strength, ionospheric effects, and multipath errors. The latter depend upon physical surroundings of the measuring point, i.e. to terrain relief, near-by buildings or other highly reflective surfaces (water bodies), or foliage plants (LACHAPELLE at al., 1994). Multipath errors cause systematic variations of GPS fixes, while other sources of errors cause random, chaotic or bias type of variations. Overall uncertainty of positioning of a point is thus calculated as a product of the accuracy (experimental deviation of the measurements) and DOP (VAN SICKLE, 2001).

The positioning accuracy of a moving receiver (rover) is in general not equal to the uncertainty of a stationary fix and should at a certain areas be determined separately. For this purpose a reference trajectory (charted path, on-site measured distances) is established and marked on the measurement site. Deviations of fixes from the reference trajectory are measured while tak-

ing the velocity of the rover into account. Uncertainty of kinematical positioning is defined (USM, 1999) as the standard deviation from the mean value or the true value if known. It has been calculated in our work from the distances of fixes against a reference trajectory marked on the ground.

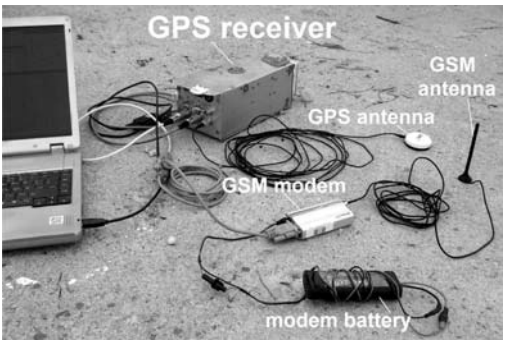

Figure 1. Test GPS equipment
Slika 1. GPS oprema za preizkusne meritve

GNSS ACCURACY REQUIRED FOR GEOPHYSICAL PURPOSES

A basic requirement of geophysics is determined as a 30 cm uncertainty in kinematical positioning. A positioning system should satisfy the demands of geophysical fieldwork, such as real-time position output acquisition with the specified accuracy. A special concern in geophysical field work is the accuracy with which the user can return to an already measured position with the same navigation system. In evaluating the positioning results, it should be understood that accurate static positioning does not necessarily lead to accurate kinematical positioning. Obstacles obscuring or reflecting the signals from satellites, and the pattern of positions of obstacles in the field, often change the conditions of reception along the positioning trajectory, causing multipath errors.

When using a low-cost GPS receiver, measurement errors, i.e. multipath and antenna variations in carrier phase, are much more likely to cause problems than with high performance receivers. Kinematical accuracy is determined from the root mean square differences between the position outputs and the nearest point on the reference trajectory. It strongly depends on the velocity of the roving receiver and capabilities of the GPS software. In our work velocities up to 3 m/s have been considered.

In testing the viability of a GPS based positioning sytem for geophysical fieldwork the following equipment was used (see Figure 1):

- Single frequency GPS receivers: R1 Allstar (12 channels, 1 Hz), R2 Allstar (12 channels, 5 Hz), Novatel , R3 GPSmap C60, Garmin,
- antenna: Aero AT 575-70, (gain: 26 dB), Canadian Marconi Company,
- total station: TPS 1100 (Leica),
- GSM modem: Fastrack M1206B-on, Wavecom,
- logger: laptop computer,
- log software: Starview,
- processing data: Matlab (Mathworks), in case of more than one geodetic point available, a transformation from GPS data to local geodetic system was used.

For the comparison reasons two more GPS receivers which were not involved in the fieldwork are also taken into consideration: R4 FlexPak-V1, NovaTel and R5 SR 20, Leica Geosystems. The lowest RMS can be achieved by the R5 (0.3 m, after CP post-

Table 2. Test sites with brief descriptions
Tabela 2. Oznake preizkusnih terenov s kratkimi opisi

Site label	Description
S1	sports field, predefined geometry
S2	archaeological site Veselov Cvinger, near Stična
S3	a car park in front of a building in Ankaran
S4	the surroundings of the geodetic point at Malija
S5	an archaeological site Dolge njive, near Vrhnika
S6	an archaeological site Tanagra, Greece

processing) whereas the highest 2DRMS is get by the commercial R3 (static 2.5 m). Under good receiving conditions the experimentally observed RMS values might become very similar, however in atmosphere changing conditions for example a benefits of R5 would result in lower RMS as of R3. Comparison of the prices to the price of R3 as the etalon price (1 EP) gives the following sequence: R2 as already obsolete device (1.9 EP), R4 (5 EP) and R5 (from 10 EP up to 13 EP).

RESULTS AND DISCUSSION

Test sites and equipment types

In order to test the positioning capabilities and accuracy of a GPS system, several types of equipment were tested at 5 different and well defined testing areas: the Adria sports field at Ankaran (site S1), an archaeological site at Veselov Cvinger, near Stična (site S2), a car park in front of a building in Ankaran (site S3), the surroundings of the geodetic point at Malija (site S4), and an archaeological site of Nauportus at Dolge njive, near Vrhnika (site S5) (see: MUŠIČ & HORVAT, 2007; MUŠIČ et al. 2008). The third archaeological site is Tanagra (Greece) (site S6) (see: BINTLIFF et al., 2000, 2002; BILC, 2003; MUŠIČ et al., 2004). The different locations have considerably different topological and signal propagation characteristics: Site S1 (a sports field) has simple geometry and is topologically well defined, site S2 is an exposed location on a ridge, signals at site S3 are especially prone to multipath errors and signal losses due to obscuration, site S4 (geodetic reference point of the 1st degree) has a well defined position and low multipath variations, however it is exposed to interference and other errors, and site S5 is an archaeological site close to a river.

A summary of the static positioning measurement results on the sites is given in Table 3. It can be seen that uncertainty of fixes is decreased by the absence of multipath errors as well as open sky, and by the use of DGPS. Uncertainty was calculated for three locations: Site S2 where moderate multipath error was observed (point No. 1, was used further as a reference point at this site, as it is also a geodetic point), a location at site S3 with obvious multipath errors, and a location at site S4, again with moderate multipath errors and additional sources of error, whose effects can only partially be resolved by data analysis. Variations of HDOP strongly influence the uncertainty. Average HDOP of experiment No. 2 was 1.24 while for experiment No. 3

Table 3. Statistical parameters of static measurements
Tabela 3. Statistične značilnosti statičnega določanja položaja

Exp. No.	Site	Receiver	Mode	No. of fixes	Absolute static uncertainty (m)
1	S2	R2	DGPS	7201	1.2
2	S3	R2	GPS	438855	4.5
3	S3	R2	GPS	1921488	3.4
4	S4	R3	GPS	3903	2.3
5	S4	R2	GPS	12148	2.1
6	S4	R2	DGPS	7739	1.7

it was 1.12. In the absence of loss of data due to cycle slips, the numbers of fixes is simply the product of measurement time (in seconds), and the data acquisition rate (number of fixes per second, 1 for R3 and 5 for R2).

Static positioning measurements

The measurements of static positioning at sites S2 and S3 are presented in Figure 2. Measurements were performed continuously for 5 consecutive days at S3 (Figure 2.a). Accuracy was determined as dRMS and was 2.96 m. The details of transformed angle/length ratio resolution are shown around a geodetic point, chosen as (0,0) position. The repeatability of observations at S2 with receiver R2 (DGPS) are shown in Figure 2.b. Measurements were performed over two days, separated by 42 days. Repeatability of positioning at points No. 2, No. 3 and No. 4 from the reference point (No. 1, with relative position 0 m) is shown. The relative experimental standard deviation of distances for points No. 2, No. 3, and No. 4 are 23 cm, 30 cm and 29 cm respectively, with a standard deviation of the reference point from its true position of 32 cm. It should be pointed out, that the large excursions of data in Figure 2.b do not represent settling times of the measurements, but real excursions of the instrument fixes from the points under consideration, caused by the movement of the experimenter from one point to another. The largest source of the uncertainties in this case are not the multipath errors, but the unfavourable position of the sites chosen (S2, S3), which have a reduced view of the satellites, not insuring optimal number of satellites in view. Data in Figure 2.b demonstrate that fixes, relative to a reference point, under unfavourable measuring conditions (obscuration of satellites) do not satisfy the accuracy requirements. However, even under such conditions the average accuracy of fixes is 8 cm from the requirement. These results cannot be directly compared to uncertainties presented in Table 3, as the relation between accuracy and uncertainty involves the variable HDOP.

Assesment of kinematic uncertainty

The results of assessment of kinematical uncertainty, relative to reference lines of 30.00 m and 41.30 m lengths, marked on the ground, are presented in Figure 3 and Figure 4 respectively. Measurements were performed by two receivers R1 and R2 on three different sites S1, S4 and S6. It can be observed from Figure 3 that in all cases

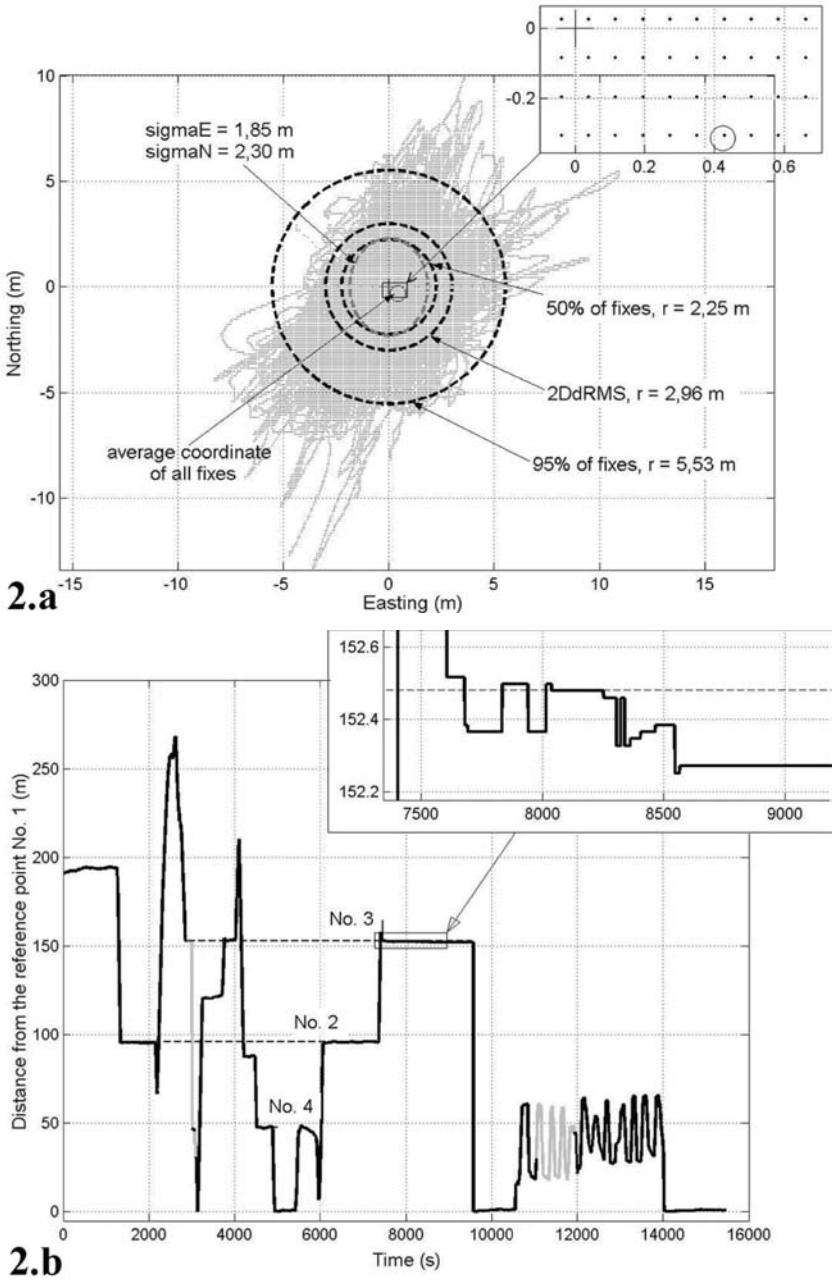

Figure 2. Results of static positioning at S3, centered with geodetic procedure (2.a) and repeatability of a distance from the reference point during fieldwork at S2 (2.b)

Slika 2. Rezultati določanja položaja točke na terenu S3, osredinjeni z geodetsko izmero (2.a) in ponovljivosti določanja razdalje do referenčne točke na terenu S2 (2.b)

Table 4. Statistical parameters of the 'line following' kinematical measurements on sites S1, S4 and on archaeological site S6
Tabela 4. Statistične značilnosti kinematičnih preizkusov sledenja ravni črti na terenih S1, S4 in arheološkem najdišču S6

Site	Conditions	Receiver	No. of fixes	No. of walks	Relative kinematical uncertainty (cm)
S1	Multipath	R1	3475	101	- 6 ± 317
S1	Multipath	R2	24551	132	5 ± 104
S4	higher HDOP	R2	10790	50	1 ± 41
S4	lower HDOP	R2	10755	50	1 ± 26
S4	moderate HDOP, DGPS	R2	6867	36	2 ± 29
S6	moderate HDOP	R2	6919	18	-15 ± 41

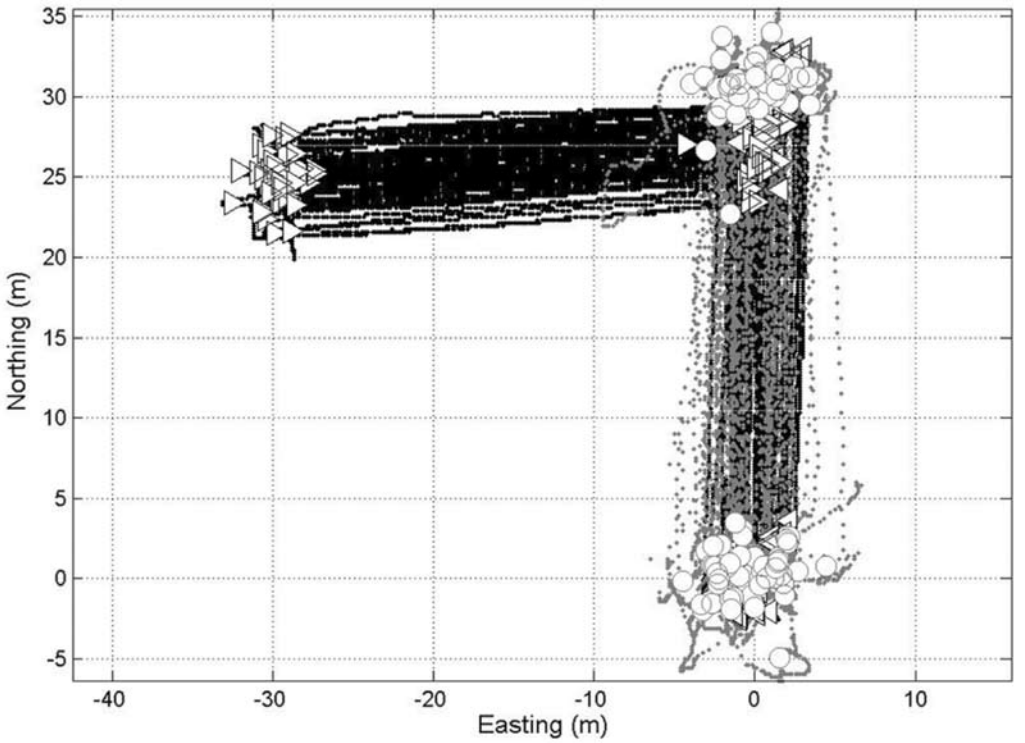

Figure 3. Fixes obtained by walking along a 30.0 m line on Site 1 with two receivers (R1 grey, R2 black). Extreme positions after two minutes of measurements are marked with circles (R1) and triangles (R2).
Slika 3. Sledi hoje ob ravni črti, dolgi 30,0 m na terenu S1 z dvema različnima sprejemnikoma (R1 siva, R2 črna). Srednje vrednosti odčitkov, zabeleženih ob dvominutnih stanjih na skrajnih točkah so označene s krogi (R1) in trikotniki (R2).

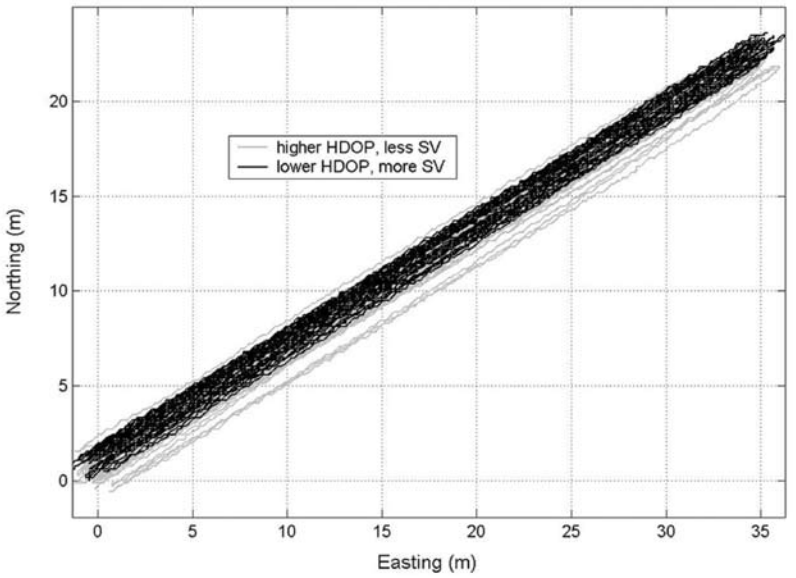

Figure 4. Fixes obtained by walking along a 41.3 m line on Site 4 with receiver R2 in two experiments, each under different conditions. The receiver was held on for up to 20 seconds only in extreme positions.
Slika 4. Zabeleženi dve sledi hoje z istim sprejemnikom (R2) ob ravni črti, dolgi 41,3 m na terenu S4 v različnih pogojih opazovanja. Stanja na skrajnih točkah niso presegala 20 s.

the worst case absolute accuracy of the following of the lines by receiver R2 is 2.50 m. However, the measured trajectories are highly parallel to the reference lines, resulting in a up to 40 cm relative accuracy in positioning, taking one of the end points of the lines as the reference point. This experiment demonstrates the considerable difference between the absolute and the relative positioning accuracies and indicates the necessity of taking the reference point positions into account in determining the fixes in the field. Obviously, in this way it is also possible to correct and improve the absolute accuracy of the positioning. The overall accuracy is then determined by the relative accuracy of the kinematical data and the absolute accuracies of the reference point fixes. As the distribution of uncertainty of fixes also incorporates the highly variable HDOP values, the width of the distribution does not reflect the accuracy that can be obtained under more favourable conditions. Even within low multipath conditions, as on site S4, changes of HDOP exert considerable influence on accuracy (Figure 4). A distribution of fixes for the determination of the uncertainty of all kinematical results from site S4 is shown on the Figure 5. The improvement of accuracy due to the smaller multipath errors is negligible with the DGPS technique. The numerical values of statistical parameters are given in Table 4.

Test on followed trajectories

The persistence of straightness and shape of the followed trajectory was tested on Site

S1 with instruments R1 and R2. Results were collected without use of the DGPS. In the absence of known geodetic points a direct transformation from degrees into meters was performed, the two orthogonal coefficients being obtained from a comparison of the physical distance of the 30.0 m line and the mean distance of position outputs on the line edges. The results are presented in Figure 6. Figure 6.a demonstrates the effects of stopping at each of the 6 reference points for two minutes. The excursions of fixes are due to changing measuring conditions. A continuous scan (without stopping) shows a qualitatively different result (Figure 6.b: the straightness of parallel lines of the trajectory is demonstrated, with a shift error occurring only during the two minutes stop between scans.

A test somewhat similar to the one described above, using R2 attached to an instrument with a different function, but in realistic field conditions (Site S2), is shown in Figure 7. The surveyor followed straight lines, parallel to each other and displaced by 50 cm, to scan the whole area of the field. As the GPS antenna was not mounted in the middle of the carrier instrument (see Figure 8, equidistance between lines was not expected.

Figure 9 shows the results of a kinematical GPS scan at the archeological site S5, compared to data obtained from a TPS scan. The GPS antenna and geodetic prism (fixed as on Figure 8) both simultaneously traveled the same route. The GPS results were transformed into the D48 system. A

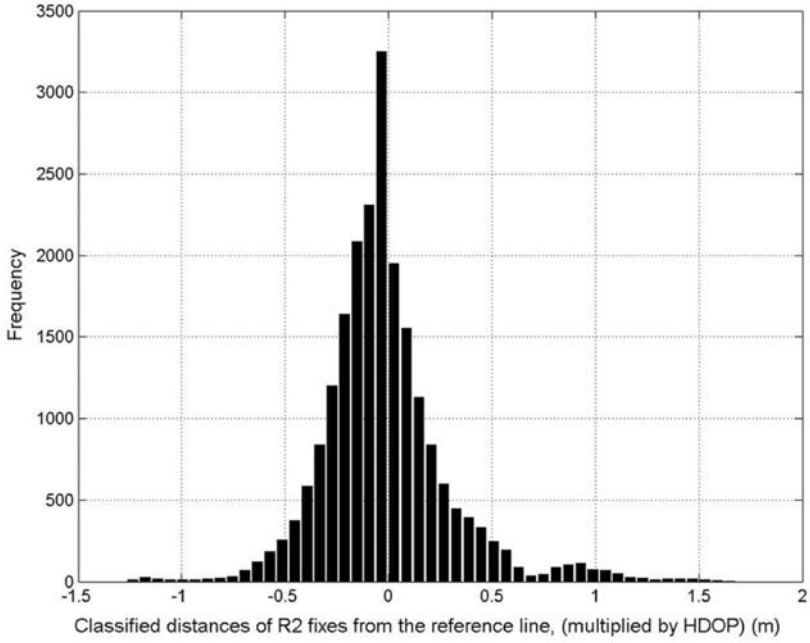

Figure 5. A distribution of fixes for the determination of the uncertainty of all kinematical results from site S4.
Slika 5. Porazdelitev odčitkov za določitev negotovosti vseh kinematičnih preizkusov na terenu S4.

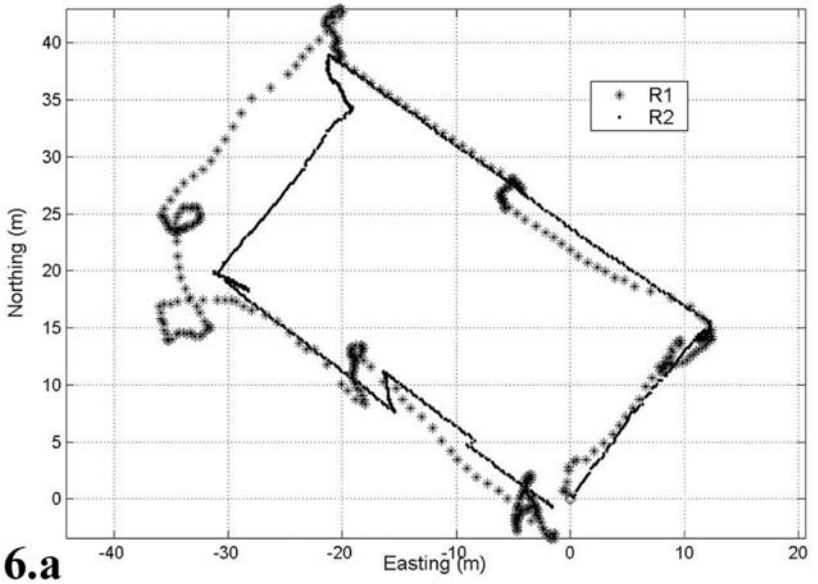

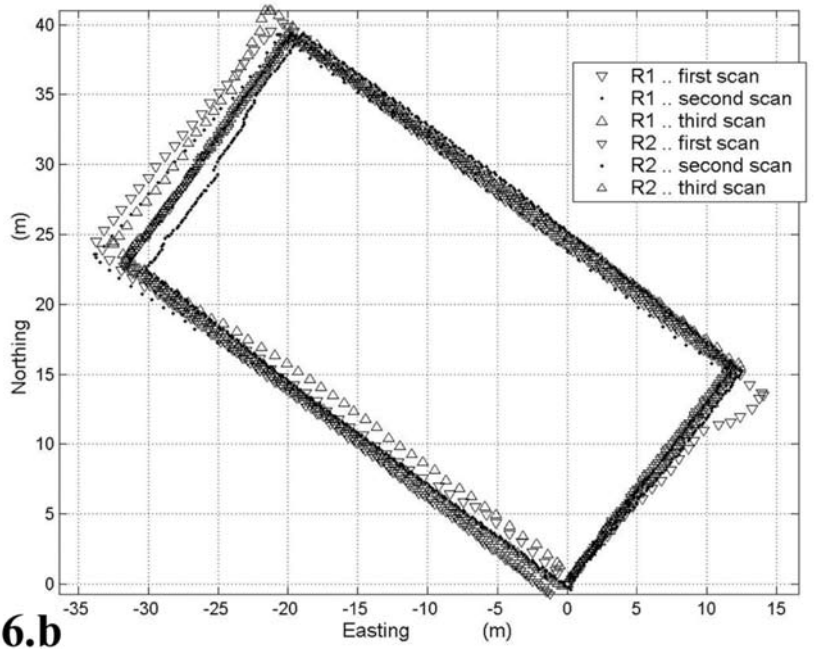

Figure 6. The starting point of scans is at coordinates (0, 0). The transformation parameters are the same for figures 6.a and 6.b. Scan around the sports field with two minute stops at reference points (6.a) and scan without stops (6.b).
Slika 6. Začetna točka sledi je premaknjena v (0,0). Transformacijski parametri so enaki na slikah 6.a in 6.b. Sled hoje okoli športnega igrišča z dvominutnimi postanki na ogliščih (6.a) in sledi, dobljene s hojo brez postankov (6.b).

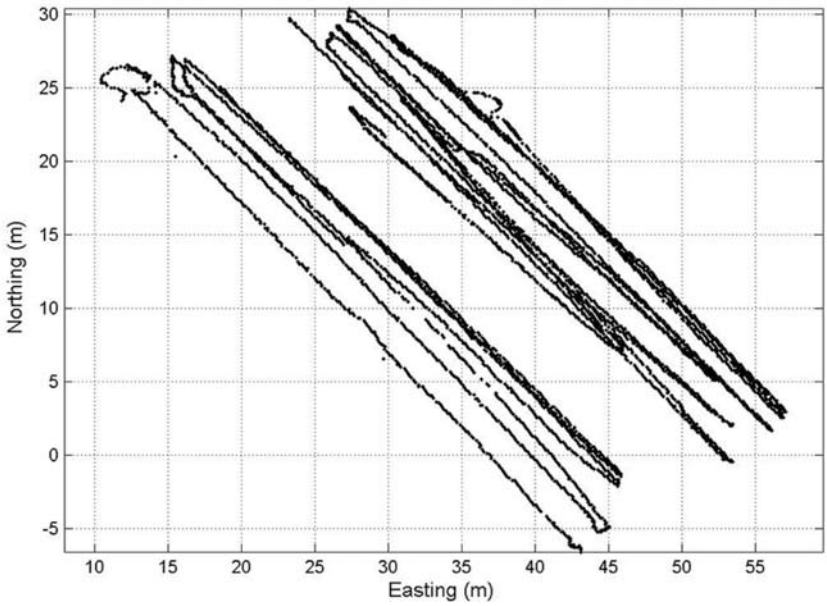

Figure 7. Following profiles with R2 in DGPS mode
Slika 7. Sledenje profilom z R2 v načinu DGPS

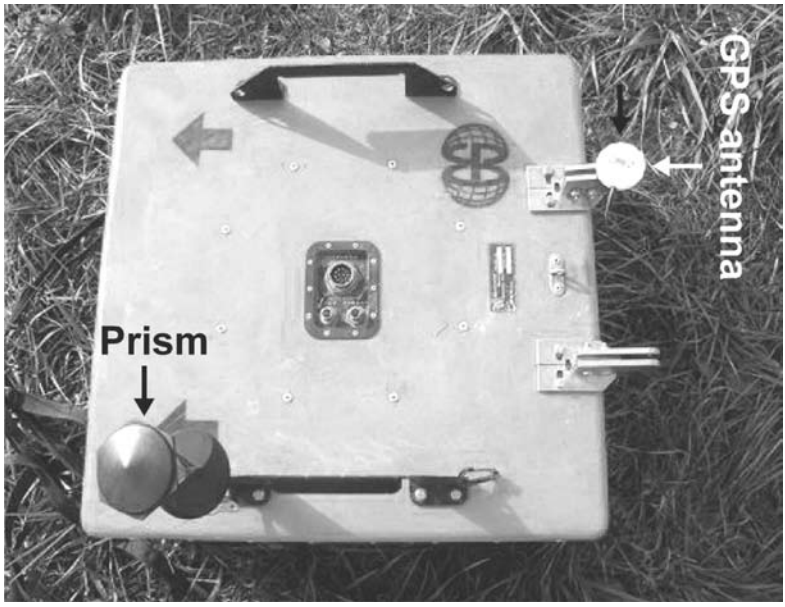

Figure 8. Positions of GPS antenna and geodetic prism for the use of TPS on the top of a 200 MHz GPR antenna
Slika 8. Namestitev antene GPS in geodetske prizme za uporabo TPS na pokrovu 200 MHz antene GPR

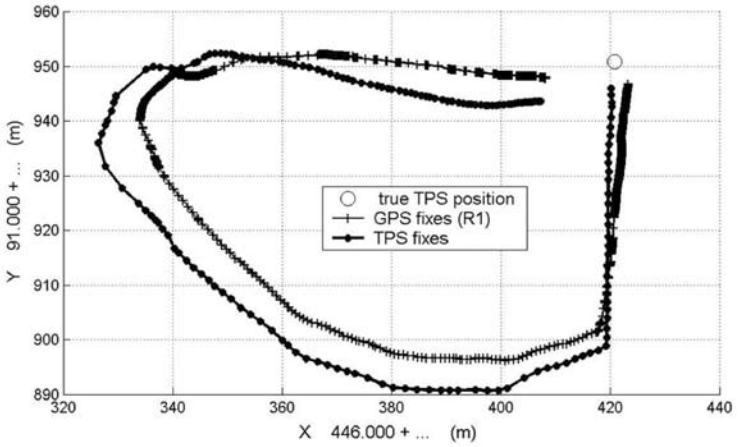

Figure 9. Comparison of R1 and TPS fixes, taken simultaneously on the same route

Slika 9. Primerjava sledi drsenja, zabeleženih sočasno s sprejemnikom R1 in TPS

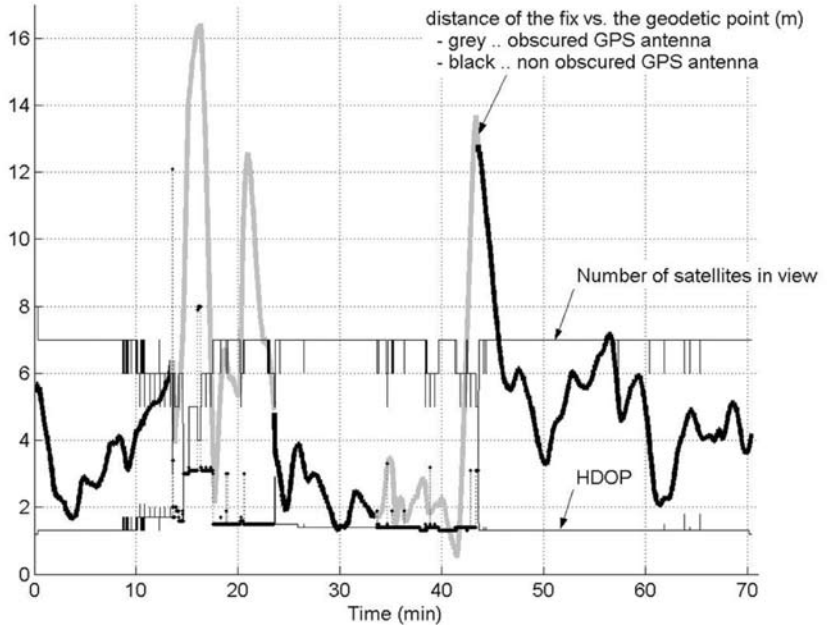

Figure 10. Static positioning with obscured antenna: how a distance from geodetic point apparently changes over time. According to the obscuring signals of less satellites are capable to reach the GPS antenna and thus HDOP and consequently the deviations arise.

Slika 10. Določanje položaja z zastrto anteno GPS: razdalja do geodetske točke se je sčasoma navidez spreminjala. Zastrto anteno dosežejo signali manjšega števila satelitov, zaradi česar se HDOP in posledično odstopanje od geodetske točke povečata.

significant displacement of the GPS fixes (up to 8 m) from the TPS trace can be observed. Also the GPS scan data do not return to the starting point after the completion of the scan. The data demonstrate that careful analysis of the GPS data is required in real situations when trajectories across the field are of a general shape (not straight lines or other favourable shapes).

Static positioning test with obscured antenna

As the obscuration of one or several satellites during measurements severely degrades the accuracy of the fixes, we attempted to quantify this by deliberately obscuring the satellites for certain time periods. To evaluate the obscuration effects on static accuracy of R2, the antenna was covered by a metal, dual-shell lid. The results are shown in Figure 10: the solid bold line represents the measured distance from a geodetic point under conditions of obscuration. It can be observed that during the obscuration (at times 13 min, 23 min, 33 min, and 43 min) the accuracy of positioning is decreased by an order of magnitude, but obscuration does not cause complete loss of data. However, as expected, obscuration in the multipath conditions leads to unpredictable behavior of the positioning system and should be avoided if possible.

The applicability of GPS system for GPR survey

The applicability of the GPS system in the GPR survey of Antique cities was tested on the archaeological site at Tanagra (Greece) (see: Bintliff et al., 2000, 2002; Bilc, 2003; Mušič et al., 2004) within the framework of geophysical survey in the Boeotia Project (http://www.nia.gr/Pharos13.htm). The starting-point of the test measurements was the recognition of archaeological features defined on aerial photographs and magnetograms by directing GPR profiles in the required direction. This information is important for the definition of the priorities of systematic geophysical survey with application of multi-method approach (see: Mušič & Horvat, 2007). GPR profiles in selected directions are a rapid means to provide data on the depth and degree of preservation of architectural remains to complement the results of geophysical mapping with resistivity and magnetic methods. Two profiles with control points in UTM projection (see Bilc, 2003) were chosen for the test measurements (Figure 11 and 12).

The trial survey in GPR profiles was undertaken using a 200 MHz antenna. This made it possible for us to register both information on the archaeological architectural remains found at a shallow depth below the surface, and changes in the basic geology at a somewhat greater depth. This 200 MHZ GPR antenna is therefore suitable for survey, because of the appropriate ratio between resolution and attainable depth. It also has a solid construction, which guarantees sufficient antenna mobility during measurement, as well as its stability in the direction of movement. This greatly reduces background noise. Prior to the identification and classification of the echoes in categories, the GPR profiles were processed according to the following procedure (for explanation see e.g.: Conyers at al. 1997): *Background removal* (Removal of horizontal banding), *Range gain* (Recovery of lower amplitude information), *IIR – Filter* (Smoothing operators for noise

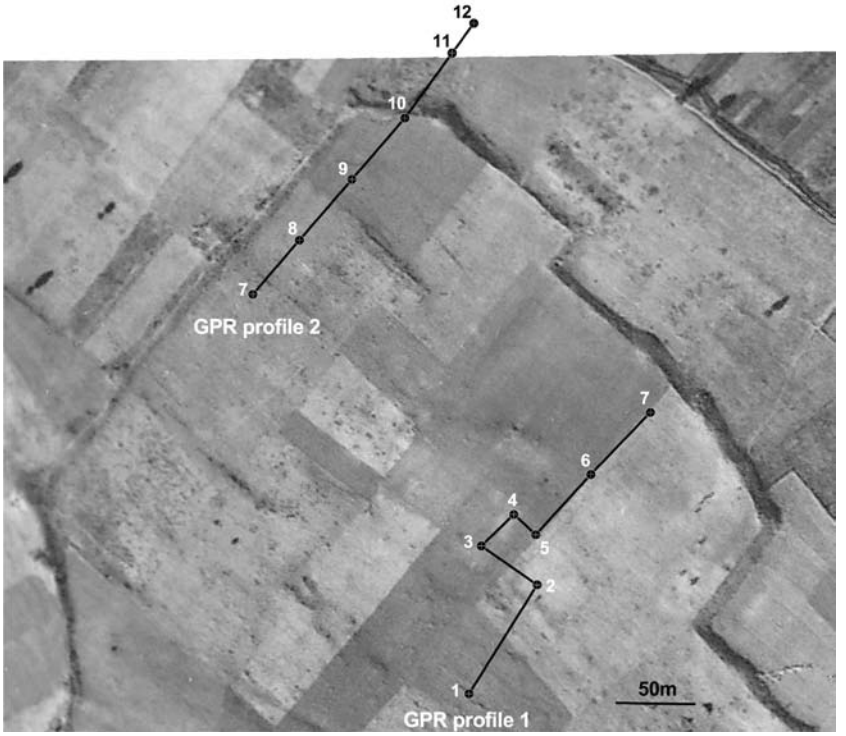

Figure 11. The northern part of Tanagra on a vertical aerial photograph (Royal Air Force, 26. Oct. 1943. Courtesy of British School in Athens) with the selected GPR profiles 1 and 2 and the control points in the direction of the profiles in the UTM system (1-12)
Slika 11. Severni del Tanagre na vertikalnem aeroposnetku (Royal Air Force, 26. Oct. 1943, z dovoljenjem britanske šole v Atenah) z izbranima GPR profiloma 1 in 2 in kontrolnimi točkami v smeri profilov v UTM sistemu (1-12)

reduction), *Migration* (Removing diffractions and correcting dipping reflectors to their true position), *Surface normalisation* (Correcting topographic position of reflectors on variable surface morphology).

It is necessary to select an appropriate standard for the marking of archaeologically significant echoes, when the single 2D GPR profiles are interpreted. Only the most typical GPR echoes that are characteristic for archaeological architectural remains are marked on the radargram (Figure 13.a). Control over the interpreted echoes and the ease of understanding of the results is established by classification of the echoes in selected, typologically defined categories. The most suitable for this purpose is the division of the echoes into 14 classes, which are precisely defined by B. BEVAN (1996, fig. B116) (Figures 13.a and 14).

The greatest deviation in the GPS measurement from the direction of the movement of the GPR antenna was determined

at points 3, 4 and 5 (Figure 14), which was a result of a a sharp change in the direction of movement of the antenna at an angle to an approximate right angle. The deviations are in accordance with the established aims of the research on the level areas and correspond to the deviations, which were determined in GPR profile 2, where there was no greater change in the direction of movement. Figures 11, 14 and 15 indicate that at each change in direction the GPS measurements »returned to the right« place, but some time nevertheless passes before this happens. If the direction of movement changes too frequently and time is not taken for the GPS readings to settle down, then these errors accumulate. The deviation in the direction of movement in fourth loop in trial GPR profile 1 already amounted to almost 2 m (Figures 14.b and 15). The GPS fixes »settled down« according to the reference lines after circa 35 meters of linear movement (see the segment from point No. 3 to No. 2).

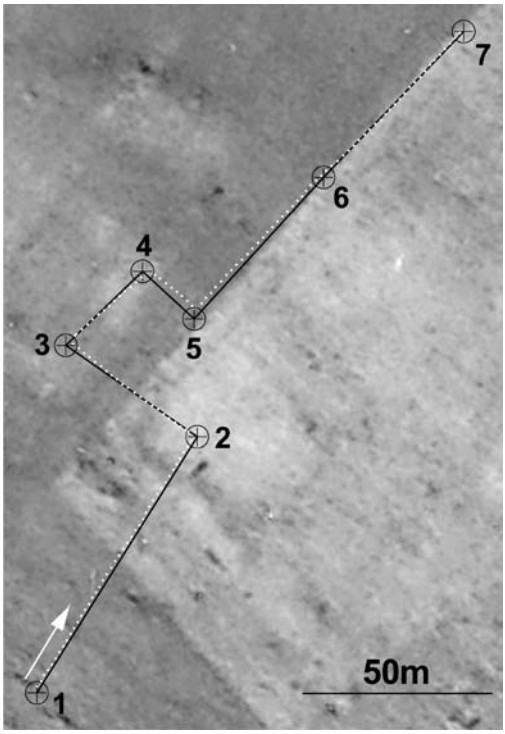

Figure 12. The GPS readings at a distance of 2 m are indicated by the white points in the direction of GPR profile 1
Slika 12. Z belimi točkami v smeri GPR profila 1 so prikazani GPS v razdalji 2 m

GPR profile 2 runs in a straight line, crosses the town wall and descends via a steep slope on the exterior of the wall at a height of 113 metres above sea level (from 122 m down to 109 m). A deviation (in the horizontal plane: average of fixes including HDOP according to the reference lines between reference points is 44 cm while 95 % of fixes lie closer than or equal to 55 cm to the reference lines) from the actual direction of movement in the particular case of linear movement due to the rapid change in height (z) was determined in this profile.

On the basis of these results it is possible to conclude that the precision of this GPS system only meets our requirements completely in the specific case of linear movement. Effective use requires the selection of a direction of movement with the least possible number of changes in direction at a greater angle. This problem can be solved by planning the prospection in long, relatively straight traverses.

The estimation of the accuracy of the location of the GPR echoes by the GPS system was also correlated in relation to the location of the magnetic anomalies, mapped by the Geometrics G-858 magnetometer (see Mušič et al., 2004), which had been georeferenced by TS measurements, using a

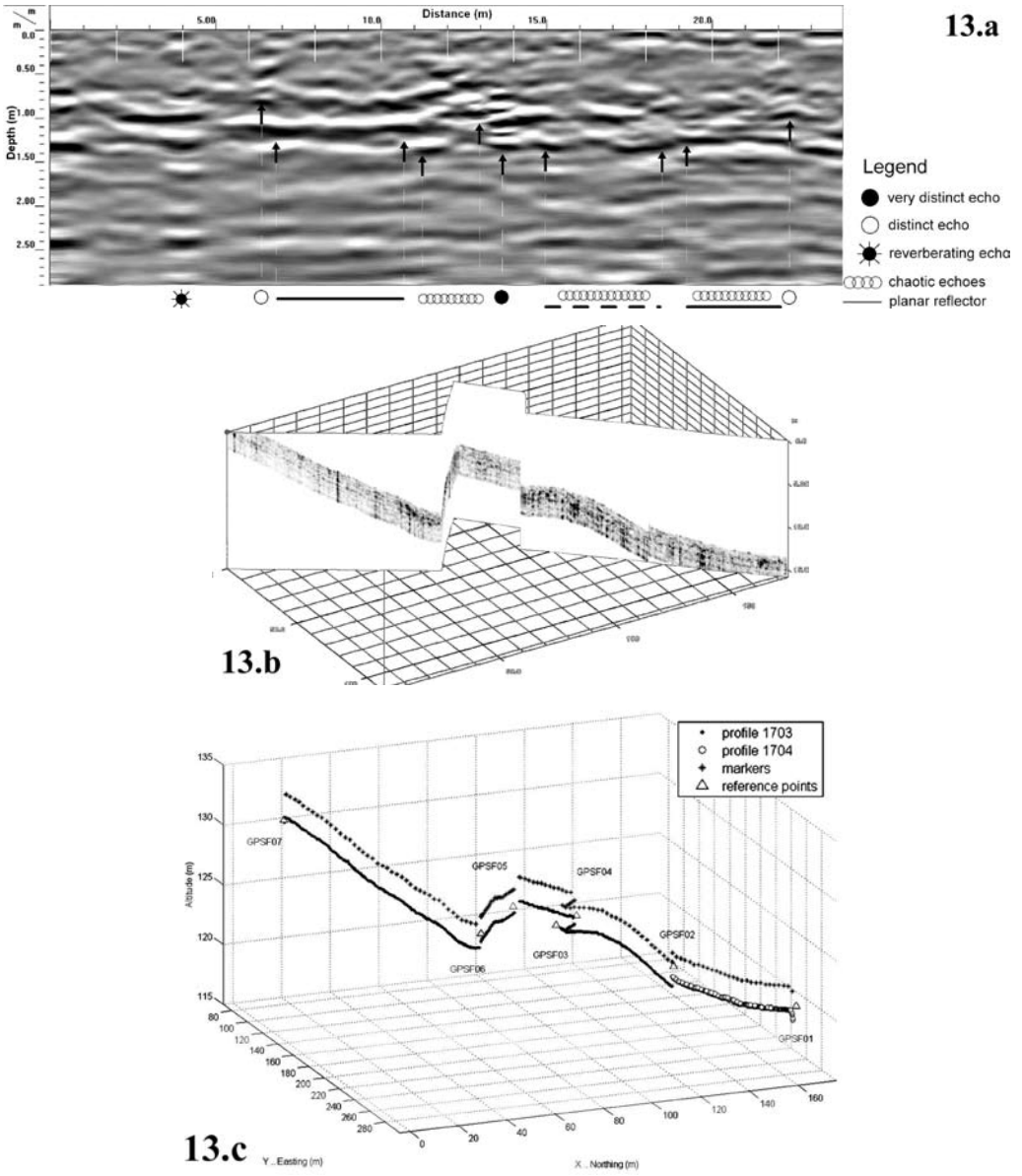

Figure 13. Detail of the filtered GPR profile in the direction of GPR profile 1 (13.a) with the arrangement of the GPR echoes in categories (BEVAN, 1997) and the 3D representation of the radargram with topographic correction in the direction of GPR profile 1 (13.b) accompanied with the GPS observation of the profile route (13.c)

Slika 13. Detajl filtriranega georadarskega profila v smeri GPR profila 1 (13.a) in tridimenzionalna predstavitev radarskega diagrama s topografsko korekcijo po smeri profila 1 GPR (13.b), izdelano po zebeleženi sledi opazovanja z GPS na isti poti (13.c)

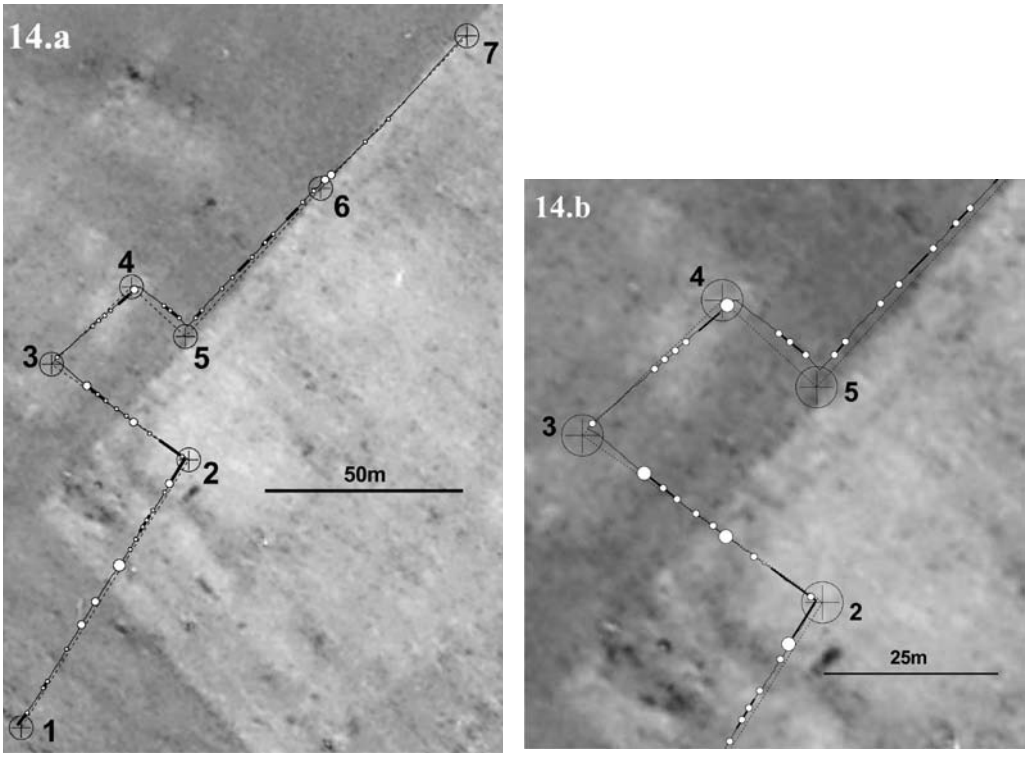

Figure 14. The significant GPR echoes are classified in the two basic categories: small and distinct echoes and long echo pattern found along a traverse (Bevan, 1996) in the direction of GPR profile 1 (14.a) and a detail of the same profile (14.b)
Slika 14. Značilni georadarski odboji so razvrščeni v dve osnovni kategoriji: majhni in izraziti odbji in dolge sledi vzdolž profilov (Bevan, 1996) v smeri GPR profila 1 (14.a) in detajl istega profila (14.b).

reference point in UTM projection (Bilc, 2003). The magnetogram (Figure 15) shows the streets of Ancient Tanagra, the building blocks and the division of space within the blocks. GPR profile 1 was, thus, located in the area, where it was reasonable to expect numerous GPR echoes from various types of architectural remains. The results of the magnetic method led us in general to expect marked individual echoes from walls (distinct echoes-small and compact echoes) and echoes from horizontal reflectors or roads (planar reflectors-long echo pattern found along a traverse). Figure 15 shows that the entire survey process with the GPR/GPS system, in accordance with the method of GPR profile evaluation explained above, was successful in terms of rapid assessment of archaeological potential. By planning surveys in radial or parallel located linear traverses, it is possible to avoid errors in defining the position of GPR echoes from GPS measurements, which are the result of frequent changes in direction. These are visible on Figure 15 between fixed points 5 and 6. It is possible to conclude from this test that such a GPR/GPS system is useful for the rapid evalu-

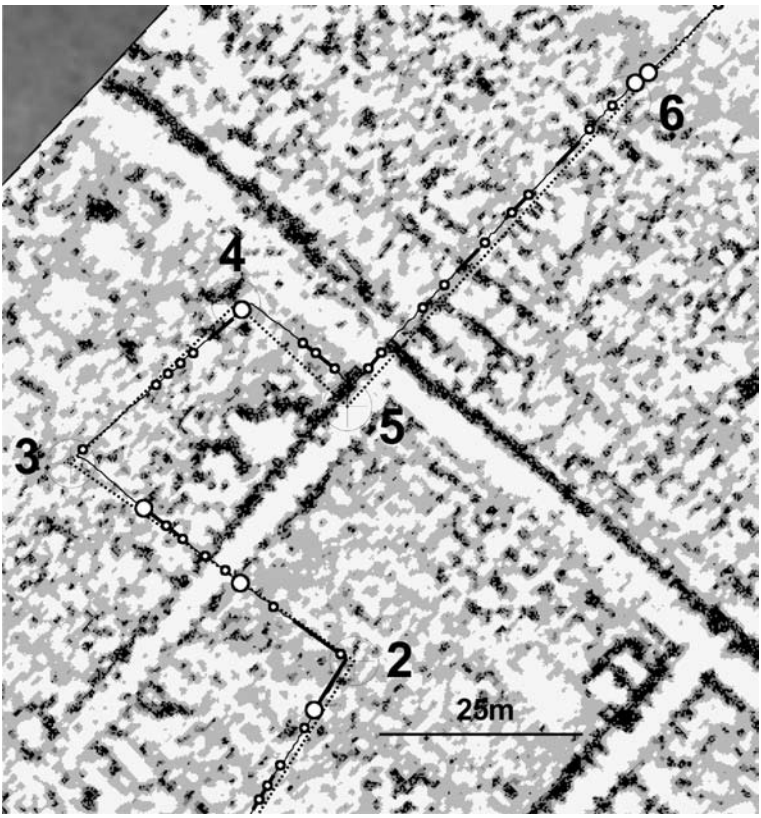

Figure 15. Detail of the magnetogram with the interpretation of GPR profile 1
Slika 15. Detajl magnetograma z interpretacijo GPR profila 1

ation of the degree of preservation of architectural remains, the extent of sites, as well as for geological mapping etc. It is especially useful where fieldwork is subject to temporal constraints and effective prospection urgently requires autonomy in the operation of the geophysical team.

CONCLUSIONS

As expected, according to the use of (L1) carrier wave, we were able to obtain a positioning resolution up to one wavelength (19 cm, see Figure 2.a). This resolution is better than our initial goal, i.e. 30 cm relative uncertainty of positioning, however, the desired 30 cm uncertainty could only be achieved under favourable conditions (ODIJK, 2002). In order to extend the positioning capabilities of the type of equipment used to less favourable conditions, further post-processing, especially concerning the influence and reduction of multipath errors is necessary (CANNON et al., 1993). Under conditions where a degradation of the GPS fixes occured during the scans, we were able to compensate for this and to refine the positioning results by taking the real-time radio link or archived

fixes from the nearest reference station into account. As described in the literature (Van Sickle, 2001; Saka et al., 2004), a dual frequency receiver enables faster real time kinematical positioning than single frequency receiver, eliminating some of the multipath and receiver noise errors. In order to describe positioning conditions the processing of the carrier phase (CP), based on smoothing the pseudo ranges, should also be considered (Ford, 2003). The techniques described are not adequate for archaeological work in extreme conditions, e.g. underground caves or urban environments, where navigation satellite signals are obscured from the receiver. A hybrid positioning technology, involving relative positioning by wideband carrier waves or by some other types of sensors (Mezentsev et al., 2004) would be recommended in such circumstances. It is now well known that many of the positioning problems investigated in our work will be solved by better basic accuracy in new satellite positioning technologies, based on a new satellite network that is now under the new satellite networks that are now under construction (Galileo, GLONASS, CNSS, GAGAN). As the new system still seems to be several years from becoming operational, the necessary experience in the geophysical fieldwork using satellite positioning can be obtained by utilizing the existing, though barely adequate GPS system. Nevertheless, the vulnerability of the satellite navigation systems due to intentioned jamming and the rate of errors due to the observation conditions, lead to the implementation of a complementary sensor.

Acknowledgments

The authors express their gratitude to Messrs. Andrej Bilban (Geoservis, Ljubljana), Guido Lenz (FSL Deutschland, Germany), Duško Vranac (Harphasea, Koper) for the discussions and help with the equipment selection and use.

Povzetek

Uporaba enofrekvenčnega sprejemnika GNSS s 30 cm negotovostjo v kinematičnem načinu dela za terenske geofizikalne preiskave

Zamisel o izdelavi cenenega, enofrekvenčnega GPS sistema, ki je preprost za upravljanje izhaja iz potrebe po večji fleksibilnosti in učinkovitosti terenskega dela pri geofizikalnih raziskavah. Zadostno fleksibilnost zagotavlja le popolna avtonomija ekipe pri načrtovanju in izvajanju terenskih postopkov pri natančnem prostorskem umeščanju ugotovljenih anomalnih območij.

Uveljavljeni geodetski terenski postopki, tudi s pomočjo satelitske navigacijske tehnike, so pogosto dolgotrajni, cenovno predragi in za našo rabo pogosto tudi preveč natančni. Z žrtvovanjem visoke natančnosti bi skrajšali čas pridobivanja dovolj zanesljivih podatkov o položaju merilnih instrumentov z uporabo enofrekvenčnih (L1) sprejemnikov GPS srednjega razreda.

Preizkusni tereni obravnavani v članku so enaki realnim situacijam in imajo napake določanja položaja s satelitskim sistemom enake vzroke: zastrtost, večpotje, spremenljivost ionosfere. Vplivov spremenljivosti ionosfere na rezultate v predstavljenih primerih še nismo opazovali.

V pogojih večpotja je raztros rezultatov (Slika 2a), izmerjen s preprosto GPS anteno (glej sliki 1 in 8), pričakovano prevelik. Pri geofizikalnih raziskavah je pomembna tudi zanesljiva ponovljivost določanja položaja, kadar je potrebno meritve ponoviti pri drugačnih nastavitvah geofizikalnega instrumenta ipd. Z določanjem razdalje do referenčne točke s statičnimi preizkusi (Slika 2b) smo dokazali, da je v dobrih pogojih oz. pri majhni zastrtosti satelitov, ponovljivost rezultatov položaja ustrezna. V tabeli 3 vidimo, da imajo na negotovost meritev pričakovano večji vpliv okoliščine in izbira sprejemnika kot način opazovanja (samostojni GPS, diferencialni - DGPS). Vpliv izbire naprave na rezultate kinematičnih preizkusov je razviden iz tabele 4: v enakih pogojih je negotovost precej manjša, v pogojih z malo večpotja je negotovost ustrezna. Sliki 3 in 4 prikazujeta rezultate z dveh terenov: v pogojih nezanemarljivega večpotja smo preizkušali različna sprejemnika (Slika 3), ob različnih razporeditvah satelitov nad obzorjem (HDOP) smo na terenu z malo večpotja in zastrtosti preizkušali isti sprejemnik. Ponovljivost oblike sledi smo v različnih režimih hoje opazovali v enakih pogojih večpotja (Slika 6a in 6b). Sledenje ravnim profilom ob znatnem večpotju je razvidno s slike 7. Sočasno določanje položaja s sprejemnikom GPS in teodolitom (TPS) na sliki 9 kaže odstopanja, pričakovana v slabših pogojih sprejema. Namerno zastiranje mirujoče antene GPS (Slika 10) povzroča velika nihanja rezultatov položaja oziroma navidezne premike. Na arheološkem terenu (Slika 11) smo zaznali odstopanja od referenčne črte, ki so naključno (glej Slika 5) naraščala z oddaljevanjem od oglišča, v katerem smo začeli hojo. Z določitvijo parametrov odstopanja ob upoštevanju vpliva HDOP in kvantitativne ocene večpotja na določenem terenu, je odstopanja možno kompenzirati.

Testno rekognosciranje v georadarskih profilih smo izvajali z 200 MHz anteno, s katero poleg informacij o arheoloških arhitekturnih ostalinah, ki se nahajajo plitvo pod površjem, registriramo tudi spremembe v geološki podlagi na nekoliko večjih globinah. Ta GPR antena je ustrezna za rekognosciranje zaradi ustreznega razmerja med ločljivostjo in globino dosega ter masivne konstrukcije, ki ob zadostni mobilnosti antene med meritvami zagotavljajo tudi njeno stabilnost v smeri gibanja, kar bistveno zmanjšuje šum.

Največja odstopanja GPS meritev od smeri gibanja GPR antene so bila ugotovljena v točkah 3, 4 in 5 (glej sliki 14b in 15), kjer smo naglo spreminjali smer gibanja antene, dejanske spremembe smeri so približno ustrezale pravemu kotu. Na ravnih odsekih so odstopanja v skladu z zastavljenimi cilji raziskave in ustrezajo odstopanjem, ki so bila ugotovljena v GPR profilu 2, kjer večjih sprememb v smeri gibanja ni bilo. Na istih slikah vidimo, da se pri vsaki spremembi smeri odčitki GPS »vrnejo na pravo« mesto vendar vmes vselej preteče nekaj časa. Če smer gibanja spreminjamo pogosto in ne počakamo, da se odčitki GPS ustalijo, se te napake akumulirajo. Na

osnovi te ugotovitve lahko zaključimo, da natančnost tega GPS sistema popolnoma odgovarja našim zahtevam samo v posebnem primeru premočrtnega gibanja. Za učinkovito rabo moramo izbirati smeri gibanja z najmanjšim možnim številom sprememb smeri pod večjimi koti. Ta problem rešimo tako, da prospekcijo načrtujemo v dolgih, približno ravnih prečnicah.

Oceno natančnosti pozicioniranja georadarskih odbojev z GPS smo preverjali tudi v odnosu do položaja magnetnih anomalij, kartiranih z magnetometrom Geometrics G-858 (Mušič et al., 2004), ki so bile georeferencirane z zemeljskimi meritvami z uporabo referenčnih točk v UTM projekciji (Bilc, 2003). Na magnetogramu (slika 15a) vidimo ulice antične Tanagre, stavbne bloke in razdelitve prostorov znotraj blokov. GPR profil 1 je bil torej izbran na območju, kjer smo lahko pričakovali številne radarske odboje od različnih tipov arhitekturnih ostalin. Glede na rezultate magnetne metode smo v splošnem pričakovali izrazite posamične odboje od zidov in odboje od horizontalnih reflektorjev oziroma cest. Iz slike 15 je razvidno, da je celoten postopek rekognosciranja z GPR/GPS sistemom v skladu z obrazloženim načinom vrednotenja radarskih profilov učinkovit v smislu hitre ocene arheološkega potenciala. Z načrtovanjem pregledov v radialno oziroma vzporedno zastavljenih ravnih prečnicah se izognemo napakam v določanju položaja radarskih odbojev iz opazovanj z GPS, ki so posledica pogostega spreminjanja smeri in so vidne na sliki 15 med točkama 5 in 6.

Iz rezultatov statičnih in kinematičnih primerjalnih preizkusov različnih vrst preprostejših sprejemnikov GPS vidimo, da imajo preprostejše naprave pričakovano širši interval zaupanja. Kakovost obdelave satelitskih signalov namreč v večji meri zagotavljajo zmogljivejša elektronska vezja.

Možnost kompenziranja napak z naknadno obdelavo izmerjenih odčitkov sprejemnikov GPS obstaja, če zadosti dobro poznamo vzroke napak oziroma pogoje, v katerih izvajamo terenske raziskave. Pričakovanja od novih sistemov satelitske navigacije (Galileo - Evropa, GLONASS - Rusija, CNSS - Kitajska, GAGAN - Indija) in posodobitve obstoječega (GPS - ZDA) so zaradi raznih nedorečenosti še v domeni prihodnosti. Dva splošna pojava zmanjšujeta zanesljivost določanja položaja satelitskih navigacijskih sistemov: že omenjene napake zaradi okoliščin na terenu in neodpornost na namerno radiofrekvenčno motenje (*jamming*). Eden od ustreznih odgovorov za zagotovitev zahtevane zanesljivosti GPS meritev z enofrekvenčnim sprejemnikom je vključevanje dodatnih komplementarnih senzorjev (npr. pospeškometer pri kinematičnih meritvah) v odvisnosti od narave motenj.

REFERENCES

BERAN, T., LANGLEY, R. B., BISNATH, S. B. & SERRANO, L. (2007): High-Accuracy Point Positioning With Low-Cost Receivers. *Navigation, Journal of The Institute of Navigation*.; Vol. 54, No. 1, pp. 53-63.

BEVAN, B. (1996): *Geophysical exploration for Archaeology. Volume B: Introduction to geophysical exploration.* Geosight Technical Report Number 4.

BILC, A. (2003): *Tanagra 2003, Report on groundwork for use of GPS measurements.*

BINTLIFF, J. L., EVELPIDOU, N., FARINETTI, E., MUŠIČ, B. & SLAPŠAK, B. (2002): The Tanagra survey. Report on the 2001 season. *Pharos*.; Vol. 9, pp. 33-74.

BINTLIFF, J. L., FARINETTI, E., SBONIAS, K., SIGALOS, L., SLAPŠAK, B. & MUŠIČ, B. (2000): The Tanagra survey. Report on the 2000 season. *Pharos*.; Vol. 8, pp. 93-128.

CANNON, M. E., LACHAPELLE, G. & LU, G. (1993): Kinematic Ambiguity Resolution With a High Precision C/A Code Receiver. *Journal of Surveying Engineering, Amer. Soc. Civil Eng*.; Vol. 119, No. 4, pp 147- 155.

CONYERS, L. B. & GOODMAN, D. (1997): *Ground-Penetrating Radar. An introduction for archaeologists*. Altamira Press. A division of Sage Publications, Ins.

DE JONG, C.D. & LACHAPELLE, G. (2001): *Hydrography, 2nd edition*. Series on mathematical geodesy and positioning. Delft University Press: Blue Print, Delft.

FORD, T. (2003): A New Positioning Filter: Phase Smoothing in the Position Domain, Navigation. *Journal of The Institute of Navigation*.; Vol. 50, No. 2, pp. 65-78.

GAFFNEY, C. & GATTER, J. (2003): *Revealing The Buried Past: Geophysics for Archaeologists*. Tempus Publishing Ltd.

GPS Position Accuracy Measures, Application note, APN-029 Rev 1, Novatel. (www.novatel.com).

International Vocabulary of Basic and General Terms in Metrology. USM, Ljubljana, 1999.

LACHAPELLE, G., HENRIKSEN, J. & MELGAERD, T. (1994): Seasonal Effect of Tree Foliage on GPS Signal Availability and Multipath for Vehicular Navigation. *Proceedings of GPS-94 (Salt Lake City, September 21-23)*. The Institute of Navigation, Alexandria, VA, pp. 527-532.

MEZENTSEV, O., COLLIN, J., KUUSNIEMI, H. & LACHAPELLE, G. (2004): Accuracy Assessment of a High Sensitivity GPS Based Pedestrian Navigation System Aided by Low-Cost Sensors. *11th Saint Petersburg International Conference on Integrated Navigation Systems*. May 24-26, Saint Petersburg, Russia, pp. 156-164.

Mušič, B., Slapšak, B. & Farinetti, E. (2004): Ancient Tanagra (Grimadha): *Geophysical prospection and modelling for understanding of urban plan and on-site activity areas*. In: Fischer Auesserer K. (ed.). [Enter the past] : the e-way into the four dimensions of cultural heritage : proceedings of the 30th conference, 2003, (BAR international series). Oxford: Archaeopress, pp. 317-320.

Mušič, B. & Horvat, J. (2007): Nauportus – an early Roman trading post at Dolge njive in Vrhnika. The results of geophysical prospection using a variety of independent methods. *Arheol. Vest.*; Vol. 58, pp. 219-283.

Mušič, B., Horvat, J. & Dimc, F. (2008): Comparison of different geophysical techniques in relation to archaeological data for settlement reconstruction – the case study of Nauportus, Slovenia. *Cultural Heritage and New Technologies*. Workshop 12 – Archäeologie und Computer. November 5. – 7. 2007, Vienna City Hall. – in print.

Odijk, D. (2002): *Fast precise GPS positioning in the presence of ionospheric delays: PhD thesis.* Delft University.

Saka, M. H., Kavzoglu, T., Ozsamli, C. & Alkan, R. M. (2004): Sub-Metre Accuracy for Stand Alone GPS Positioning in Hydrographic Surveying. *The Journal of Navigation*.; Vol. 57, No. 1, pp. 135-144.

Van Sickle, J. (2001): *GPS for Land Surveyors*. Taylor and Francis, New York.

Wang, C. & Lachapelle, G. (2002): GPS Attitude Determination Reliability Performance Improvement Using Low Cost Receivers. *Journal of Global Positioning Systems*.; Vol. 1, No. 2, pp. 85-95.

The possibility of using homogeneous (projective) coordinates in 2D measurement exercises

Možnost uporabe homogenih (projektivnih) koordinat v dvodimenzionalnih merskih nalogah

Aleksandar Ganić[1], Milivoj Vulić[2], Franc Runovc[2], Tina Habe[3]

[1]University of Belgrade, Faculty of Mining and Geology, Đušina 7, 11000 Belgrade, Serbia: E-mail: aganic@rgf.bg.ac.yu
[2]University of Ljubljana, Faculty of Natural Sciences and Engineering, Aškerčeva cesta 12, SI-1000 Ljubljana, Slovenia;
E-mail: milivoj.vulic@ntf.uni-lj.si, franc.runovc@ntf.uni-lj.si
[3]Geoinvest d.o.o., Dimičeva ulica 16, SI-1000 Ljubljana, Slovenia;
E-mail: tinahabe@gmail.com

Received: November 29, 2007 **Accepted:** January 12, 2008

Abstract: This work's intention is to present the basic characteristics of projective geometry and the use of homogeneous (projective) coordinates in two-dimensional (further denoted as 2D) measurement exercises. The concept of a projective plane originates from the Euclidean plane, assuming all our given points are ideal and lie upon an ideal line verging towards infinity. The term "ideal point" is taken to mean an intersection of all lines that are parallel in the finite space. By introducing these so-called ideal points and ideal lines, the calculations in 2D measurement exercises – ones that are usually carried out under the rules of Euclidean trigonometry – have been simplified, as the calculations of directional angles and lengths are no longer necessary. As a practical example of the use of projective coordinates, an intersection is presented, such that it can also be used for the Collins Method of Resection, seeing as it is based upon using said intersection twice.

Izvleček: Predstavljene so osnovne značilnosti projektivne geometrije in s tem uporaba homogenih (projektivnih) koordinat v dvodimenzionalnih merskih nalogah. Projektivno ravnino dobimo iz evklidske ravnine, če privzamemo točke in premico v neskončnosti na kateri ležijo vse točke v neskončnosti. Neskončna točka predstavlja presečišče vseh premic, ki so v končnosti med seboj vzporedne. Z uvedbo neskončnih točk in neskončne premice se izračuni v dvodimenzionalnih merskih nalogah, ki se navadno vršijo po pravilih evklidske trigonometrije, poenostavijo saj računanje smernih kotov in dolžin ni potrebno. Kot praktični primer uporabe projektivnih koor-

Scientific paper

dinat je prikazan zunanji urez, ki ga je možno uporabiti tudi pri Collinsovi metodi notranjega ureza, saj temelji na dvakratni uporabi zunanjega ureza.

Key words: homogeneous coordinates of a point, homogeneous coordinates of a line, incidence relation, principle of duality, ideal point, ideal line, intersection, resection

Ključne besede: homogene koordinate točke, homogene koordinate premice, relacija incidence, princip dualnosti, neskončna točka, premica v neskončnosti, zunanji urez, notranji urez

INTRODUCTION

In 2D measurement exercises, all calculations are usually carried out under the rule of Euclidean geometry - where the points, lines and their relationships are defined differently than in a projective plane - in which the coordinates of an unknown point are established through the aid the calculation of so-called lengths and angles of our site. As a reaction to the latter, the article at hand is meant to present the basic relations between points and lines of the projective plane and depict their use in 2D measurement exercises. A practical example of using said projective coordinates would be an intersection, in which the coordinates of a new point are calculated from the measured angles of given points of an existing triangulation network. In what follows, the coordinates of a point and the formulas of lines on a Euclidean plane shall be marked using upper case, whereas the coordinates of points and formulas of lines on the projective plane will be denoted using lower case letters.

POINT AND LINE

In projective geometry, a point is defined as a set of three coordinates that equal the set ($y\ x\ \omega$) and therefore obviously also as an ordered set of three numbers ($y\ x\ \omega$) - which do not all equal zero at the same time, since then ($\lambda y\ \lambda x\ \lambda\omega$) would be the same point for any given $\lambda \neq 0$.

For example, (2 3 6) is our exemplary point, and (⅓ ½ 1) is another of the numerous ways to mark that exact same point, bearing in mind the principle that an unlimited number of sets of three numbers ($y\ x\ \omega$) may correspond to each point, but only one point may correspond to each ordered set. Furthermore, from non-homogeneous coordinates of any given point, we beget an infinite number of sets of homogeneous coordinates of that same point:

$$\lambda \neq 0 \Rightarrow \begin{pmatrix} Y \\ X \end{pmatrix} \rightarrow \lambda \begin{pmatrix} X \\ Y \\ 1 \end{pmatrix} = \begin{pmatrix} y \\ x \\ \omega \end{pmatrix} \tag{1}$$

And from homogeneous coordinates of that certain point, we can get one single ordered pair of numbers:

$$\lambda \neq 0 \Rightarrow \lambda \begin{pmatrix} y \\ x \\ \omega \end{pmatrix} = \begin{pmatrix} \lambda y \\ \lambda x \\ \lambda\omega \end{pmatrix} = \begin{pmatrix} \frac{\lambda y}{\lambda\omega} \\ \frac{\lambda x}{\lambda\omega} \\ \frac{\lambda\omega}{\lambda\omega} \end{pmatrix} = \begin{pmatrix} \frac{\lambda y}{\lambda\omega} \\ \frac{\lambda x}{\lambda\omega} \\ 1 \end{pmatrix} = \begin{pmatrix} \frac{\lambda y}{\lambda\omega} \\ \frac{\lambda x}{\lambda\omega} \end{pmatrix} = \begin{pmatrix} Y \\ X \end{pmatrix} \tag{2}$$

A line is defined in almost the same way as a point, the one difference being that the line is treated as a set of all points that equal the set of three ($v\ u\ w$). For example, if (3 2 -2) defines a line, then (-3/2 -1 1) is the notation for that same line. In other words, a line is an ordered set of three numbers, denoted as ($v\ u\ w$), which do not equal zero all at the same time, in which case ($\mu v\ \mu u\ \mu w$) would be the same line for any given $\mu \neq 0$ [1].

Incidence relation

Given point P and line l - where P and l are short for ($y\ x\ \omega$) and ($v\ u\ w$), respectively - we say that the two are incident to one another (incidence relation being descriptive of the relation simply summed up as the point lying on the line i.e. the line going "through" the point) in the case, the following is true: $\{P \cdot l\} = \{l \cdot P\} = yv + xu + \omega w = vy + ux + w\omega = 0$ [2].

The principle of duality

The axiom of geometry says that there is exactly one line that is in incidence with two different points P_1 and P_2, i.e. exactly one line goes through both different points. If we exchange the term "line" with the term "point" in the above axiom, we get a geometrical theorem that states there is exactly one point that is in incidence with two different lines l_1 and l_2 - in other words, two different lines intersect at exactly one point in space. The afore-mentioned axiom and theorem are said to be mutually dual, i.e. points and lines are mutually dual spatial elements, while the "running" and intersecting of lines are mutually dual operations[3].

For different points $P_1(y_1\ x_1\ \omega_1)$ and $P_2(y_2\ x_2\ \omega_2)$; $y_1 \neq \lambda \cdot y_2, x_1 \neq \lambda \cdot x_2$, $\omega_1 \neq \lambda \cdot \omega_2$ there is always an ordered set of three elements, ($v\ u\ w$), for which the following need most definitely apply:

$$\begin{aligned} y_1 v + x_1 u + \omega_1 w &= 0 \\ y_2 v + x_2 u + \omega_2 w &= 0 \end{aligned} \tag{3}$$

And for two different lines, in our particular example l_1 ($v_1\ u_1\ w_1$) and l_2 ($v_2\ u_2\ w_2$); $v_1 \neq \mu \cdot v_2$, $u_1 \neq \mu \cdot u_2$, $w_1 \neq \mu \cdot w_2$; there is always an ordered set of three elements, ($y\ x\ \omega$), for which the following need apply:

$$\begin{aligned} v_1 y + u_1 x + w_1\, \omega &= 0 \\ v_2 y + u_2 x + w_2\, \omega &= 0 \end{aligned} \tag{4}$$

Thus, homogeneous systems of equations are combined with the following expression:

$$\begin{vmatrix} \begin{Bmatrix} P \\ l \end{Bmatrix} \\ \begin{Bmatrix} P \\ l \end{Bmatrix}_1 \\ \begin{Bmatrix} P \\ l \end{Bmatrix}_2 \end{vmatrix} = \begin{vmatrix} \begin{Bmatrix} y \\ v \end{Bmatrix} & \begin{Bmatrix} x \\ u \end{Bmatrix} & \begin{Bmatrix} \omega \\ w \end{Bmatrix} \\ \begin{Bmatrix} v \\ y \end{Bmatrix}_1 & \begin{Bmatrix} u \\ x \end{Bmatrix}_1 & \begin{Bmatrix} w \\ \omega \end{Bmatrix}_1 \\ \begin{Bmatrix} v \\ y \end{Bmatrix}_2 & \begin{Bmatrix} u \\ x \end{Bmatrix}_2 & \begin{Bmatrix} w \\ \omega \end{Bmatrix}_2 \end{vmatrix} = 0 \Rightarrow \begin{cases} \begin{vmatrix} P \\ l_1 \\ l_2 \end{vmatrix} = \begin{vmatrix} y & x & \omega \\ v_1 & u_1 & w_1 \\ v_2 & u_2 & w_2 \end{vmatrix} = 0 \\ \begin{vmatrix} l \\ P_1 \\ P_2 \end{vmatrix} = \begin{vmatrix} v & u & w \\ y_1 & x_1 & \omega_1 \\ y_2 & x_2 & \omega_2 \end{vmatrix} = 0 \end{cases} \tag{5}$$

Then we are able to beget the formula of the point or line:

$$\begin{vmatrix} \begin{Bmatrix} y \\ v \end{Bmatrix} & \begin{Bmatrix} x \\ u \end{Bmatrix} & \begin{Bmatrix} \omega \\ w \end{Bmatrix} \\ \begin{Bmatrix} v \\ y \end{Bmatrix}_1 & \begin{Bmatrix} u \\ x \end{Bmatrix}_1 & \begin{Bmatrix} w \\ \omega \end{Bmatrix}_1 \\ \begin{Bmatrix} v \\ y \end{Bmatrix}_2 & \begin{Bmatrix} u \\ x \end{Bmatrix}_2 & \begin{Bmatrix} w \\ \omega \end{Bmatrix}_2 \end{vmatrix} = \begin{Bmatrix} y \\ v \end{Bmatrix} \begin{vmatrix} \begin{Bmatrix} u \\ x \end{Bmatrix}_1 & \begin{Bmatrix} w \\ \omega \end{Bmatrix}_1 \\ \begin{Bmatrix} u \\ x \end{Bmatrix}_2 & \begin{Bmatrix} w \\ \omega \end{Bmatrix}_2 \end{vmatrix} - \begin{Bmatrix} x \\ u \end{Bmatrix} \begin{vmatrix} \begin{Bmatrix} v \\ y \end{Bmatrix}_1 & \begin{Bmatrix} w \\ \omega \end{Bmatrix}_1 \\ \begin{Bmatrix} v \\ y \end{Bmatrix}_2 & \begin{Bmatrix} w \\ \omega \end{Bmatrix}_2 \end{vmatrix} + \begin{Bmatrix} \omega \\ w \end{Bmatrix} \begin{vmatrix} \begin{Bmatrix} v \\ y \end{Bmatrix}_1 & \begin{Bmatrix} u \\ x \end{Bmatrix}_1 \\ \begin{Bmatrix} v \\ y \end{Bmatrix}_2 & \begin{Bmatrix} u \\ x \end{Bmatrix}_2 \end{vmatrix} = 0 \tag{6}$$

Each set of three $\left(\begin{Bmatrix} y \\ v \end{Bmatrix} \quad \begin{Bmatrix} x \\ u \end{Bmatrix} \quad \begin{Bmatrix} \omega \\ w \end{Bmatrix} \right)$ therefore represents a solution to the system under question.

The coordinates of the point or line follow:

$$\begin{Bmatrix} y \\ v \end{Bmatrix} : \begin{Bmatrix} x \\ u \end{Bmatrix} : \begin{Bmatrix} \omega \\ w \end{Bmatrix} = \begin{vmatrix} \begin{Bmatrix} u \\ x \end{Bmatrix}_1 & \begin{Bmatrix} w \\ \omega \end{Bmatrix}_1 \\ \begin{Bmatrix} u \\ x \end{Bmatrix}_2 & \begin{Bmatrix} w \\ \omega \end{Bmatrix}_2 \end{vmatrix} : \begin{vmatrix} \begin{Bmatrix} w \\ \omega \end{Bmatrix}_1 & \begin{Bmatrix} v \\ y \end{Bmatrix}_1 \\ \begin{Bmatrix} w \\ \omega \end{Bmatrix}_2 & \begin{Bmatrix} v \\ y \end{Bmatrix}_2 \end{vmatrix} : \begin{vmatrix} \begin{Bmatrix} v \\ y \end{Bmatrix}_1 & \begin{Bmatrix} u \\ x \end{Bmatrix}_1 \\ \begin{Bmatrix} v \\ y \end{Bmatrix}_2 & \begin{Bmatrix} u \\ x \end{Bmatrix}_2 \end{vmatrix} \tag{7}$$

A point or a line pertaining to a projective plane can be multiplied by any number λ or μ , as long as the value is not equal to zero, which then gives us the actual coordinates of this same point or line:

$$\left(\begin{Bmatrix} y \\ v \end{Bmatrix} : \begin{Bmatrix} x \\ u \end{Bmatrix} : \begin{Bmatrix} \omega \\ w \end{Bmatrix} \right) = \begin{Bmatrix} \lambda \\ \mu \end{Bmatrix} \left(\begin{vmatrix} \begin{Bmatrix} u \\ x \end{Bmatrix}_1 & \begin{Bmatrix} w \\ \omega \end{Bmatrix}_1 \\ \begin{Bmatrix} u \\ x \end{Bmatrix}_2 & \begin{Bmatrix} w \\ \omega \end{Bmatrix}_2 \end{vmatrix} \begin{vmatrix} \begin{Bmatrix} w \\ \omega \end{Bmatrix}_1 & \begin{Bmatrix} v \\ y \end{Bmatrix}_1 \\ \begin{Bmatrix} w \\ \omega \end{Bmatrix}_2 & \begin{Bmatrix} v \\ y \end{Bmatrix}_2 \end{vmatrix} \begin{vmatrix} \begin{Bmatrix} v \\ y \end{Bmatrix}_1 & \begin{Bmatrix} u \\ x \end{Bmatrix}_1 \\ \begin{Bmatrix} v \\ y \end{Bmatrix}_2 & \begin{Bmatrix} u \\ x \end{Bmatrix}_2 \end{vmatrix} \right) \tag{8}$$

For a point, this would be:

$$(y \quad x \quad \omega) = \mu \left(\begin{vmatrix} u_1 & w_1 \\ u_2 & w_2 \end{vmatrix} \begin{vmatrix} w_1 & v_1 \\ w_2 & v_2 \end{vmatrix} \begin{vmatrix} v_1 & u_1 \\ v_2 & u_2 \end{vmatrix} \right) \tag{9}$$

And for a line:

$$(v \quad u \quad w) = \lambda \left(\begin{vmatrix} x_1 & \omega_1 \\ x_2 & \omega_2 \end{vmatrix} \begin{vmatrix} \omega_1 & y_1 \\ \omega_2 & y_2 \end{vmatrix} \begin{vmatrix} y_1 & x_1 \\ y_2 & x_2 \end{vmatrix} \right) \tag{10}$$

THE IDEAL POINT AND LINE

The parallels *(coefficient of site* $k = k_1 = k_2$*)* l_1 and l_2 with formulas $Y = k_1X + n_1$ and $Y = k_2X + n_2$ are given. For X, we enter values $X = \frac{x}{\omega}$, and for Y values $Y = \frac{y}{\omega}$, then multiplying the equations with ω, which in turn gives us the formulas of lines using homogeneous coordinates:

$$y = kx + n_1\omega \text{ and } y = kx + n_2\omega \tag{11}$$

Considering that the lines are parallel, we are interested in the set of three, $(v\ u\ w)$, such that it must correspond to both formulas.

By subtracting the equations we get: $\omega(n_1 - n_2) = 0$.

As $n_1 \neq n_2$, then $\omega = 0$ and the equations $y = kx + n_1\omega$ and $y = kx + n_2\omega$ are reduced into $y = xk$.

Since we are dealing with homogeneous coordinates, we can say that $x = 1$. From this, we come to the conclusion that $y = k$. Thus, we obtain a set of three, $(k\ 1\ 0)$, which does indeed correspond to both equations.

If the lines l_1 and l_2 are parallel to the y-axis, then the formulas of the lines in homogeneous coordinates have the form $x = \omega x_1$ and $x = \omega x_2$. In this case, the set of three (0 1 0) corresponds to both formulas.

To summarize, the set of three, $(k\ 1\ 0)$, corresponds to a formula of the forms $y = kx + n_1\omega$ and $y = kx + n_2\omega$ only when $k = k_1 = k_2$, or when the lines are parallel and the coefficient of site equals k. The set of three (0 1 0) corresponds to all formulas of the form $x = \omega x_1$ that describe the parallels of the y-axis.

A bouquet of parallel lines (all parallel lines are of the same class and form organised heaps of parallel lines denoted as “bouquets”) defines a point P_∞ in projective plane that has been defined as an ideal point. The bouquet P_∞ consists of all lines that are parallel to

a certain line l. The equation pertaining to line l is $Y = kX + n$, or $X = X_P$ if it is parallel to the y rather than the x-axis.

The line l belongs to bouquet P_∞ exactly when the set of three (k 1 0) corresponds to the equation of line l in its homogeneous coordinates, and to pencil P_∞ exactly when what corresponds to this equation is this set of three: (0 1 0). Consequentially, we can have the set of three (k 1 0) in the former case, and the set of three (0 1 0) in the latter case for homogeneous coordinates of the ideal point P_∞.

Since we may multiply homogeneous coordinates with any number that is different than zero, we may say that the set of three (y x 0) represents the homogeneous coordinates of one ideal point, where y and x are any given elements different from zero. In this way, we have adjusted our homogeneous coordinates (y x ω) so that they befit each and every point of our projective plane. The point with such coordinates also lies in the Euclidean plane if $\omega \neq 0$, and is an ideal point when $\omega = 0$ [4].

Two ideal points define the ideal line l_∞:

$$\begin{vmatrix} v_\infty & u_\infty & w_\infty \\ y_1 & x_1 & 0 \\ y_2 & x_2 & 0 \end{vmatrix} = 0 \tag{12}$$

The solution of the system are the very coordinates of our ideal line l_∞:

$$(v_\infty \quad u_\infty \quad w_\infty) = \mu \left(\begin{vmatrix} x_1 & 0 \\ x_2 & 0 \end{vmatrix} \begin{vmatrix} 0 & y_1 \\ 0 & y_2 \end{vmatrix} \begin{vmatrix} y_1 & x_1 \\ y_2 & x_2 \end{vmatrix} \right) = \mu \left(0 \quad 0 \quad \begin{vmatrix} y_1 & x_1 \\ y_2 & x_2 \end{vmatrix} \right) \tag{13}$$

or, if:

$$\left(\mu \neq 0 \wedge \begin{vmatrix} y_1 & x_1 \\ y_2 & x_2 \end{vmatrix} \neq 0 \wedge \mu = \frac{1}{\begin{vmatrix} y_1 & x_1 \\ y_2 & x_2 \end{vmatrix}} \right) \Rightarrow (v_\infty \quad u_\infty \quad w_\infty) = (0 \quad 0 \quad 1) \tag{14}$$

The set of three (0 0 1) represents the coordinates of an ideal line such that all ideal points lie on it.

THE IDEAL LINE AND ANGLE OF SITE

An ideal point represents the intersection of a group of all lines that are parallel to one another in finite space. A specific ideal point upon an ideal line belongs to each group of parallel lines that in finite space represent a so-called »angle of site« between the lines of a certain class and the positive end of the x-axis.

The coordinates of the line that goes through the points $P_1(y_1\ x_1\ \omega_1)$ and $P_2(y_1 + d\cos\varphi\ x_1 + d\sin\varphi\ \omega_2)$, where φ is the so-called angle of site are enclosed within the line $\overline{P_1P_2}$ and the positive side of x-axis, and d represents the distance between the points P_1 and P_2, which would be:

$$(v\ u\ w) = \mu\ (x_1(\omega_2 - \omega_1) - d\cos\varphi\omega_1\ \ y(\omega_1 - \omega_2) + d\sin\varphi\omega_2\ \ d(y_1\cos\varphi - x_1\sin\varphi)) \tag{15}$$

If :

$$\omega_2 = \omega_1 = 1 \Rightarrow (v\ u\ w) = \mu\ (-d\cos\varphi \quad d\sin\varphi \quad d(y_1\cos\varphi - x_1\sin\varphi)) \tag{16}$$

or, when:

$$(\omega_2 = \omega_1 = 1 \wedge d \neq 0 \wedge d \neq \infty \wedge \mu = \tfrac{1}{d}) \Rightarrow (v\ u\ w) = (-\cos\varphi\ \sin\varphi\ (y_1\cos\varphi - x_1\sin\varphi)) \tag{17}$$

The set $(v\ u\ w) = (-\cos\varphi\ \sin\varphi\ (y_1\cos\varphi - x_1\sin\varphi))$ represents the coordinates of the line that is notated using polar coordinates.

The intersection of the line given with polar coordinates and the ideal line (0 0 1) is the ideal line, now denoted using polar coordinates:

$$(y_\infty\ \ x_\infty\ \ \omega_\infty) = \lambda\left(\begin{vmatrix}\sin\varphi & y_1\cos\varphi - x_1\sin\varphi\\ 0 & 1\end{vmatrix}\ \begin{vmatrix}y_1\cos\varphi - x_1\sin\varphi & -\cos\varphi\\ 1 & 0\end{vmatrix}\ \begin{vmatrix}-\cos\varphi & \sin\varphi\\ 0 & 0\end{vmatrix}\right) \tag{18}$$

or, if:

$$\lambda = 1 \Rightarrow (y_\infty\ \ x_\infty\ \ \omega_\infty) = (\sin\varphi\ \ \cos\varphi\ \ 0) \tag{19}$$

The notation $(y_\infty\ \ x_\infty\ \ \omega_\infty) = (\sin\varphi\ \ \cos\varphi\ \ 0)$ at the same time alos represents standardised coordinates of said ideal line, for which the following is valid:

$$(y_\infty\ \ x_\infty\ \ \omega_\infty)\begin{pmatrix}y_\infty\\ x_\infty\\ \omega_\infty\end{pmatrix} = \left(\frac{y_\infty}{\sqrt{y_\infty^{\,2} + x_\infty^{\,2}}}\ \ \frac{x_\infty}{\sqrt{y_\infty^{\,2} + x_\infty^{\,2}}}\ \ 0\right)\begin{pmatrix}\dfrac{y_\infty}{\sqrt{y_\infty^{\,2} + x_\infty^{\,2}}}\\ \dfrac{x_\infty}{\sqrt{y_\infty^{\,2} + x_\infty^{\,2}}}\\ 0\end{pmatrix} = 1 \tag{20}$$

where:

$$\varphi = \tan^{-1}\left(\frac{\sin\varphi}{\cos\varphi}\right) = \frac{\dfrac{y_\infty}{\sqrt{y_\infty^2 + x_\infty^2}}}{\dfrac{x_\infty}{\sqrt{y_\infty^2 + x_\infty^2}}} = \tan^{-1}\frac{y_\infty}{x_\infty} \tag{21}$$

Should the lines l_1 in l_2 enclose the angle α , and the line l_1 is defined through the ideal point (sin φ_1 cos φ_1 0), then the ideal point of line l_2 is defined as (sin ($\varphi_1 \pm \alpha$) cos ($\varphi_1 \pm \alpha$) 0), where $\varphi_1 \pm \alpha$ is the angle of site of the line l_2:

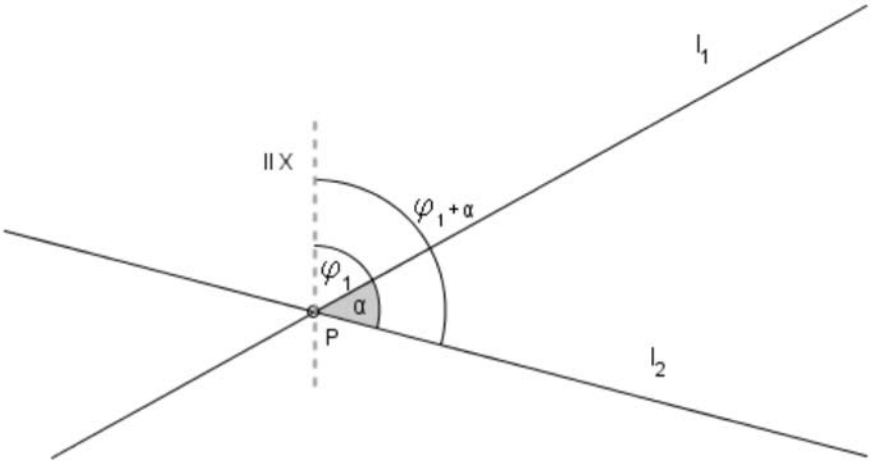

Figure 1. The angle between our two lines and angles of site
Slika 1. Kot med premicama in smerna kota

INTERSECTION

An intersection is both a measurement and calculation method, with the aid of which the coordinates of a new point can be calculated from measured angles or (outer) directions upon given points of the existing triangulation network. A given new point is determined as an intersection of several outer directions that are controllably oriented at each standpoint.

The coordinates of points $L(Y_L\ X_L)$ and $R(Y_R\ X_R)$ are given.

Observation:
We are observing the direction from two given points (L and R) towards the new point M. Angle α is observed from the point L between points *M-left* and *R-right*, and angle β from point R between points *L-left* and *M-right*.

Based on the given and observed information, we must establish the coordinates of the unknown point M, which would translate into us looking for X_M and Y_M:

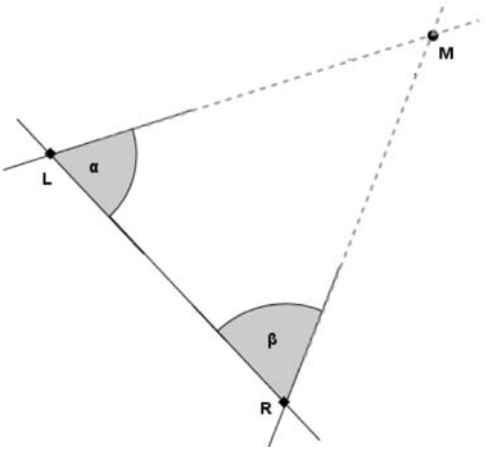

Figure 2. Intersection
Slika 2. Zunanji urez

The connecting line $\overline{LM}$ denotes the line *left*, $\overline{RM}$ the line *right*, and $\overline{LR}$ the line *left-right*. The lines *left* and *left-right* are bisected via one another in point *L* and enclose the angle α, while the lines *right* and *left-right* do the same in point *R*, therefore enclosing the angle β.

By establishing the ideal point L_∞ of the line *left* and the ideal point R_∞ of the line *right*, the lines *left* and *right* have been accurately established. Thus, we have also established their intersection *M*, which represents the coordinates of the point we are seeking.

L_∞ denotes the ideal point on the line *left,*, R_∞ the ideal point on the line *right* and LR_∞ the ideal point on the line *left-right*. Points L_∞ and R_∞ are obtained with the help of the ideal point LR_∞, which is established through the bisection of line *left-right* with the ideal line. When the point LR_∞ is standardised (transformed into a format such as (sin φ cos φ 0)), we can, with the help of the latter, as well as with the help of angles α and β, determine the points L_∞ and R_∞ on the line l_∞.

1. ***Establishing the line left-right***

- The coordinates of point *L* are ($y_L = Y_L$ $x_L = X_L$ 1)
- The coordinates of point *R* are ($y_L = Y_R = Y_L + X_L + d \sin \upsilon_L^R$ $x_L = X_R = X_L + d \cos \upsilon_L^R$ 1)

Therefore, the following is true:

$$\begin{vmatrix} v_{LR} & u_{LR} & w_{LR} \\ Y_L & X_L & 1 \\ Y_L + d \cdot \sin v_L^R & X_L + d \cdot \cos v_L^R & 1 \end{vmatrix} = 0 \tag{22}$$

The formula of the line *left-right* is:

$$v_{LR}\begin{vmatrix} X_L & 1 \\ X_L + d\cdot\cos\nu_L^R & 1 \end{vmatrix} - u_{LR}\begin{vmatrix} Y_L & 1 \\ Y_L + d\cdot\sin\nu_L^R & 1 \end{vmatrix} + w_{LR}\begin{vmatrix} Y_L & X_L \\ Y_L + d\cdot\sin\nu_L^R & X_L + d\cdot\cos\nu_L^R \end{vmatrix} = 0 \tag{23}$$

or, its coordinates:

$$v_{LR} = \begin{vmatrix} X_L & 1 \\ X_L + d\cos\nu_L^R & 1 \end{vmatrix} \tag{24}$$

$$u_{LR} = \begin{vmatrix} 1 & Y_L \\ 1 & Y_L + d\sin\nu_L^R \end{vmatrix} \tag{25}$$

$$w_{LR} = \begin{vmatrix} Y_L & X_L \\ Y_L + d\cdot\sin\nu_L^R & X_L + d\cdot\cos\nu_L^R \end{vmatrix} = \begin{vmatrix} Y_L & X_L \\ Y_L & X_L \end{vmatrix} + \begin{vmatrix} Y_L & X_L \\ d\cdot\sin\nu_L^R & d\cdot\cos\nu_L^R \end{vmatrix} \tag{26}$$

2. *Establishing the ideal point on the line left-right*

The line *left-right* is bisected with the ideal point (0 0 1):

$$\begin{vmatrix} y_{LR_\infty} & x_{LR_\infty} & \omega_{LR\infty} \\ 0 & 0 & 1 \\ \begin{vmatrix} X_L & 1 \\ X_L + d\cdot\cos\nu_L^R & 1 \end{vmatrix} & \begin{vmatrix} 1 & Y_L \\ 1 & Y_L + d\cdot\sin\nu_L^R \end{vmatrix} & \begin{vmatrix} Y_L & X_L \\ Y_L + d\cdot\sin\nu_L^R & X_L + d\cdot\cos\nu_L^R \end{vmatrix} \end{vmatrix} = 0 \tag{27}$$

The coordinates of the ideal point are denoted as follows:

$$\begin{aligned} y_{LR_\infty} &= \begin{vmatrix} 0 & 1 \\ \begin{vmatrix} 1 & Y_L \\ 1 & Y_L + d\cdot\sin\nu_L^R \end{vmatrix} & \begin{vmatrix} Y_L & X_L \\ d\cdot\sin\nu_L^R & d\cdot\cos\nu_L^R \end{vmatrix} \end{vmatrix} = -\begin{vmatrix} 1 & Y_L \\ 1 & Y_L + d\cdot\sin\nu_L^R \end{vmatrix} = \\ &= -\begin{vmatrix} 1 & Y_L \\ 1 & Y_L \end{vmatrix} - \begin{vmatrix} 1 & 0 \\ 1 & d\cdot\sin\nu_L^R \end{vmatrix} = -d\cdot\sin\nu_L^R \end{aligned} \tag{28}$$

$$\begin{aligned} x_{LR_\infty} &= \begin{vmatrix} 1 & 0 \\ \begin{vmatrix} Y_L & X_L \\ d\cdot\sin\nu_L^R & d\cdot\cos\nu_L^R \end{vmatrix} & \begin{vmatrix} X_L & 1 \\ X_L + d\cdot\cos\nu_L^R & 1 \end{vmatrix} \end{vmatrix} = \begin{vmatrix} X_L & 1 \\ X_L + d\cdot\cos\nu_L^R & 1 \end{vmatrix} = \\ &= \begin{vmatrix} X_L & 1 \\ X_L & 1 \end{vmatrix} + \begin{vmatrix} 0 & 1 \\ d\cdot\cos\nu_L^R & 1 \end{vmatrix} = -d\cdot\cos\nu_L^R \end{aligned} \tag{29}$$

$$\omega_{LR_\infty} = \begin{vmatrix} 0 & 0 \\ \begin{vmatrix} X_L & 1 \\ X_L + d\cdot\sin\nu_L^R & 1 \end{vmatrix} & \begin{vmatrix} 1 & Y_L \\ 1 & Y_L + d\cdot\cos\nu_L^R \end{vmatrix} \end{vmatrix} \tag{30}$$

The point $LR_\infty = \lambda(-d \sin \upsilon_L^R - d \cos \upsilon_L^R \; 0)$ is standardised, which means that it is multiplied by factor:

$$\lambda = \frac{1}{\sqrt{y_{LR_\infty}{}^2 + x_{LR_\infty}{}^2 + \omega_{LR_\infty}{}^2}}$$

Consequentially, we transform the notation $LR_\infty = \lambda(-d \sin \upsilon_L^R - d \cos \upsilon_L^R \; 0)$ into $LR_\infty = \lambda(\pm \sin \upsilon_L^R \pm \cos \upsilon_L^R \; 0)$.

$$\lambda = \frac{1}{\sqrt{y_{LR_\infty}{}^2 + x_{LR_\infty}{}^2 + \omega_{LR_\infty}{}^2}} \Rightarrow LR_\infty = \lambda\left(-d \cdot \sin\nu_L^R \; -d \cdot \cos\nu_L^R \; 0\right) \tag{31}$$

$$\lambda = \frac{1}{\sqrt{\left(d \cdot \sin\nu_L^R\right)^2 + \left(d \cdot \cos\nu_L^R\right)^2}} \Rightarrow LR_\infty = \lambda\left(-d \cdot \sin\nu_L^R \; -d \cdot \cos\nu_L^R \; 0\right) \tag{32}$$

$$\lambda = \frac{1}{\sqrt{d^2\left(\sin^2\nu_L^R + \cos^2\nu_L^R\right)}} \Rightarrow LR_\infty = \lambda\left(-d \cdot \sin\nu_L^R \; -d \cdot \cos\nu_L^R \; 0\right) \tag{33}$$

$$\lambda = \frac{1}{\sqrt{d^2}} \Rightarrow LR_\infty = \lambda\left(-d \cdot \sin\nu_L^R \; -d \cdot \cos\nu_L^R \; 0\right) \tag{34}$$

$$LR_\infty = \pm\frac{1}{d}\left(-d \cdot \sin\nu_L^R \; -d \cdot \cos\nu_L^R \; 0\right) \tag{35}$$

So, finally, the standardised ideal point is:

$$LR_\infty = \left(\mp\sin\nu_L^R \; \mp\cos\nu_L^R \; 0\right) \tag{36}$$

or:

$$LR_\infty = \left(\mp\sin\left(\nu_L^R + k\pi\right) \mp\cos\left(\nu_L^R + k\pi\right) 0\right) \tag{37}$$

3. *Establishing the ideal points on the lines left and right*

(a) Ideal point L_∞ of the line *left*

The line *left-right* encloses, along with the positive side of *x*-axis, the angle υ_L^R, and with the line *left*, the angle α. The angle of site of the line *left* is $\upsilon_L^M = \upsilon_L^R - \alpha$ and the ideal line is of the form:

$$L_\infty = (\sin(\upsilon_L^R - \alpha) \cos(\upsilon_L^R - \alpha) \; 0) \tag{38}$$

(b) Ideal point R_∞ of the line *right*

The coefficient of site of the line *right* is $\upsilon_L^M = \upsilon_L^R + \beta$ and the ideal line is of the form:

$$R_\infty = (\sin(\upsilon_L^R + \beta) \cos(\upsilon_L^R + \beta) \; 0) \tag{39}$$

4. *Establishing the lines left and right*

(a) Establishing the line *left*:

The line *left* goes through the points L_∞ and L:

$$\begin{vmatrix} v_{left} & u_{left} & w_{left} \\ \sin\nu_L^R \cdot \cos\alpha - \cos\nu_L^R \cdot \sin\alpha & \cos\nu_L^R \cdot \cos\alpha + \sin\nu_L^R \cdot \sin\alpha & 0 \\ Y_{left} & X_{left} & 1 \end{vmatrix} = 0 \tag{40}$$

$$v_{left} = \begin{vmatrix} \cos\nu_L^R \cdot \cos\alpha + \sin\nu_L^R \cdot \sin\alpha & 0 \\ X_{left} & 1 \end{vmatrix} = \cos\nu_L^R \cdot \cos\alpha + \sin\nu_L^R \cdot \sin\alpha = \cos\left(\nu_L^R - \alpha\right) \tag{41}$$

$$u_{left} = \begin{vmatrix} 0 & \sin\nu_L^R \cdot \cos\alpha - \cos\nu_L^R \cdot \sin\alpha \\ 1 & 1 \end{vmatrix} = -\sin\nu_L^R \cdot \cos\alpha - \cos\nu_L^R \cdot \sin\alpha = -\sin\left(\nu_L^R - \alpha\right) \tag{42}$$

$$\begin{aligned} w_{left} &= \begin{vmatrix} \sin\nu_L^R \cdot \cos\alpha - \cos\nu_L^R \cdot \sin\alpha & \cos\nu_L^R \cdot \cos\alpha + \sin\nu_L^R \cdot \sin\alpha \\ Y_{left} & X_{left} \end{vmatrix} = \\ &= -Y_{left} \cdot \cos\left(\nu_L^R - \alpha\right) - X_{left} \cdot \sin\left(\nu_L^R - \alpha\right) \end{aligned} \tag{43}$$

Coordinates of the line *left*:

$$\left(v_{left} \;\; u_{left} \;\; w_{left}\right) = \left(\cos\left(\nu_L^R - \alpha\right) - \sin\left(\nu_L^R - \alpha\right) - Y_{left} \cdot \cos\left(\nu_L^R - \alpha\right) - X_{left} \cdot \sin\left(\nu_L^R - \alpha\right)\right) \tag{44}$$

(b) Establishing the line *right*

The line *right* is defined by the points R and R_∞:

$$\begin{vmatrix} v_{right} & u_{right} & w_{right} \\ \sin\nu_R^L \cdot \cos\beta + \cos\nu_R^L \cdot \sin\beta & \cos\nu_R^L \cdot \cos\beta - \sin\nu_R^L \cdot \sin\beta & 0 \\ Y_{right} & X_{right} & 1 \end{vmatrix} = 0 \tag{45}$$

$$v_{right} = \begin{vmatrix} \cos\nu_R^L \cdot \cos\beta - \sin\nu_R^L \cdot \sin\beta & 0 \\ X_{right} & 1 \end{vmatrix} = \cos\nu_R^L \cdot \cos\beta - \sin\nu_R^L \cdot \sin\beta = \cos\left(\nu_R^L + \beta\right) \tag{46}$$

$$u_{right} = \begin{vmatrix} 0 & \sin\nu_R^L \cdot \cos\beta + \cos\nu_R^L \cdot \sin\beta \\ 1 & 1 \end{vmatrix} = -\sin\nu_R^L \cdot \cos\beta + \cos\nu_R^L \cdot \sin\beta = -\sin\left(\nu_R^L + \beta\right) \tag{47}$$

$$\begin{aligned} w_{right} &= \begin{vmatrix} \sin\nu_R^L \cdot \cos\beta + \cos\nu_R^L \cdot \sin\beta & \cos\nu_R^L \cdot \cos\beta - \sin\nu_R^L \cdot \sin\beta \\ Y_{right} & X_{right} \end{vmatrix} = \\ &= -Y_{right} \cdot \cos\left(\nu_R^L + \beta\right) + X_{right} \cdot \sin\left(\nu_R^L + \beta\right) \end{aligned} \tag{48}$$

Coordinates of the line *right*:

$$\left(v_{right}\ \ u_{right}\ \ w_{right}\right)=\left(\cos\left(\nu_R^L+\beta\right)\ -\sin\left(\nu_R^L+\beta\right)\ -Y_{right}\cdot\cos\left(\nu_R^L+\beta\right)+X_{right}\cdot\sin\left(\nu_R^L+\beta\right)\right] \quad (49)$$

5. *Establishing the unknown point M*

The point *M* is defined as the intersection of the lines $\overline{LM}=\overline{L_\infty L}$ and $\overline{RM}=\overline{R_\infty R}$:

$$\begin{vmatrix} y_M & x_M & \omega_M \\ v_{left} & u_{left} & w_{left} \\ v_{right} & u_{right} & w_{right} \end{vmatrix}=0 \quad (50)$$

$$M=\left(y_M\ \ x_M\ \ \omega_M\right)=\left(\begin{vmatrix} u_{left} & w_{left} \\ u_{right} & w_{right} \end{vmatrix}\begin{vmatrix} w_{left} & v_{left} \\ w_{right} & v_{right} \end{vmatrix}\begin{vmatrix} v_{left} & u_{left} \\ v_{right} & u_{right} \end{vmatrix}\right)^{[1]} \quad (51)$$

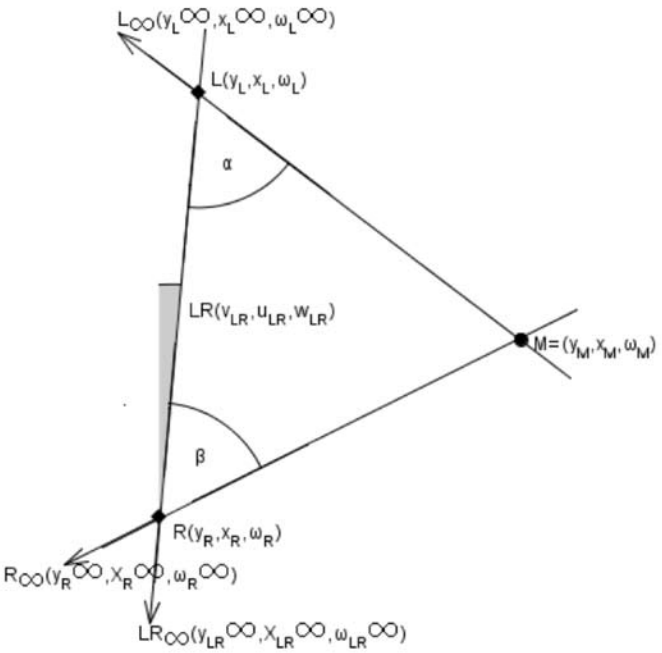

Figure 3. Intersection with projective coordinates
Slika 3. Zunanji urez s projektivnimi koordinatami

CONCLUSIONS

In projective geometry, the lines have their own coordinates inasmuch as points do. A point is defined as an ordered set of three numbers ($y\ x\ \omega$), which are not allowed to simultaneously take on the value of zero, seeing as the latter would make ($\lambda y\ \lambda x\ \lambda\omega$) the same point for any given $\lambda \neq 0$. We can obtain an infinite number of ordered sets of coordinates of a given point from the non-homogeneous coordinates of that same point, just as well as we can obtain only one ordered pair of numbers from homogeneous coordinates.

A line, much like a point, is an ordered set of three numbers, ($v\ u\ w$), which must not all equal zero at the same time, seeing as that would again make ($\mu v\ \mu u\ \mu w$) the same line for any given $\mu \neq 0$. The set ($v\ u\ w$) = (x_1-x_2 y_1-y_2 y_1x_2-y_2x_1) represents the coordinates of the line that are denoted using rectangular coordinates, whilst the set ($v\ u\ w$) = (- cos φ sin φ y_1 cos φ - x_1 sin φ) represents the coordinates of the line that is denoted using polar coordinates.

By using projective coordinates, the establishment of the intersection $R(Y\ X)$ of two lines – the line l_1, defined by the points $A_1(Y_1\ X_1)$ and $A_2(Y_2\ X_2)$, and the line l_2, on which the points $B_1(Y_1\ X_1)$ and $B_2(Y_2\ X_2)$ lie – is very simple, and is defined using the help of nine second order determinants:

First, the coordinates of lines l_1 and l_2 are established, for which six of secondary-order determinants need to be calculated:

$$\lambda = 1 \Rightarrow l_1 = (v_1 \quad u_1 \quad w_1) = \left(\begin{vmatrix} X_1 & 1 \\ X_2 & 1 \end{vmatrix} \begin{vmatrix} 1 & Y_1 \\ 1 & Y_2 \end{vmatrix} \begin{vmatrix} Y_1 & X_1 \\ Y_2 & X_2 \end{vmatrix} \right)' \tag{52}$$

$$\lambda = 1 \Rightarrow l_2 = (v_2 \quad u_2 \quad w_2) = \left(\begin{vmatrix} X_1 & 1 \\ X_2 & 1 \end{vmatrix} \begin{vmatrix} 1 & Y_1 \\ 1 & Y_2 \end{vmatrix} \begin{vmatrix} Y_1 & X_1 \\ Y_2 & X_2 \end{vmatrix} \right) \tag{53}$$

The intersection R, as the intersection of lines l_1 and l_2, is established with the calculation of another three secondary-order determinants:

$$\mu = 1 \Rightarrow R = (y \quad x \quad \omega) = \left(\begin{vmatrix} u_1 & w_1 \\ u_2 & w_2 \end{vmatrix} \begin{vmatrix} w_1 & v_1 \\ w_2 & v_2 \end{vmatrix} \begin{vmatrix} v_1 & u_1 \\ v_2 & u_2 \end{vmatrix} \right)' \tag{54}$$

$$R = (y \quad x \quad \omega) = \left(\frac{y}{\omega} \quad \frac{x}{\omega} \quad 1 \right) = (Y \quad X \quad 1) = (Y \quad X) \tag{55}$$

The projective plane, as has already been mentioned, originates from the Euclidean plane when we assume ideal points and an ideal line. Thus, the point with coordinates (y

$x\ \omega$) lies in the Euclidean plane if $\omega \neq 0$, and $\omega = 0$ to render our point ideal.

Two different ideal points define the ideal line (0 0 1), on which *all* ideal points lie. The notation (sin φ cos φ 0) represents these coordinates of our ideal point, from which we can find the angle which a given line encloses in partnership with the positive side of the *x*-axis.

If the line l_1 and the positive side of the first axis enclose the angle φ_1, and both l_1 and l_2 enclose the angle α, then the ideal point of the line l_2 can be determined as $(\sin(\varphi_1 \pm \alpha)\ \cos(\varphi_1 \pm \alpha)\ 0)$, where $\varphi_2 = \varphi_1 \pm \alpha$ is the angle of site of the line l_2.

Via the introduction of ideal points and an ideal line, we are able to avoid the process of calculation of lengths and angles of site in 2D measurement exercises (the practical example here being the one depicted using intersections). The coordinates of an unknown point may always be established as the intersection of two lines, defined by the given and ideal points.

Povzetek

Možnost uporabe homogenih (projektivnih) koordinat v dvodimenzionalnih merskih nalogah

V projektivni geometriji imajo poleg točk tudi premice koordinate.

Točka je definirana kot urejena trojka števil ($y\ x\ \omega$), ki niso vse hkrati enake nič, s tem da je ($\lambda y\ \lambda x\ \lambda\omega$) ista točka za katerikoli $\lambda \neq 0$. Iz nehomogenih koordinat neke točke dobimo neskončno urejenih trojk homogenih koordinat iste točke, iz homogenih koordinat neke točke pa lahko dobimo eno samo urejeno dvojico števil.

Premica je urejena trojka števil ($v\ u\ w$), ki niso vse hkrati enake nič, s tem da je ($\mu v\ \mu u\ \mu w$) ista premica za katerikoli $\mu \neq 0$. Trojka $(v\ u\ w) = (x_1\text{-}x_2\ y_1\text{-}y_2\ y_1\ x_2\text{-}\ y_2\ x_{1)}$ predstavlja koordinate premice zapisane s pravokotnimi koordinatami, trojka $(v\ u\ w) = (-\cos\varphi \sin\varphi\ y_1 \cos\varphi\ -\ x_1 \sin\varphi)$ pa koordinate premice zapisane s polarnimi koordinatami.

Z uporabo projektivnih koordinat je določitev presečišča $R(Y\ X)$ dveh premic, premice l_1, ki ju določata točki $A_1(Y_1\ X_1)$ in $A_2(Y_2\ X_2)$ ter premice l_2 na kateri ležita točki $B_1(Y_1\ X_1)$ in $B_2(Y_2\ X_2)$ zelo enostavna, saj se presečišče določi s pomočjo devetih determinant drugega reda:

Najprej se določijo koordinate premic l_1 in l_2 za kar je potrebno rešiti šest determinant drugega reda:

$$\lambda = 1 \Rightarrow l_1 = (v_1 \quad u_1 \quad w_1) = \left(\begin{vmatrix} X_1 & 1 \\ X_2 & 1 \end{vmatrix} \begin{vmatrix} 1 & Y_1 \\ 1 & Y_2 \end{vmatrix} \begin{vmatrix} Y_1 & X_1 \\ Y_2 & X_2 \end{vmatrix} \right)$$

$$\lambda = 1 \Rightarrow l_2 = (v_2 \quad u_2 \quad w_2) = \left(\begin{vmatrix} X_1 & 1 \\ X_2 & 1 \end{vmatrix} \begin{vmatrix} 1 & Y_1 \\ 1 & Y_2 \end{vmatrix} \begin{vmatrix} Y_1 & X_1 \\ Y_2 & X_2 \end{vmatrix} \right)$$

Presečišče R, kot presek premic l_1 in l_2 pa je odrejeno z rešitvijo še treh determinant drugega reda:

$$\mu = 1 \Rightarrow R = (y \quad x \quad \omega) = \left(\begin{vmatrix} u_1 & w_1 \\ u_2 & w_2 \end{vmatrix} \begin{vmatrix} w_1 & v_1 \\ w_2 & v_2 \end{vmatrix} \begin{vmatrix} v_1 & u_1 \\ v_2 & u_2 \end{vmatrix} \right)$$

$$R = (y \quad x \quad \omega) = \left(\frac{y}{\omega} \quad \frac{x}{\omega} \quad 1 \right) = (Y \quad X \quad 1) = (Y \quad X)$$

Projektivno ravnino dobimo iz evklidske ravnine, če privzamemo točke in premico v neskončnosti. Točka s koordinatami (y x ω) leži v evklidski ravnini, če je $\omega \neq 0$ in je točka v neskončnosti, če je $\omega = 0$.

Dve različni neskončni točki določata premico v neskončnosti (0 0 1) na kateri ležijo vse točke v neskončnosti. Zapis (sin φ cos φ 0) predstavlaj koordinate neskončne točke iz katerih razberemo kot, ki ga neka premica oklepa s pozitivnim delom abscisne osi.

Če oklepa premica l_1 s pozitivnim delom prve osi kot φ_1 s premico l_2 pa kot α lahko neskončno točko premice l_2 določimo kot (sin ($\varphi_1 \pm \alpha$) $cos(\varphi_1 \pm \alpha)$ 0) pri čemer je $\varphi_2 = \varphi_1 \pm \alpha$ smerni kot premice l_2.

Z uvedbo neskončnih točk in neskončne premice se v merskih dvodimenzionalnih nalogah (praktični primer uporabe prikazan v zunanjem urezu) izognemo računanju dolžin in smernih kotov. Koordinate neznane točke vedno določimo kot presečišče dveh premic, ki jih določat dani točki ter točki v neskončnosti.

REFERENCES

[1] HABE, T. (2007): *Možnost uporabe homogenih (projektivnih) koordinat v dvodimenzionalnih merskih nalogah*: *Diplomsko delo*. Faculty of Natural Sciences and Engineering, Ljubljana, 77 p.

[2] AYRES, F. (1967): *Theory and problems of projective geometry*. New York, US. 243 p.

[3] PALMAN, D. (1984): *Projektivna geometrija*. Zagreb, Croatia, 343 p.

[4] VIDAV, I. (1981): *Afina in projektivna geometrija*. Ljubljana, Slovenia, 170 p.

How we calculate volume with the use of "NTF" method

Kako izračunamo volumen z uporabo metode "NTF"

Anes Durgutović[1], Milivoj Vulić[2]

[1]Oikos d.o.o., Jarška cesta 30, SI-1230 Ljubljana, Slovenia;
E-mail: anes.durgutovic@oikos.si
[2]University of Ljubljana, Faculty of Natural sciences and Engineering,
Department of Geotechnology and Mining Engineering, Aškerčeva cesta 12,
SI-1000 Ljubljana, Slovenia;
E-mail: milivoj.vulic@ntf.uni-lj.si

Received: November 23, 2007 **Accepted:** January 4, 2008

Abstract: In the article titled *Volume calculation with the use of "NTF" method* and the *"UDF" for calculation of volumes with the use of "NTF" method,* mathematic plan of the mentioned principal method is presented and instructions for the use of "UDF" are also given. When it comes to the introduction into work with new computer programs the most effective explanation of the method of use is on the basis of a practical example. The purpose of this article is to represent the calculation of volumes with the use of "NTF" method with the use of "UDF" in the simple way on a practical example.

Izvleček: V prispevkih z naslovoma *Izračun volumnov z uporabo metode* "*NTF*" ter "*UDF*"*-ji za izračun volumnov po metodi* "*NTF*", je predstavljena matematična zasnova osnove omenjene metode ter so podana navodila za uporabo "UDF"-jev. Pri uvajanju v delo z novimi računalniškimi programi se najbolje obnese razlaga načina uporabe na praktičnem primeru. Z namenom, da vam izračun volumnov z metodo "NTF" čim bolj enostavno prikažemo, vam bomo v tem prispevku, na praktičnem primeru, prikazali postopek izračuna prostornine po metodi "NTF", z uporabo "UDF"-jev.

Key words: volume calculation, Delauney triangulation, MS Excel, **"**UDF"
Ključne besede: izračun volumnov, Delaunayeva triangulacija, MS Excel , "UDF"

Scientific paper

INTRODUCTION

In order to carry out, calculation of the volume with the use "NTF" method, in the simple way. We have on the basis of the result which is shown in the above mentioned paragraph, prepared our own written functions of "UDF" which enable realization of the calculation of volume with the use of program MS Excel. When it comes to the introduction into work with new computer programs the most effective explanation of the method of use is on the basis of a practical example. The purpose of this article is to represent the calculation of volumes with the use of "NTF" method with the use of "UDF" in the simple way on a practical example.

For the representation of the calculation of volume with the use of "NTF" method we have, in the program *»Rhinoceros 3D«,* made 3D model of an imaginary geometrical shape which is formed by the selection of thirty points. Graphic representation of the model is represented in the picture below.

After we have carried out Delaney triangulation and got data about the edges of the triangles we can, therefore, calculate the volume of the shape which is formed, in our case, by the selected points.

The process of calculation can be divided into three points:

- The calculation of the volume between upper surface of the shape and the surface on the reference high (volume of the upper part of the shape),
- Determination of the outline points (only in the case if we do not have data about the points of the down surface) and the calculation of the volume between down surface of the shape and the surface on the reference high (volume of the down part of the shape),
- The calculation of the final volume.

HOW WE CARRY OUT DELANEY TRIANGULATION

In order to carry out Delaney triangulation of the upper or rather down surface we use the computer program *»Triangel Net«*, which is available for free on the internet[6]. For the use of the mentioned program we need collective data of coordinate points in the text file with ending ".nod".

When we have prepared the data in already mentioned file ".nod" we can use the already mentioned computer program *»Triangel Net«*. With a simple series of commands the program automatically carries out the Delaunay triangulation. On the place where we have saved the file with ending ".nod" we get new file with ending ".tri". In that file edge of Delaunay triangle are written.

With it we have carried out Delaunay triangulation of our collected points and got file with edge of Delaunay triangles. We transmit data from the mentioned file with ending ".tri" on the work sheet program tools Microsoft Excel where we have saved data of collective coordinated points.

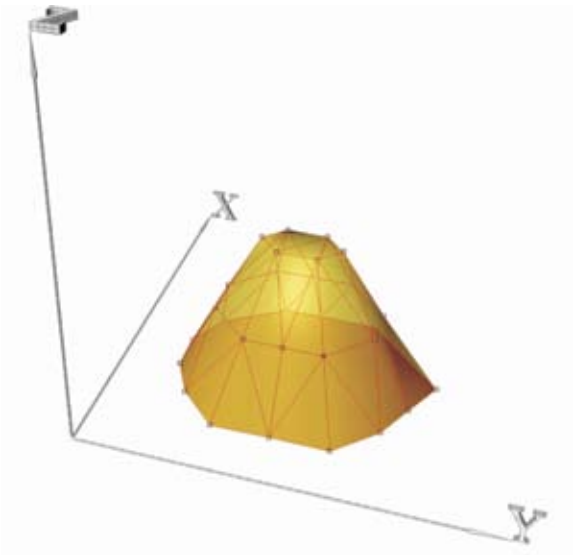

Figure 1. Shape to which we will calculate volume
Slika 1. Oblika izbranega modela, ki ga tvori trideset točk

The calculation of volume of the upper part

After we got data about edges of triangles of the Delaunay triangulation we can calculate the volume of the upper part. First we must find for the given edges suitable coordinates. The computer program *»Triangel Net«,* with which we have carried out Delaunay triangulation, marks edges which form Delaunay triangles with numbering which starts going upwards from the number 0. Because we are familiar with the feature of the mentioned program we also mark (give ID) coordinate points by numbering them, starting with 0.

In the next step we use "UDF" *»coVolW3ID«*, which finds the value of coordinate points for every individual edge of Delaunay triangles and simultaneously gives the value of the upper part of shape volume. Instructions for the use "UDF" are given in the article titled "UDF" for volume calculation with the use of "NTF" method.

For reference high (z_{ref}), we took minimal high from the collective coordinated points, which value in 50 m. The explanation of the meaning of the reference high (z_{ref}) in the article titled Volume calculation with the use of "NTF" method.

After we have carried out calculation we got the value of the volume of the upper part which we write as V_{UP}=46870.83. After getting a volume of the upper part we must, for the purpose of the calculation of the final volume, calculate the down part of the volume shape. How we calculate volume of the mentioned part is represented in the following.

Table 1. Calculated volume of the upper part
Tabela 1. Izračunana prostornina zgornjega dela

a	a	a	b	b	b	c	c	c	V
Y	X	Z	Y	X	Z	Y	X	Z	
185.0	55.0	50.0	190.0	65.0	70.3	200.0	55.0	50.3	*515.00*
185.0	55.0	50.0	175.0	65.0	50.1	190.0	65.0	70.3	*510.00*
200.0	55.0	50.3	200.0	65.0	70.3	210.0	65.0	70.2	*680.00*
200.0	55.0	50.3	210.0	65.0	70.2	215.0	55.0	50.2	*517.50*
200.0	55.0	50.3	190.0	65.0	70.3	200.0	65.0	70.3	*681.67*
215.0	55.0	50.2	210.0	65.0	70.2	225.0	65.0	50.1	*512.50*
175.0	65.0	50.1	180.0	75.0	70.3	190.0	65.0	70.3	*1017.50*
175.0	65.0	50.1	170.0	75.0	50.1	180.0	75.0	70.3	*341.67*
190.0	65.0	70.3	180.0	75.0	70.3	190.0	80.0	90.1	*2017.50*
190.0	65.0	70.3	190.0	80.0	90.1	195.0	75.0	90.0	*1255.00*
190.0	65.0	70.3	195.0	75.0	90.0	200.0	65.0	70.3	*1343.33*
200.0	65.0	70.3	195.0	75.0	90.0	205.0	75.0	90.1	*1673.33*
200.0	65.0	70.3	205.0	75.0	90.1	210.0	65.0	70.2	*1343.33*
210.0	65.0	70.2	205.0	75.0	90.1	210.0	80.0	90.1	*1255.00*
210.0	65.0	70.2	210.0	80.0	90.1	220.0	75.0	70.1	*2010.00*
210.0	65.0	70.2	220.0	75.0	70.1	225.0	65.0	50.1	*1010.00*
225.0	65.0	50.1	220.0	75.0	70.1	230.0	75.0	50.2	*340.00*
170.0	75.0	50.1	170.0	85.0	50.1	180.0	75.0	70.3	*341.67*
180.0	75.0	70.3	180.0	85.0	70.3	190.0	80.0	90.1	*1345.00*
180.0	75.0	70.3	170.0	85.0	50.1	180.0	85.0	70.3	*678.33*
195.0	75.0	90.0	190.0	80.0	90.1	195.0	85.0	90.0	*1000.83*
195.0	75.0	90.0	195.0	85.0	90.0	205.0	85.0	90.0	*2000.00*
195.0	75.0	90.0	205.0	85.0	90.0	205.0	75.0	90.1	*2001.67*
205.0	75.0	90.1	205.0	85.0	90.0	210.0	80.0	90.1	*1001.67*
220.0	75.0	70.1	210.0	80.0	90.1	220.0	85.0	70.0	*1336.67*
220.0	75.0	70.1	220.0	85.0	70.0	230.0	75.0	50.2	*671.67*
230.0	75.0	50.2	220.0	85.0	70.0	235.0	85.0	50.1	*507.50*
190.0	80.0	90.1	180.0	85.0	70.3	195.0	85.0	90.0	*1255.00*
210.0	80.0	90.1	205.0	85.0	90.0	210.0	95.0	70.1	*1252.50*
210.0	80.0	90.1	210.0	95.0	70.1	220.0	85.0	70.0	*2005.00*
170.0	85.0	50.1	175.0	95.0	50.0	180.0	85.0	70.3	*340.00*
180.0	85.0	70.3	175.0	95.0	50.0	190.0	95.0	70.2	*1012.50*
180.0	85.0	70.3	190.0	95.0	70.2	190.0	80.0	90.1	*2015.00*
195.0	85.0	90.0	180.0	85.0	70.3	190.0	95.0	70.2	*2012.50*
195.0	85.0	90.0	190.0	95.0	70.2	200.0	95.0	70.1	*1338.33*
195.0	85.0	90.0	200.0	95.0	70.1	205.0	85.0	90.0	*1668.33*
205.0	85.0	90.0	200.0	95.0	70.1	210.0	95.0	70.1	*1336.67*
220.0	85.0	70.0	210.0	95.0	70.1	225.0	95.0	50.1	*1005.00*
220.0	85.0	70.0	225.0	95.0	50.1	235.0	85.0	50.1	*505.00*
175.0	95.0	50.0	190.0	105.0	50.0	190.0	95.0	70.2	*505.00*
190.0	95.0	70.2	190.0	105.0	50.0	200.0	95.0	70.1	*671.67*
200.0	95.0	70.1	200.0	105.0	50.3	210.0	95.0	70.1	*675.00*
200.0	95.0	70.1	190.0	105.0	50.0	200.0	105.0	50.3	*340.00*
210.0	95.0	70.1	200.0	105.0	50.3	215.0	105.0	50.2	*515.00*
210.0	95.0	70.1	215.0	105.0	50.2	225.0	95.0	50.1	*510.00*
							Together		***46870.83***

Definition of the outline points

When we do not have the definition of the down surface, we can only from the outline points determine the surface which we use as down surface. As the first step of defining of the outline points of the down surface of the mentioned shape we have, among the given edges which form Delaunay triangles, connected straight lines.

During that we eliminated straight lines which have appeared among the same edges twice. For the calculation of that mentioned process we use "UDF" »*linesSortedW3«*. The functions offers us, from the individual edges of triangle net, classification of lines between two edges and also mark the ones which occur only once. (See the article titled "UDF" for volume calculation with the use of "NTF" method).

In the next step we use udf »*outLineW«*, which, from contour lines between two edges in triangle net, gives us only contour lines. (See the article titled "UDF" for volume calculation with the use of "NTF" method).

By doing this we must pay attention to the given selection of outpoints and checks the given selection by drawing them in some program for designing. In this way we will check whether we got the actual shape of the outline surface. Because of that the example, where it is necessary to eliminate the last three given outlines, is presented. The reason for that, is that represented way of determining of outpoints, can cause mistakes. In the already presented example there are 14 outpoints which we will use for the further calculation.

For the selection of outpoints of the down surface we use "UDF" »*outPoints«* which, from sorted contour lines between two edges in triangle net, gives us only contour point. (See the article titled UDF for volume calculation with the use of "NTF" method).

The calculation of volume of the down part

After we have determined the points of the down surface, we can start with calculation of the volume between down surface of the shape and the surface on the reference high (volume of the down part of the shape). Firstly, we must determine suitable coordinate values to the outline points of the down surface. For the selection of the suitable coordinate values we use "UDF" »*coEntW«* see the article titled "UDF" for volume calculation with the use of "NTF" method). Therefore, we get written coordinate values of the outpoints of the down surface.

After getting written coordinate values of the outpoints of the down surface, we again carry out the same steps which we have made at volume calculation of the upper surface. At first, we prepared the data (coordinate values of the outpoints of the down surface) in the text file with ending ''.nod. Therefore, with the use of program *(»Triangel Net«),* carry out the Delaunay triangulation of down surface.

We carry out the calculation of the down surface volume in the same way as we calculated the upper surface volume. After we have carried out calculation which is pre-

Table 2. Calculated volume of the down part
Tabela 2. Izračunana prostornina spodnjega dela

d Y	d X	d Z	e Y	e X	e Z	f Y	f X	f Z	V
185.0	55.0	50.0	175.0	65.0	50.1	200.0	55.0	50.3	*10.00*
200.0	55.0	50.3	175.0	65.0	50.1	175.0	95.0	50.0	*50.00*
200.0	55.0	50.3	175.0	95.0	50.0	200.0	105.0	50.3	*125.00*
200.0	55.0	50.3	200.0	105.0	50.3	225.0	95.0	50.1	*145.83*
200.0	55.0	50.3	225.0	95.0	50.1	225.0	65.0	50.1	*62.50*
200.0	55.0	50.3	225.0	65.0	50.1	215.0	55.0	50.2	*15.00*
175.0	65.0	50.1	170.0	75.0	50.1	170.0	85.0	50.1	*2.50*
175.0	65.0	50.1	170.0	85.0	50.1	175.0	95.0	50.0	*5.00*
225.0	65.0	50.1	225.0	95.0	50.1	230.0	75.0	50.2	*10.00*
230.0	75.0	50.2	225.0	95.0	50.1	235.0	85.0	50.1	*10.00*
175.0	95.0	50.0	190.0	105.0	50.0	200.0	105.0	50.3	*5.00*
225.0	95.0	50.1	200.0	105.0	50.3	215.0	105.0	50.2	*15.00*
							Together		***455.83***

sented in table 2 we got the volume of the down surface $V_{DOWN} = 455.83$.

Now we can determine the final volume presented shape in terms of subtracting the down shape volume from upper shape volume. In this way we get final volume of the presented shape, that is:

$$V = V_{UP} - V_{DOWN} = 46870.83 - 455.83 = 46415.00$$

CONCLUSIONS

Throughout the presented method of the volume calculation with the use of "NTF" method we have established:

- That the final result of the shape volume depends on the way of collecting points at topographic measurement (if we made mistakes at field measurements, we will most likely get the incorrect result about the shape volume).
- That in the case of a large number of collected points the time of calculation is extended, because we need more time to calculate Delaunay triangulation.
- That when do not have the definition of the down surface, we can with the help of "UDF" select outline points and determine the surface which we use as down surface. By doing this we must pay attention to the given selection of outpoints and check the given selection by drawing them in some program for designing.
- That we can simultaneously check the process of calculation and in this way dismiss possible mistakes which we made in the process of calculation.

Visually presented example of the entire process of calculation is available on the web site: http:/www. ntfgam.uni-lj.si/mvulic.

Povzetek

Kako izračunamo volumen z uporabo metode "NTF"

V prispevku je na praktičnem primeru prikazan postopek izračuna prostornine po metodi "NTF", z uporabo "UDF"-jev. Prispevek je nadaljevanje člankov *Calculation of volume with the use of "NTF" method*[9] and *"UDF" for volume calculation with the use of "NTF" method*[8]. Za prikaz postopka izračuna na praktičnem primeru je bil predhodno oblikovan model telesa, ki ga tvori trideset izbranih točk. Model telesa smo oblikovali z uporabo računalniškega programa *»Rhinoceros 3D«*. Delaunayevo triangulacijo iz točk izbranega telesa izvedemo v računalniškem programu "Triangel Net". Na podlagi izvedene triangulacije dobimo podatke o ogliščih, ki tvorijo Delaunayeve trikotnike. To nam je tudi osnova za izvedbo izračuna. Ko smo izvedli Delaunayevo triangulacijo ter dobili podatke o ogliščih trikotnikov izvedene triangulacije, lahko izračunamo prostornino telesa, ki ga tvorijo, v našem primeru izbrane točke. Sam postopek izračuna lahko razdelimo na tri dele:

- določitev prostornine med plaščem in referenčno ravnino,
- izbor konturnih točk ter določanje prostornine med konturo in referenčno ravnino,
- določitev končne prostornine.

Postopek izračuna volumna po izvedeni Delaunayevi triangulaciji izvedemo z uporabo lastno zapisanih funkcij (MS Excel) "UDF".

Vizualna predstavitev praktičnega primera izračuna oz. prikaz celotnega procesa je dostopen na: http:/www.ntfgam.uni-lj.si/mvulic.

References

[1] Bronštejn, J.N., Semendjajev, K.A. (1978): *Matematični priročnik*. Tehniška založba Slovenije, Ljubljana, 683 p.

[2] O`Rourke, J. (1997): *Computational geometry in C*. Cabbridge univerity press, 350 p.

[3] Vulić, M. (2005): *User Defined Function*. Naravoslovnotehniška fakulteta, Ljubljana.

[4] Vulić, M. (2005): *Matematične osnove določanja prostornin tristranih prizem (interna predavanja)*. Naravoslovnotehniška fakulteta, Ljubljana.

[5] Vulić, M. (2005): *Osnove Delaunayeve triangulacije in Voronoi diagramov (interna predavanja)*. Naravoslovnotehniška fakulteta, Ljubljana.

[6] http://www.codeproject.com/cpp/kazumi.asp.

[7] Durgutović, A. (2005): *Izmera in določanje prostornin nepravilnih teles z uporabo metode "RTK-GPS": diplomsko delo*. Naravoslovnotehniška fakulteta, Ljubljana.

[8] Vulić, M., Durgutović, A. (2007): "UDF" for volume calculation with the use of "NTF" method. *RMZ - Materials and Geoenvironment*; Vol. 54, No. 3, pp. 419-425.

[9] VULIĆ, M., DURGUTOVIĆ, A. (2006): Calculation of volume with the use of "NTF" method. *RMZ - Materials and Geoenvironment*; Vol. 53, No. 2, pp. 221-227.

[10] VULIĆ, M. (2005): *Osnove topologije (interna predavanja)*. Naravoslovnotehniška fakulteta, Ljubljana.

[11] VULIĆ, M. (2005): *Transformacije koordinatnih sistemov (interna predavanja)*. Naravoslovnotehniška fakulteta, Ljubljana.

Strokovna literatura - Professional literature

Marko Zlokarnik
Prenos merila
Izdajatelj: Ljubljana: Zavod za tehnično izobraževanje, 2007.
Obseg: 106 strani, format 24 x 17 cm, cena: 20 EUR.
ISBN: 978-961-6135-60-3.

V slovenščini je izšla knjiga Prenos merila svetovno znanega strokovnjaka za procesno tehnologijo prof. dr. Marka Zlokarnika, ki je deloval kot raziskovalec 35 let v kemijski multinacionalki Bayer A. G. v Leverkusnu z obširno bibliografijo in nato kot profesor na tehniški univerzi Köln. Njegovo strokovno delo je zadevalo laboratorijske meritve najrazličnejših postopkov, katerih rezultate je bilo treba nato prenesti v industrijsko, tehnično merilo. Tako si je pridobil neštevilne izkušnje, katerih pravilnost je bila vselej preizkušena in potrjena v industrijskem merilu. Knjiga je skrajšana izdaja originalnega dela, ki je izšlo pri renomirani založbi J. Wiley – VCH v ZDA v letih 2000 oz. 2002 v angleščini pod naslovom Scale-up in Chemical Engineering in v nemščini pod naslovom Scale-up – Modellübertragung in der Verfahrenstechnik. Knjigi sta bili po samo štirih letih razprodani in izšla je 2., za sto strani razširjena izdaja. Kdor se bo želel razgledati po tem področju podrobneje, mu bosta ti knjigi v veliko oporo, kajti slovenska izdaja ima samo tretjino originalnega obsega. Leta 2007 so odkupili Kitajci licenco za knjigo in izšla je v veliki nakladi v kitajščini, kar priča o njeni veliki uporabnosti v tehničnem svetu.

Pri prenosu merila iz majhnega v veliko (ali pa tudi obratno!) je zahtevana popolna podobnost med modelom in tehnično izvedbo, in to v geometričnem, snovnem in procesno-tehničnem pogledu. Osnova metode je dimenzijska analiza, s katero se prenese relevantne veličine, s katerimi je proces popolnoma opisan, v brezdimenzijska števila. Teh je po eni strani manj, kot je dimenzijskih (t.i. pi-teorem), po drugi strani pa je predstava meritev v brezdimenzijskem prostoru "invariantna" z ozirom na sleherno merilo, tako tudi z ozirom na dolžinsko merilo. Zato predstavlja ta metoda edin zanesljiv prenos postopka iz malega v veliko.

Prva polovica knjige prinaša osnove dimenzijske analize in prenosa merila, druga polovica knjige pa prinaša praktične primere. Knjiga izpolnjuje veliko vrzel: področje prenosa izdelkov in rezultatov meritev iz malih dimenzij na realne velike, s čemer se pečajo projektanti tovarniških naprav, ni bilo dovolj jasno obdelano na nobeni ravni od strokovnih do visokih šol, najbrž zato, ker predstavlja proizvodni tehnološki vidik, za katerega teoretiki nimajo posluha, so pa osnovne naloge procesnega inženiringa. Problem prenosljivosti eksperimentalnih rezultatov na realne velikosti zavzema osrednje mesto v procesnem projektiranju. Težavnost problema je nazornejša, ker se tekom procesa dogajajo pomembne spremembe lastnosti snovi. Ker je procesno področje zelo blizu tudi našim metalurgom, jim bo ta knjiga dobro služila.

Dr. Marko Kos

Author`s Index, Vol. 55, No. 1

Anžel Ivan	ivan.anzel@uni-mb.si	1
Bombač David	david.bombac@ntf.uni-lj.si	19
Bradaskja Boštjan	bostjan.bradaskja@acroni.si	31
Čevnik Gabrijela	gcevnik@metalravne.com	1
Dimc Franc	franc.dimc@fpp.uni-lj.si	85
Durgutović Anes	anes.durgutovic@oikos.si	127
Fazarinc Matevž	matevz.fazarinc@ntf.uni-lj.si	19, 31
Ganić Aleksandar	aganic@rgf.bg.ac.yu	111
Gosar Andrej	andrej.gosar@gov.si	41, 67
Habe Tina	tinahabe@gmail.com	111
Knap Matjaž	matjaz.knap@ntf.uni-lj.si	31
Koruza Jurij	jurij.koruza@ntf.uni-lj.si	31
Kosec Gorazd	gorazd.kosec@acroni.si	1
Kosec Borut	borut.kosec@ntf.uni-lj.si	1
Kosec Ladislav	kosec@ntf.uni-lj.si	1
Kugler Goran	goran.kugler@ntf.uni-lj.si	19
Mušič Branko	branko.music@ff.uni-lj.si	85
Osredkar Radko	radko.osredkar@fri.uni-lj.si	85
Rošer Janez	janez.roser@ntf.uni-lj.si	41, 67
Rudolf Rebeka	rebeka.rudolf@uni-mb.si	1
Runovc Franc	franc.runovc@ntf.uni-lj.si	111
Stopar Robert	robert.stopar@geo-inz.si	41, 67
Turk Radomir	rado.turk@ntf.uni-lj.si	19, 31
Vulić Milivoj	milivoj.vulic@ntf.uni-lj.si	111, 127
Zupanič Franc	franc.zupanic@uni-mb.si	7

INSTRUCTIONS TO AUTHORS

RMZ-MATERIALS & GEOENVIRONMENT (RMZ- Materiali in geookolje) is a periodical publication with four issues per year (established 1952 and renamed to RMZ-M&G in 1998). The main topics of contents are Mining and Geotechnology, Metallurgy and Materials, Geology and Geoenvironment.
RMZ-M&G publishes original Scientific articles, Review papers, Technical and Expert contributions (also as short papers or letters) **in English**. In addition, evaluations of other publications (books, monographs,...), short letters and comments are welcome. A short summary of the contents in Slovene will be included at the end of each paper. It can be included by the author(s) or will be provided by the referee or the Editorial Office.
**** Additional information and remarks for Slovenian authors:***
English version with extended »Povzetek«, and additional roles (in Template for Slovenian authors) ***can*** *be written. Only exceptionally the articles in the Slovenian language with summary in English will be published. The contributions in English will be considered with priority over those in the Slovenian language in the review process.*

Authorship and originality of the contributions. Authors are responsible for originality of presented data, ideas and conclusions as well as for correct citation of data adopted from other sources. The publication in RMZ-M&G obligate authors that the article will not be published anywhere else in the same form.

Specification of Contributions

Optimal number of pages of full papers is 7 to 15, longer articles should be discussed with Editor, but 20 pages is limit.
Scientific papers represent unpublished results of original research.
Review papers summarize previously published scientific, research and/or expertise articles on the new scientific level and can contain also other cited sources, which are not mainly result of author(s).
Technical and Expert papers are the result of technological research achievements, application research results and information about achievements in practice and industry.
Short papers (Letters) are the contributions that contain mostly very new short reports of advanced investigation. They should be approximately 2 pages long but should not exceed 4 pages.
Evaluations or critics contain author's opinion on new published books, monographs,

textbooks, exhibitions...(up to 2 pages, figure of cover page is expected).
In memoriam (up to 2 pages, a photo is expected).
Professional remarks (Comments) cannot exceed 1 page, and only professional disagreements can be discussed. Normally the source author(s) reply the remarks in the same issue.

Supervision and review of manuscripts. All manuscripts will be supervised. The referees evaluate manuscripts and can ask authors to change particular segments, and propose to the Editor the acceptability of submitted articles. Authors can suggest the referee but Editor has a right to choose another. **The name of the referee remains anonymous.** The technical corrections will be done too and authors can be asked to correct missing items. The final decision whether the manuscript will be published is made by the Editor in Chief.

The Form of the Manuscript

The manuscript should be submitted as a complete hard copy including figures and tables. The figures should also be enclosed separately, both charts and photos in the original version. In addition, all material should also be provided in electronic form on a diskette or a CD. The necessary information can conveniently also be delivered by E-mail.

Composition of manuscript is defined in the attached Template

The original file of Template is temporarily available on E-mail addresses:
peter.fajfar@ntf.uni-lj.si,
barbara.bohar@ntf.uni-lj.si

References - can be arranged in two ways:
- first possibility: alphabetic arrangement of first authors - in text: (Borgne, 1955),
or
- second possibility: [1] numerated in the same order as cited in the text: example[1]

Format of papers in journals:

Le Borgne, E. (1955): Susceptibilite magnetic anomale du sol superficiel. *Annales de Geophysique*, 11, pp. 399-419.

Format of books:

Roberts, J. L. (1989): Geological structures, *MacMillan*, *London*, 250 p.

Text on the hard print copy can be prepared with any text-processor. The electronic version on the diskette, CD or E-mail transfer should be in MS Word or ASCII format.
Captions of figures and tables should be enclosed separately. **Figures (graphs and photos)** and tables should be original and sent separately in addition to text. They can be prepared on paper or computer designed (MSExcel, Corel, Acad).
Format. Electronic figures are recommended to be in CDR, Al, EPS, TIF or JPG formats. Resolution of bitmap graphics (TIF, JPG) should be at least 300 dpi. Text in vector graphics (CDR, Al, EPS) must be in MSWord Times typography or converted in curves.
Color prints. Authors will be charged for color prints of figures and photos.
Labeling of the additionally provided material for the manuscript should be very clear and must contain at least the lead author's name, address, the beginning of the title and the date of delivery of the manuscript. In case of an E-mail transfer the exact message with above asked data must accompany the attachment with the file containing the manuscript.
Information about RMZ-M&G:
Editor in Chief prof. dr. Peter Fajfar (tel. ++386 1 4250-316) or
Secretary Barbara Bohar Bobnar, un. dipl. ing. geol. (++386 1 4704-630),
Aškerčeva 12, Ljubljana, Slovenia

or at E-mail addresses:
peter.fajfar@ntf.uni-lj.si,
barbara.bohar@ntf.uni-lj.si

Sending of manuscripts. Manuscripts can be sent by mail to the **Editorial Office** address:

- RMZ-Materials & Geoenvironment
  Aškerčeva 12,
  1000 Ljubljana, Slovenia

or delivered to:

- **Reception** of the Faculty of Natural Science and Engineering (for RMZ-M&G)
  Aškerčeva 12,
  1000 Ljubljana, Slovenia
- E-mail - addresses of Editor and Secretary
- You can also contact them on their phone numbers.

TEMPLATE

The title of the manuscript should be written in bold letters (Times New Roman, 14, Center)

Name Surname[1], …. , & Name Surname[X]
(Times New Roman, 12, Center)

[x]Faculty of ... , University of ... , Address…, Country, e-mail: ...
(Times New Roman, 11, Center)

THE LENGTH OF FULL PAPER SHOULD NOT EXCEED TWENTY (20, INCLUDING FIGURES AND TABLES) PAGES (OPTIMAL 7 TO 15), SHORT PAPER FOUR (4) AND OTHER TWO (2) WITHOUT TEXT FLOWING BY GRAPHICS AND TABLES.

Abstract (Times New Roman, Normal, 11): The text of the abstract is placed here. The abstract should be concise and should present the aim of the work, essential results and conclusion. It should be typed in font size 11, single-spaced. Except for the first line, the text should be indented from the left margin by 10 mm. The length should not exceed fifteen (15) lines (10 are recommended).

Key words: a list of up to 5 key words (3 to 5) that will be useful for indexing or searching. Use the same styling as for abstract.

Introduction (Times New Roman, Bold, 12)

Two lines below the keywords begin the introduction. Use Times New Roman, font size 12, Justify alignment.
There are two (2) admissible methods of citing references in text:

1. by stating the first author and the year of publication of the reference in the parenthesis at the appropriate place in the text and arranging the reference list in the alphabetic order of first authors; e.g.:
   "Detailed information about geohistorical development of this zone can be found in: Antonijević (1957), Grubić (1962), ..."
   "… the method was described previously (Hoefs, 1996)"

2. by consecutive Arabic numerals in square brackets, superscripted at the appropriate place in the text and arranging the reference list at the end of the text in the like manner; e.g.:
   "... while the portal was made in Zope[3] environment."

Materials and methods (Times New Roman, Bold, 12)

This section describes the available data and procedure of work and therefore provides enough information to allow the interpretation of the results, obtained by the used methods.

Results and discussion (Times New Roman, Bold, 12)

Tables, figures, pictures, and schemes should be incorporated in the text at the appropriate place and should fit on one page. Break larger schemes and tables into smaller parts to prevent extending over more than one page.

Conclusions (Times New Roman, Bold, 12)

This paragraph summarizes the results and draws conclusions.

Acknowledgements (Times New Roman, Bold, 12, Center - optional)

This work was supported by the ****.

References (Times New Roman, Bold, 12*)*

In regard to the method used in the text, the styling, punctuation and capitalization should conform to the following:

FIRST OPTION - in alphabetical order

Casati, P., Jadoul, F., Nicora, A., Marinelli, M., Fantini-Sestini, N. & Fois, E. (1981): Geologia della Valle del'Anisici e dei gruppi M. Popera - Tre

Cime di Lavaredo (Dolomiti Orientali). *Riv. Ital. Paleont.*; Vol. 87, No. 3, pp. 391-400, Milano.

Folk, R. L. (1959): Practical petrographic classification of limestones. *Amer. Ass. Petrol. Geol. Bull.;* Vol. 43, No. 1, pp. 1-38, Tulsa.

SECOND OPTION - in numerical order

[1] Trček, B. (2001): *Solute transport monitoring in the unsaturated zone of the karst aquifer by natural tracers*. Ph.D. Thesis. Ljubljana: University of Ljubljana 2001; 125 p.

[2] Higashitani, K., Iseri, H., Okuhara, K., Hatade, S. (1995): Magnetic Effects on Zeta Potential and Diffusivity of Nonmagnetic Particles. *Journal of Colloid and Interface Science 172*, pp. 383-388.

Citing the Internet site:

CASREACT-Chemical reactions database [online]. Chemical Abstracts Service, 2000, updated 2.2.2000 [cited 3.2.2000]. Accessible on Internet: http://www.cas.org/CASFILES/casreact.html.

Povzetek (Times New Roman, 12)

A short summary of the contents in Slovene (up to 400 characters) can be written by the author(s) or will be provided by the referee or by the Editorial Board.

TEMPLATE for Slovenian Authors

The title of the manuscript should be written in bold letters (Times New Roman, 14, Center)

Naslov članka (Times New Roman, 14, Center)

Name Surname[1],…. , & Name Surname[X] (Times New Roman, 12, Center)
Ime Priimek[1], …, Ime Priimek[X] (Times New Roman, 12, Center)

[X]Faculty of ... , University of ... , Address…, Country; e-mail: ...
(Times New Roman, 11, Center)
[X]Fakulteta…, Univerza…, Naslov…, Država; e-mail: …
(Times New Roman, 11, Center)

THE LENGTH OF ORIGINAL SCIENTIFIC PAPER SHOULD NOT EXCEED TWENTY (20, INCLUDING FIGURES AND TABLES) PAGES (OPTIMAL 7 TO 15), SHORT PAPER FOUR (4) AND OTHER TWO (2) WITHOUT TEXT FLOWING BY GRAPHICS AND TABLES.
DOLŽINA IZVIRNEGA ZNANSTVENEGA ČLANKA NE SME PRESEGATI DVAJSET (20, VKLJUČNO S SLIKAMI IN TABELAMI), KRATKEGA ČLANKA ŠTIRI (4) IN OSTALIH PRISPEVKOV DVE (2) STRANI.

Abstract (Times New Roman, Normal, 11): The text of the abstract is placed here. The abstract should be concise and should present the aim of the work, essential results and conclusion. It should be typed in font size 11, single-spaced. Except for the first line, the text should be indented from the left margin by 10 mm. The length should not exceed fifteen (15) lines (10 are recommended).

Izvleček (TNR, N, 11): Kratek izvleček namena članka ter ključnih rezultatov in ugotovitev. Razen prve vrstice naj bo tekst zamaknjen z levega roba za 10 mm. Dolžina naj ne presega petnajst (15) vrstic (10 je priporočeno).

Key words: a list of up to 5 key words (3 to 5) that will be useful for indexing or searching. Use the same styling as for abstract.

Ključne besede: seznam največ 5 ključnih besed (3-5) za pomoč pri indeksiranju ali iskanju. Uporabite enako obliko kot za izvleček.

Introduction – Uvod (Times New Roman, Bold, 12)

Two lines below the keywords begin the introduction. Use Times New Roman, font size 12, Justify alignment. All captions of text and tables as well as the text in graphics must be prepared in English and Slovenian language.
Dve vrstici pod ključnimi besedami se začne Uvod. Uporabite pisavo TNR, velikost črk 12, z obojestransko poravnavo. Naslovi slik in tabel (vključno z besedilom v slikah) morajo biti pripravljeni v slovenskem in angleškem jeziku.

Figure (Table) X. Text belonging to figure (table)
Slika (Tabela) X. Pripadajoče besedilo k sliki (tabeli)

There are two (2) admissible methods of citing references – obstajata dve sprejemljivi metodi navajanja referenc:

1. by stating the first author and the year of publication of the reference in the parenthesis at the appropriate place in the text and arranging the reference list in the alphabetic order of first authors; e.g.:
1. z navedbo prvega avtorja in letnice objave reference v oklepaju na ustreznem mestu v tekstu in z ureditvijo seznama referenc po abecednem zaporedju prvih avtorjev; npr.:
   "Detailed information about geohistorical development of this zone can be found in: Antonijević (1957), Grubić (1962), ..."
   "… the method was described previously (Hoefs, 1996)"

or/ali

2. by consecutive Arabic numerals in square brackets, superscripted at the appropriate place in the text and arranging the reference list at the end of the text in the like manner; e.g.:
2. z zaporednimi arabskimi številkami v oglatih oklepajih na ustreznem mestu v tekstu in z ureditvijo seznama referenc v številčnem zaporedju navajanja; npr.;
   "... while the portal was made in Zope[3] environment."

Materials and methods (Times New Roman, Bold, 12)

This section describes the available data and procedure of work and therefore provides enough information to allow the interpretation of the results, obtained by the used methods.
Ta del opisuje razpoložljive podatke, metode in način dela ter omogoča zadostno količino informacij, da lahko z opisanimi metodami delo ponovimo.

Results and discussion – Rezultati in razprava (Times New Roman, Bold, 12)

Tables, figures, pictures, and schemes should be incorporated (inserted, not pasted) in the text at the appropriate place and should fit on one page. Break larger schemes and tables into smaller parts to prevent extending over more than one page.
Tabele, sheme in slike je potrebno vnesti (z ukazom Insert, ne Paste) v tekst na ustreznem mestu. Večje sheme in tabele je potrebno ločiti na manjše dele, da ne presegajo ene strani.

Conclusions – Sklepi (Times New Roman, Bold, 12)

This paragraph summarizes the results and draws conclusions.
Povzetek rezultatov in zaključki.

Acknowledgements – Zahvale (Times New Roman, Bold, 12, Center - optional)

This work was supported by the ……..
Izvedbo tega dela je omogočilo ……

References - Viri (Times New Roman, Bold, 12)

With regard to the method used in the text, the styling, punctuation and capitalization should conform to the following:

Glede na uporabljeno metodo citiranja referenc v tekstu upoštevajte eno od naslednjih oblik:

FIRST OPTION (recommended) – PRVA MOŽNOST (priporočena) – in alphabetical order (v abecednem zaporedju)

Casati, P., Jadoul, F., Nicora, A., Marinelli, M., Fantini-Sestini, N. & Fois, E. (1981): Geologia della Valle del'Anisici e dei gruppi M. Popera – Tre Cime di Lavaredo (Dolomiti Orientali). *Riv. Ital. Paleont.*; Vol. 87, No. 3, pp. 391-400, Milano.

Folk, R. L. (1959): Practical petrographic classification of limestones. *Amer. Ass. Petrol. Geol. Bull.;* Vol. 43, No. 1, pp. 1-38, Tulsa.

SECOND OPTION – DRUGA MOŽNOST - in numerical order (v numeričnem zaporedju)

[1] Trček, B. (2001): *Solute transport monitoring in the unsaturated zone of the karst aquifer by natural tracers.* Ph.D. Thesis. Ljubljana: University of Ljubljana 2001; 125 p.

[2] Higashitani, K., Iseri, H., Okuhara, K., Hatade, S. (1995): Magnetic Effects on Zeta Potential and Diffusivity of Nonmagnetic Particles. *Journal of Colloid and Interface Science 172*, pp. 383-388.

Citing the Internet site:
CASREACT-Chemical reactions database [online]. Chemical Abstracts Service, 2000, updated 2.2.2000 [cited 3.2.2000]. Accessible on Internet: http://www.cas.org/CASFILES/casreact.html.

Citiranje Internetne strani:
CASREACT-Chemical reactions database [online]. Chemical Abstracts Service, 2000, obnovljeno 2.2.2000 [citirano 3.2.2000]. Dostopno na svetovnem spletu: http://www.cas.org/CASFILES/casreact.html.

Povzetek – Summary (Times New Roman, 12)

An extended summary of the contents in Slovene (from one page to approximately 1/3 of the original article length).
Razširjeni povzetek vsebine prispevka v Angleščini (od ene strani do približno 1/3 dolžine izvirnega članka).

Rešitve za opazovanje premikov in deformacij

GNSS senzor
Leica GMX902 GG

GPS senzor
Leica GMX901
in 360° reflektor
Leica GZR122

Nagibni senzor
Leica NIVEL200

Samodejni tahimeter
Leica TCA1201 M

Programska oprema
Leica GNSS Spider

Programska oprema
Leica GeoMoS

Authorized Leica Geosystems Distributor

- when it has to be **right**

Leica Geosystems

geo servis

Geoservis, d.o.o.
Litijska cesta 45, 1000 Ljubljana
t. (01) 586 38 30, i. www.geoservis.si

prof. dr. Andrej Paulin

Tehniški metalurški slovar *(CD-ROM za WINDOWS)*

slovensko - angleško - nemški

Technical metallurgical dictionary *(CD-ROM for WINDOWS)*

Slovenian - English - German

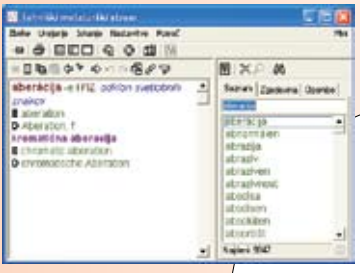

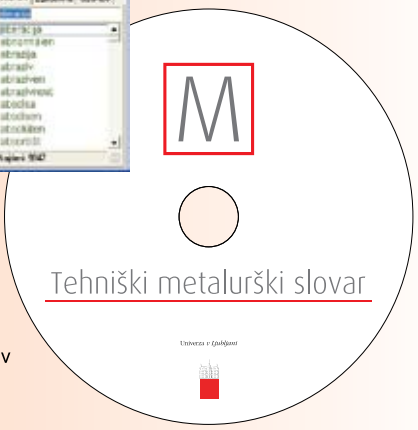

Več kot 10.000 gesel s področij:
- metalurgije,
- tehniških materialov,
- tehnike površin,
- analiznih metod,
- strojništva,
- kemije,
- elektrotehnike,
- ekologije,
- standardizacije,
- predpisov,
- ekonomike in
- uporabe računalništva pri tehnoloških postopkih.

Osnovne značilnosti oz. prednosti elektronske različice slovarja so preprost in izjemno hiter dostop do iskanega gesla, besede ali zveze, tudi pri zahtevnejših pogojih, ter velika prilagodljivost vmesnika uporabnikovim potrebam in željam. Slovar uporablja pregledovalnik ASP32 in je združljiv s številnimi drugimi slovarji v tem sistemu.

Cenik elektronskega slovarja:
Enouporabniška lokalna verzija - 58,00 EUR
5 licenc mrežna verzija - 390,00 EUR
10 licenc mrežna verzija - 535,00 EUR
20 licenc mrežna verzija - 680,00 EUR
30 licenc mrežna verzija - 825,00 EUR
40 licenc mrežna verzija - 970,00 EUR
50 licenc mrežna verzija - 1.115,00 EUR

Leto izdaje: 2007
Issued in 2007

Prices for the electronic dictionary:
Single user local version - 58,00 EUR
5 users network version - 390,00 EUR
10 users network version - 535,00 EUR
20 users network version - 680,00 EUR
30 users network version - 825,00 EUR
40 users network version - 970,00 EUR
50 users network version - 1.115,00 EUR

More than 10 000 technical terms on:
-metallurgy
-technical materials
-surface engineering
-analytical methods
-mechanical engineering
-chemical engineering
-electrical engineering
-environmental engineering
-standardization
-technical regulations
-economics, and
-computer engineering in technological processes

Basic characteristics or advantages, respectively, of electronic version of the dictionary is simple and very fast access to sought term, word or to complex term, also in more demanding conditions, and a great adaptability of the interface to user's needs and wishes. The dictionary uses ASP32 search system that is compatible to numerous other dictionaries in this system.

Za naročila in dodatne informacijenas kontaktirajte preko e-pošte:
For orders and additional information please contact us by e-mail: ***omm@ntf.uni-lj.si***